MEASURING THE SCATTER IN THE MASS RICHNESS RELATION OF GALAXY CLUSTERS FOR THE DARK ENERGY SURVEY USING THE CORRELATION FUNCTION

PhD Thesis

Julia Campa Romero

Programa de Doctorat en Física
Departament de Física
Facultat de Ciències
Universitat Autònoma de Barcelona

Curs Academic 2014-2015

Documento maquetado con TEXIS v.1.0.

MEASURING THE SCATTER IN THE MASS RICHNESS RELATION OF GALAXY CLUSTERS FOR THE DARK ENERGY SURVEY USING THE CORRELATION FUNCTION

PhD Thesis

Author: Julia Campa
Director: Juan Estrada
Tutor: Enrique Fernandez

Programa de Doctorat en Física
Departament de Física
Facultat de Ciències
Universitat Autònoma de Barcelona

Curs Academic 2014-2015

A mis padres y a mi hermano Raúl.
Para toda mi gente querida, con amor.

Acknowledgments

I would like to first say a very big thank you to my supervisor Dr. Juan Estrada for all the support and encouragement he gave me. Without his guidance, patience and constant feedback this PhD would not have been achievable. Besides being a brilliant scientist is my friend and a wonderful person.

I would also like to thank to my tutor in the Universidad Autónoma de Barcelona Professor Enrique Fernández.

I developed the mayor part of my research at the Astroparticle Physics Division at CIEMAT. My sincere thanks to Dr. Manuel Aguilar and Dr. Javier Berdugo for give me the opportunity for doing my PhD Thesis there. Dra. Mercedes Mollá for her friendship and support in my early days in the lab. She also gives the point of view of astrophysics to my research. My thanks to Dr. Nacho Sevilla for learn together cosmology by reading and discussing about papers. Thanks to share with me the o ce. Also to the Principal Investigator of the DES project at CIEMAT, Dr. Eusebio Sánchez and all participants of the group.

I greatly appreciate the support I received from the collaborative work I undertook with the Centro Brasileriro de Pesquisas Fisicas (CBPF). I am especially grateful to Dr. Martin Makler and Dra. Mariana Penna. We worked together in the theoretical predictions of the mass function and bias. I also thank for the invitation to spend some days working with them at Rio de Janeiro.

My sincere thanks to Dr. Jiangang Hao, Dra. Marcelle Soares, Dr. Jim Annis and Dr. Josh Frieman for useful discussions and communications. Also I thank to all participants of the Astrophysics Experimental Group meetings at Fermilab Center for Particle Astrophysics (FPCA).

I spent the first years of my PhD at ICE/CSIC where I worked in the R&D program for the DES focal plane detectors in collaboration with the IFAE DES group and Fermilab. I thank to Dr. Javier Castander, Dr. Pablo Fosalba, Dr. Enrique Gaztañaga, Dr. Marc Manera, Dra. Anna Cabre, Dra. Violeta Gonzalez and all the participants of the DES group. Also I thank my collaborators from IFAE, Laia Cardiel, Dr. Lluis Galvany and Dr. Manel Martinez.

I would also to extend my thanks to all the people from the Fermilab CCD Testing Group, especially Dr. Tom Diehl, Dra. Brenna Flaugher, Dra. Wyatt Merritt, Herman Cease, Bob Angstad, Donna Kubik and all the technicians of the laboratory for their help in the R&D work with the CCDs.

I gratefully acknowledge the funding sources that made my Ph.D. work possible. I obtained a fellow from the I3P Program of the European Social Fond for my first years to start my research at ICE/CSIC. Then I obtain a contract to continue at the Astroparticle Physics Division of CIEMAT for the last years. I acknowledge the fellowships of the FCPA and the economical support provided by the Particle Physics Division at Fermilab that give me the opportunities of traveling and spend some time there.

I thank my lab mates in the CIEMAT. In my daily work I have been fortunate to have a friendly and cheerful group of PhD students, postdocs and engineers. A very special thanks goes to Cristina de La Guia La Bailaora, David Crespo, Antonio Delgado, Bruno García, Carmen Diez, Maria Cepeda, Ignacio Cernuda, Aurelio Carnero, Jesús Puerta, Jorge Berenguer, Rafael Ponce, Adrian Quintario, Jose Crespo, Mariano Betis, Mara Senghi, Eduardo Navarro, Javier Sánchez, Manuel Moreno, Carlos Diaz, Juanjo Rodríguez, Isabel Rodríguez, Miguel Ángel Velasco, Bárbara Montes and Miguel Cárdenas.

I cannot finish without thanking my family. I warmly thank and appreciate my parents and my brother for the support they provided me through my entire life. I must acknowledge my close friends, Emilio, Dani, Kitty, Adriana, Elena, Begoña and Sergio, without whose love and encouragement, I would not have finished this thesis.

Contents

Acknowledgments **vii**

1 Introduction **1**

2 Cosmological Preliminaries **5**
2.1 The Smooth, Expanding Universe 5
2.1.1 Hubble's Law 5
2.1.2 Redshift 6
2.2 Theoretical Framework 7
2.2.1 The Metric 7
2.2.2 Einstein Equations 9
2.2.3 Evolution of the Energy 10
2.2.4 Friedmann Equations 12
2.2.5 The Matter Budget Today 12
2.3 Distances Measures in Cosmology 14

3 Cluster as Probes of Cosmic Acceleration **19**
3.1 Clusters 19
3.2 Clusters as Cosmological Probes 21
3.2.1 Evolution of the Cluster Mass function and Clustering of Clusters in Large Area Cluster Surveys 22
3.2.2 Calibration of the Mass Observable Relation. Self Calibration 25
3.3 The Scatter 29
3.4 Observational Considerations 33
3.4.1 Optical Observations 33
3.4.2 X-ray Observation 36
3.4.3 Sunyaev Zeldovich Observation 36

4 The Dark Energy Survey Project **39**
4.1 Overview 39
4.2 Dark Energy Survey Techniques 45

4.3 Clusters in DES 47
4.3.1 Systematics Effects 48

5 Structure Formation and Statistical Description of Density Fluctuations 51
5.1 Introduction 51
5.2 Growth of Inhomogeneities 52
5.2.1 Introduction 52
5.2.2 Results from Newtonian Hydrodynamics in an Expanding Universe. 55
5.2.3 Transfer Function 59
5.3 Power Spectrum 62
5.4 Statistic of Density Fluctuations 63
5.4.1 Two Point Correlation Function and Power Spectrum . 64
5.4.2 Gaussian Density Fields 66
5.4.3 Filtering and Normalization of the Power spectrum . . 67

6 The Abundance of Dark Matter Halos 69
6.1 Introduction 69
6.2 The Spherical Collapse Model and the Mass function 70
6.2.1 The Spherical Top Hat Collapse 70
6.2.2 The Dark Matter Halo Mass Function and the Press Schecther Theory 73
6.3 Halo Mass Function in Numerical Simulation 75
6.3.1 Measures of Halo Mass 75
6.3.2 Fitting Functions 76
6.4 Mass Function for Simulations Used in this Work 81
6.4.1 Mass Function Result in the Hubble Volume Snapshot at z=0 83
6.4.2 Mass Function in DES Light Cone Simulations 84

7 Halo Bias and Clustering 89
7.1 Halo Bias 89
7.1.1 Introduction 89
7.1.2 Linear Bias from Peak Background Split 90
7.1.3 Linear Bias from Excursion Set Approach 91
7.1.4 Linear Bias Improvements 93
7.1.5 The Distribution of Halos at Large scales: Deterministic Biasing 94
7.2 The Halo Model 94
7.2.1 The Two Point Correlation Function and the Power Spectrum 95

7.3 Halo Bias and Two Point Correlation Function estimation in N-body Simulations 99
7.3.1 Two Point Halo Correlation Function Estimation . . . 99
7.3.2 Halo Bias Results in Simulations 112

8 From Halos to Clusters. Measuring the Scatter of the Observable-Mass relation 117
8.1 Halo Model of Galaxy Clustering 117
8.1.1 The Galaxy Correlation Function and Bias 118
8.2 Construction of the Cluster Catalog with a DES volume . . . 119
8.3 Theoretical Predictions of the richness bias using the Halo Model 121
8.4 Likelihood Analysis. Constraining the Scatter 123
8.5 Forecast and Error Estimation for the Scatter on DES volume 124
8.6 Scatter Constraints 129

9 Conclusions 131

A Focal Plane Detectors for Dark Energy Survey 135
A.1 DECam CCDs and the DES Technical Requirements 135
A.2 Packaging and Testing of DECam Detectors at Fermilab . . . 136
A.3 Characterization Techniques 138
A.3.1 Photon Transfer Curve: Gain, Linearity and Full Well Capacity 139
A.3.2 Charge Transfer E ciency 140
A.3.3 Effective Threshold. Output Gate Transfer Curve. . . 144
A.3.4 X-ray calibration 145

B Pro le of Dark Matter Halos 147
B.1 Profile of Dark Matter Halos 147

C Two Point Correlation Function Estimators 149
C.1 Choosing an Estimator 149

Bibliography 155

Chapter 1

Introduction

The discovery of the cosmic acceleration is one most important developments of modern cosmology. It raises fundamental questions about the expanding universe and our understanding of gravity. The cosmic acceleration could arise from the repulsive gravity of dark energy or it may signal that the General Relativity breaks down on cosmological scales and must be replaced. The dark energy term is used for the Einstein's cosmological constant Λ or a component of the universe that varies slowly with time and space and acts like Λ.

The most direct evidence for detection of dark energy comes from observations of supernovae in 1998. The measurements agree with the relativistic cosmological model with non zero Λ and no space curvature. While the dark energy density Ω_Λ has been determined to a precision of a few percent, study its nature by measuring its equation of state parameter, w, is more challenging.

The primary effect of dark energy is on the expansion rate of the universe; this affects the redshift distance relation and the growth of structure. While dark energy has been important at recent epochs, we expect that its effects at high redshift were very small, since otherwise it would have been di cult to large scale structure to have formed in most models (Frieman et al. (2008)).

Apart from the distance measurements using type Ia supernovae, there are other methods that probes dark energy at recent epoch: the weak gravitational lensing of the matter distribution, the galaxy power spectrum studies and the galaxy clusters surveys. A task for scientifics is to construct more sensitive new experiments that employ each of these techniques individually to provide tight and independent constraints on the dark energy equation of state, w.

We will focus on the cluster of galaxies which are the largest virialized objects in the universe. The evolution of their abundance has long been recognized as powerful tool for constraining cosmological parameters, including dark energy (e.g., Eke et al. (1996) and Haiman et al. (2001)).

The idea is to compare the predicted space density of massive halos to the observed space density of clusters, which can be identified via optical, X-ray, or CMB observables that should correlate with halo mass. But this mass estimators are noisy, meaning there can be significant scatter between the observable mass tracer and cluster mass. Since the mass function is a steeply declining function of mass, a low level of scatter can change the shape and amplitude of the observed mass function significantly and degrades the cosmological constraints. Uppscattering of low mass systems into high mass bins can results in a significant boost to the number of systems with apparently high mass (Lima and Hu (2005)).

Scatter arises from physical variations in cluster properties at fixed halo mass, from observational noise, and from low level contamination that produces small random uctuations in the observable. These effects are typically assume to produce a lognormal form of $P(X\ M, z)$, i.e. Gaussian scatter in lnM . The calibration task is then to determine the mean scaling relation and the standard deviation σ_{lnM} called the scatter.

In previous studies, Rozo et al. (2009) constrain the scatter in the mass richness relation at fixed richness of maxBCG cluster sample with weak lensing, optical richness estimates and X ray data. Specifically, they use observational constraints on the mean mass richness relation and the X-ray measurement of the mean and scatter of the X-ray luminosity as a function of richness.

In the next few years, a host of large scale optical surveys, such as Dark Energy Survey (DES) (The Dark Energy Survey Collaboration (2005), the Hyper-Suprime Camera (HSC)(Miyazaki et al. (2006), Takada (2010)) and the Large Synoptic Survey Telescope (LSST) ((LSST Science Collaboration et al. (2009)), are expected to generate galaxy catalogs to su ciently depth to reliable detect galaxies at redshift as high as $z \approx 1$. Oguri and Takada (2011) study how these surveys in conjunction with stacked weak lensing mass calibration, can be used to calibrate the mass observable relation and the scatter and place tight constraints on the cosmological parameters (self calibration method).

In this thesis, we present a cross check method, complementary to previous, to constrain the scatter of the mass richness relation in the DES large optical cluster catalog. We will use the spatial clustering of the cluster themselves, as characterized by the cluster correlation function (Estrada et al. (2009)). Because the bias of halo clustering depend on mass, the amplitude and the scale dependence of clustering provides information about the mass observable relation (Majumdar and Mohr (2004)). However, in our scales of interest the underlying halo-mass bias is scale-independent.

The halo model (Cooray and Sheth (2002a) provides an analytical expression for the bias of halos as a function of halo mass. Then, in order to model the bias for a sample of clusters we need to relate the mass to an easily

observable quantity. In our case we model the bias for a richness threshold. Doing this requires a halo occupation distribution (HOD), where the number of galaxies is specified by the probability distribution $P(N\ M)$. In particular , we use a lognormal distribution with a mean given by an empirical mass richness relation and the standard deviation or scatter, σ_{lnM}. To constrain the scatter in simulations we assign richness to the dark matter halos of the light cone by means of this distribution.

In this thesis, first we will study how the halos are biased respect to the underlying matter distribution using the halo model. It describes the clustering of dark matter halos and the halo abundances. Theoretical models for halo bias have been derived from the mass function (e.g., Mo and White (1996) and Sheth and Tormen (1999)). Sheth and Tormen (1999) generalize the expression for the Press-Schechter mass function and calibrated the free parameters using numerical simulations. Later, Tinker et al. (2010), using higher resolution N-body simulations, also calibrate fitting functions for the large scale bias. In this thesis we study the accuracy of these models using dark matter halo simulations. In particular, we use the DESv1.02 light cone based on the Hubble Volume Simulations SO light cone (Evrard et al. (2002)) that has 5000 deg^2 (DES volume).

Then as we explain before we assign richness to the dark matter halos and study the expected precision to measure the scatter in a DES-like cluster survey.

This thesis is organized as follows. In Chapter 2 we present the seeds of modern observational cosmology (i.e., brief introduction to basic cosmology). We review the Friedmann-Robertson-Walker cosmology and the definition of the different cosmological lengths. In Chapter 3 we describe the clusters as cosmological probes. We explain the importance of the calibration of the mass observable relation with special emphasis on the scatter as a key challenge in extracting precise cosmological constraints. In Chapter 4 we introduce the Dark Energy Survey and the instrument. We summarize the four proposed techniques for probing dark energy, focusing on galaxy clusters and their systematics effects such as the scatter. In Chapter 5 we brie y summarize some of the results which are more relevant for describing structure formation quantitatively in the ΛCDM paradigm. This is intended to form the basis for subsequent chapters, where we will analyze the measurements of the dark matter halos and galaxy clusters distribution. In Chapter 6 we study the models for the abundance of dark matter halos. After we explain the spherical collapse model, we introduce the more accurate calibrated formulas or fitting formulas from N-body simulations. Finally, we test them in N-body simulations. In Chapter 7 we study the accuracy of the model predictions of the linear halo bias by comparing them with results from numerical simulation. To conclude in Chapter 8 we propose a model that connect the halo bias with the bias that is observed in a cluster sample. We explain

our method to constrain the scatter in the mass richness relation for optical surveys using the bias measured with cluster correlation functions. We finish with the forecasts of the performance of the new analysis technique for the Dark Energy Survey galaxy cluster catalog. We end with a summary and conclusions in Chapter 9.

The thesis also includes three appendices. The appendix A describes the work performed on the focal plane detectors for DECam. The appendix B includes a discussion of the profile of dark matter halos and the C summarizes the different studies about the behavior of different the two point correlation function and discuss why the LS is the best option.

Chapter 2

Cosmological Preliminaries

Abstract: This chapter is a brief review of the current cosmological model and the relevant equations for the remainder of the thesis. First we present the seeds of modern observational cosmology. We then introduce the FRW models and the solutions for energy fluids playing an important role in the dynamics at different epochs. We finish with a definition of the different cosmological lengths.

2.1 The Smooth, Expanding Universe

2.1.1 Hubble s Law

Hubble's law was formulated in 1929 by Edwin Hubble when he observed that galaxies move away from us at velocities, $v(t)$, that are proportional to their distance from us, d (Hubble (1929))

$$v(t) = H(t)d = \frac{\dot{a}}{a}d \tag{2.1}$$

where $H(t)$ is the Hubble parameter, which measures how rapidly the scale factor changes. For nearby galaxies and for present epoch

$$v = H_0 d \tag{2.2}$$

where H_0 is the Hubble constant at current time t_0. The dimensions of H_0 are inverse time[1], but it is usually written

$$H_0 = 100\,h\,kms^{-1}\,Mpc^{-1} \tag{2.3}$$

[1] $1Mpc = 3.09 \times 10^{24}$ cm $= 3.26 \times 10^6$ light years

where h is a dimensionless number that parameterizes the uncertainty on H. The reciprocal of H_0 is Hubble time and the speed of light c times the Hubble time is the Hubble distance D_H

$$D_H \equiv \frac{c}{H_0} = 3000\, h^{-1}\, Mpc \tag{2.4}$$

The Hubble diagram (Figure 2.1) is still the most direct evidence we have that the universe is expanding.

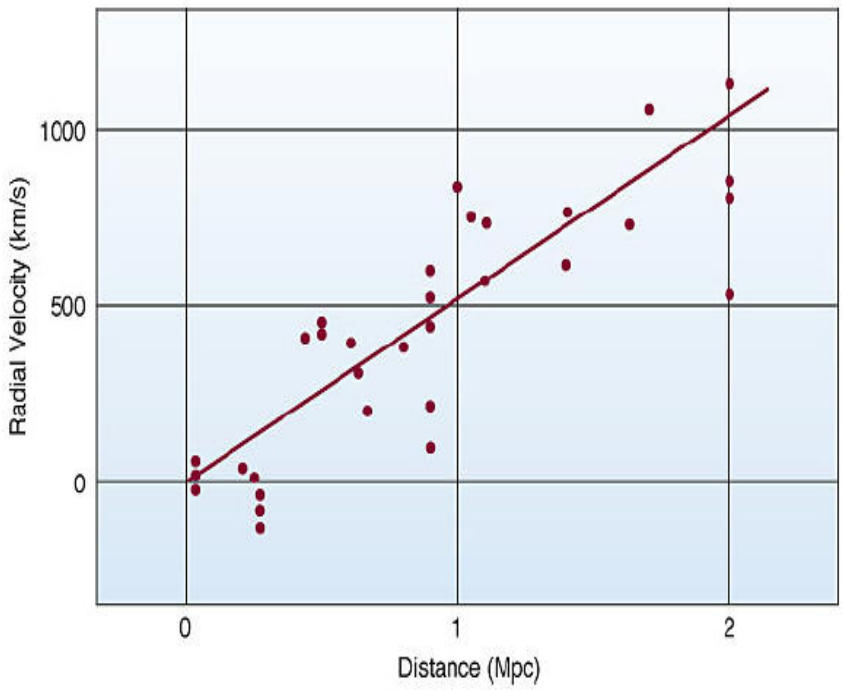

Figure 2.1: The Hubble Diagram (Hubble (1929). Velocities of distant galaxies are plotted versus distance. The solid line is the best fit to the filled points which are corrected from the sun's motion.

2.1.2 Redshift

If the universe is expanding, then galaxies should be moving away from each other. We should therefore see galaxies receding from us. We do not observe directly the recession velocity of a galaxy, but the changes in the spectra. Because the Doppler, the light emitted from receding galaxies with frequency ν_e arrives to us with lower frequency ν_0. The observed shift of the frequency (or wavelength) of the spectra is described by a parameter z called redshift:

$$z + 1 \equiv \frac{\lambda_0}{\lambda_e} \tag{2.5}$$

For low redshifts, or small v/c, in the standard Doppler formula applies and

$$z \approx \frac{v}{c} \tag{2.6}$$

So a measurement of the amount by which absorption and/or emission lines are redshifted is a direct measurement of how fast the structures in which they reside are receding from us.
In terms of cosmography, also for small velocities or small changes in frequencies

$$1 + z = \frac{1}{a} \tag{2.7}$$

Thus, we will use this expression to determine the scale factor at the moment the light was emitted.

2.2 Theoretical Framework

The Friedmann-Robertson-Walker (FRW) cosmological model provides the context for interpreting the observational evidence for the acceleration of the universe as well as the framework for understanding how cosmological probes in the future will help uncover the cause of acceleration by determining the history of the cosmic expansion with greater precision.

It consist in two ingredients, the geometry of the curved space (its metric) and the assumptions about the physical content of the Universe. Therefore, we will be familiar with the concept of metric, understand geodesic, and be able to apply Einstein equations to the FRW metric thereby relating the parameters in the metric to the density of the universe.

Note that we will follow the standard practice of using units in which the speed of light $c = 1$.

2.2.1 The Metric

The metric turns coordinate distance into physical distance and so will be an essential tool to make quantitative predictions in a expanding universe.

The space time metric plays a fundamental role in relativity. It turns observer-dependent coordinates into invariants

$$ds^2 = \sum_{\mu\nu}^{3} g_{\mu\nu} dx^\mu dx^\nu \tag{2.8}$$

where ds is the distance between two nearby points (events) with coordinates $\bar{x}$ and $\bar{x} + d\bar{x}$ and $g_{\mu\nu}$ is the metric tensor. The indices μ and ν range from 0 to 3, with the first one reserve for the time coordinate ($dx^0 = dt$) and the last three for spatial coordinates. Therefore, the metric $g_{\mu\nu}$ provides the

connection between values of the coordinates and the more physical measure of the interval ds^2.

The great advantage of the metric is that it incorporates gravity. We can include gravity in the metric and talk about particles moving freely in a distorted or curved space time. How the metric depends of the position is determined by the distribution of matter and energy in the Universe.

From the large scale distribution of galaxies and the near-uniformity of the CMB temperature, we have good evidence that the universe is nearly homogeneous and isotropic. Under this assumption, the space time metric can be written in the FRW form in terms of the expansion of the universe, or the scale factor $a(t)$,

$$ds^2 = dt^2 - a(t)^2\Big(\frac{dr^2}{1-kr^2} + r^2 d\theta^2 + r^2 sin^2\theta d^2\phi\Big) \tag{2.9}$$

where r, θ and ϕ are comoving spatial coordinates and t is time. The quantity k is the curvature of the Universe which is measured to be very close to zero (Komatsu et al. (2011)).

It will be useful to rewrite the last equation in terms of a new distance coordinate, χ, called comoving distance. If

$$d\chi = \frac{dr}{\sqrt{1-kr^2}} \tag{2.10}$$

we obtain

$$ds^2 = dt^2 - a(t)^2[d\chi^2 + f_k^2(\chi)(d\theta^2 + sin^2\theta d\phi^2)] \tag{2.11}$$

where

$$f_k = \begin{cases} sin\chi & k=+1 \quad spherical \quad or \quad closed \\ \chi & k=0 \quad Euclidean \quad or \quad flat \\ sinh\chi & k=-1 \quad hyperbolic \quad or \quad open \end{cases}$$

The symmetries of the Universe have reduced to a single function of time, the scale factor $a(t)$, and a curvature parameter k.

At least, in a at Universe ($k = 0$), the metric is almost identical to the Minkowski metric, except that distance must be multiplied by the scale factor. Therefore, the metric in a expanding, at Universe is

$$g_{\mu\nu} = \begin{pmatrix} -1 & 0 & 0 & 0 \\ 0 & a^2(t) & 0 & 0 \\ 0 & 0 & a^2(t) & 0 \\ 0 & 0 & 0 & a^2(t) \end{pmatrix}$$

To summarize, the smooth universe can be describe with the FRW metric, which implies that physical distances are related to comoving distance with

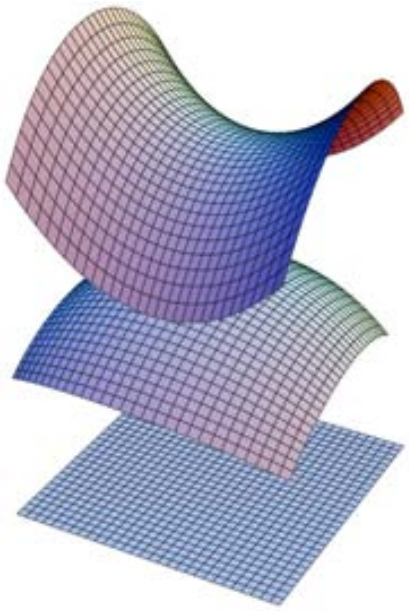

Figure 2.2: From bottom to top: at, spherical and hyperbolic curvature of a 2D plane.

the time dependent scale factor $a(t)$. Therefore, the comoving distance, χ remains fixed as the universe expands and the physical distance, x grows simply because of the expansion and is proportional to the scale factor $x = a\chi$ (see Section 2.3 for more definitions of comoving distances).

2.2.2 Einstein Equations

To determine the evolution of the scale factor $a(t)$ we need to use the Einstein equation

$$G_{\mu\nu} = 8\pi G\mathcal{T}_{\mu\nu} \tag{2.12}$$

This relates the metric to the matter and energy of the universe, how the space-time $G^{\mu\nu}$ of the FRW Universe is curved by the presence of matter and energy $T^{\mu\nu}$. Here $G_{\mu\nu}$ is the Einstein tensor which is formed from the metric tensor $g_{\mu\nu}$, which depends on the metric and its derivatives, G is the Newton constant; and $T_{\mu\nu}$ is the energy-momentum tensor that describes the physical content of the universe.

First we will discuss possible forms of the cosmological energy-momentum tensors $T_{\mu\nu}$ and then using the Einstein tensor $G_{\mu\nu}$ for the FRW background we solve the evolution of the scale factor as a function of the matter content.

2.2.3 Evolution of the Energy

The conservation laws for the energy-momentum tensors $T_{\mu\nu}$ in general relativity implies the vanishing of the covariant derivative. Therefore, in a expanding universe, the continuity equation reads (Dodelson (2003))

$$\dot{\rho} = -3\frac{\dot{a}}{a}(p+\rho) \tag{2.13}$$

Rearranging terms, for each component the conservation of energy is expressed by

$$d(a^3\rho_i) = -p_i da^2 \tag{2.14}$$

analogue of the first law of the thermodynamic, $dE = -pdV$.

The conservation law can be applied immediately to glean information about the scaling relation of both matter and radiation with the expansion. Once the equation of state, $w_i \equiv \frac{p_i}{\rho_i}$, is specified for each energy component of the universe, the evolution of the energy density can be predicted.
For the general case, w_i varies with time, and the evolution of the energy density in a given component is given by,

$$\rho_i \quad exp\Big[3\int_o^z [1+w_i(z')]dln(1+z')\Big] \tag{2.15}$$

In the case of constant w_i,

$$\rho_i \quad (1+z)^{3(1+w_i)} \tag{2.16}$$

2.2.3.1 Cosmic Inventory

Since the Universe is a mixture of different components, here we will classify the different sources by their contribution to the pressure.

Non relativistic matter, which includes both dark matter and baryons, has effectively zero pressure, so $w_m = 0$ and

$$\rho_m \quad (1+z)^3 \tag{2.17}$$

For **radiation**, i.e. relativistic particles, $p = \rho/3$ so $w_r = \frac{1}{3}$ and the energy density of radiation

$$\rho_r \quad (1+z)^4 \tag{2.18}$$

Dark energy

There is evidence pointing toward the existence of something beyond the matter and radiation described before. They are not enough to describe the evolution of the universe.

Observations made by two teams (Riess et al. (1998), Perlmutter et al. (1999)) revealed that distant supernovae appear fainter than they should

given a purely matter dominated expansion, suggesting that the Universe has entered an epoch of accelerated expansion. In order to explain these observations, we are required to introduce a late-time acceleration into our cosmological model in the form of a cosmological constant Λ (see Figure 2.3). When analyzed assuming a Universe with matter and cosmological constant, their results provided evidence for $\Omega_\Lambda > 0$ at greater than 99% confidence (Frieman et al. (2008)).

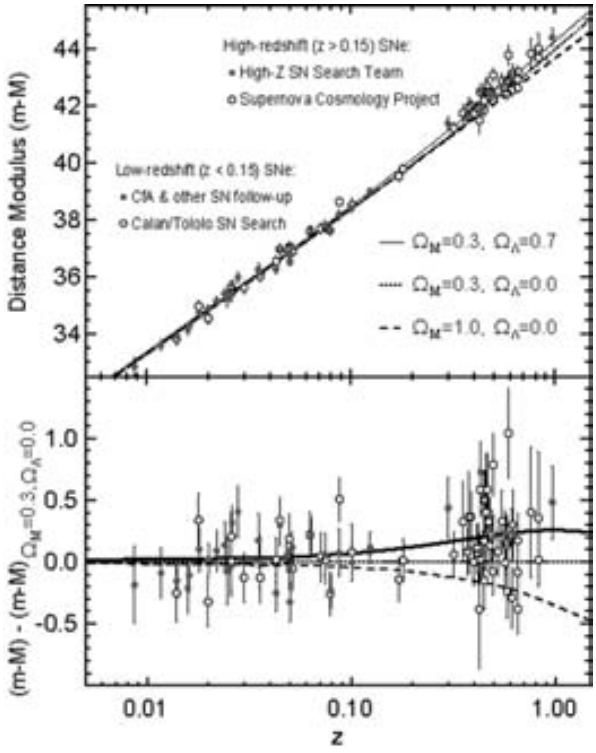

Figure 2.3: Hubble diagram of SNe Ia measured by the Supernova Cosmology Project and the High-z Supernova Team. Bottom panel shows residuals in distance modulus relative to an open universe with $\Omega_M = 0.3$. Figure based on Riess et al. (1998), Perlmutter et al. (1999).

For dark energy, the only way to satisfy Equation 2.13 with constant energy density is if the pressure is equal to $-\rho$. So $w = -1$. For other model of dark energy, w can differ from -1 and vary in time.

Einstein first introduced a cosmological constant term Λ into his field equations in 1917 to achieve a static Universe. He later removed it when Hubble observed that the Universe is expanding, since it was no longer required. In recent years however, Λ has been re-introduced into the field equations to accommodate the accelerated expansion. It is by far the simplest model that can be constructed to explain current observations and is

obtained by adding a cosmological constant term Λ to the Einstein de-Sitter matter model. The left hand side of the Equation 2.12 isn't uniquely defined. We can add the term $-\Lambda g_{\nu\mu}$, for some constant Λ, without changing the conservation of the stress tensor, ${}^{\nu}T_{\nu\mu} = 0$. In other words, we could have written the Einstein equation as

$$G_{\mu\nu} - \Lambda g_{\mu\nu} = 8\pi G \mathcal{T}_{\mu\nu} \tag{2.19}$$

The failure of quantum field theory to explain the size of the observed dark energy has lead theorist to consider more exotic possibilities.

Until now, we have only considered models that contain an additional term in the stress-energy tensor which have the properties required to account for the late-time acceleration of the Universe. An interesting alternative approach is to modify the geometrical part of the Einstein equation (modifications of general relativity).

2.2.4 Friedmann Equations

The key equation of cosmology are the Friedmann equations, the field equations of general relativity (Equation 2.12) for the FRW metric (Equation 2.9) combined with energy-momentum tensor,

$$H^2 = \left(\frac{\dot{a}}{a}\right)^2 = \frac{8\pi G\rho}{3} - \frac{k}{a^2} \tag{2.20}$$

$$\frac{\ddot{a}}{a} = -\frac{4\pi G}{3}(\rho + 3p) \tag{2.21}$$

where ρ is the total energy density of the universe and p is the total pressure (sum of pressures of each component).

In a FRW background and using the modified form of Einstein's Equations 2.19 the Friedmann equations are given by:

$$H^2 = \left(\frac{\dot{a}}{a}\right)^2 = \frac{8\pi G\rho}{3} - \frac{k}{a^2} + \frac{\Lambda}{3} \tag{2.22}$$

$$\frac{\ddot{a}}{a} = -\frac{4\pi G}{3}(\rho + 3p) + \frac{\Lambda}{3} \tag{2.23}$$

In this model, after the matter dominated era, we will enter a dark energy dominated era.

2.2.5 The Matter Budget Today

In order to know the past and future evolution of the Universe, it would be enough to measure the present density of radiation, matter and Λ, and also to measure H_0, the Hubble constant. Then, thanks to the Friedmann equation (2.22), it would be possible to extrapolate $a(t)$ at any time.

The critical density $\rho_c(z)$ is defined as the density required to produce zero spatial curvature (k=0). In that case the total density of matter, radiation and Λ is equal at any time to the critical density

$$\rho_c(z) = \frac{3H^2(z)}{8\pi G} \tag{2.24}$$

The present value of the critical density is

$$\rho_{c,0} \equiv \frac{3{H_0}^2}{8\pi G} = 2.78h^{-1}10^{11}M_\odot(h^{-1}Mpc)^{-3} = 1.88h^2 10^{-26}kgm^{-3} \tag{2.25}$$

The density of different forms of energy density can then be written in units of this critical density today

$$\Omega_{i,0} \equiv \frac{\rho_{i,0}}{\rho_{c,0}} = \frac{8\pi G}{3}\rho_{i,0} \tag{2.26}$$

and

$$\Omega_\Lambda = \frac{\Lambda}{3{H_0}^2} \tag{2.27}$$

The Friedman equation, 2.22, can then be written,

$$H^2 = H_0^2\Big[\Omega_{r,0}a^{-4} + \Omega_{m,0}a^{-3} - \frac{k}{H_0^2}a^{-2} + \Omega_{\Lambda,0}\Big] \tag{2.28}$$

where we can define the curvature density parameter

$$\Omega_k = \frac{k}{H_0^2} \tag{2.29}$$

At redshsit $z = 0$, the equation 2.28 is

$$1 = \Big[\Omega_{r,0} + \Omega_{m,0} - \frac{k}{H_0^2} + \Omega_{\Lambda,0}\Big] \tag{2.30}$$

The equation for the evolution of the scale factor a(t), the Friedmann equation 2.22 is rewrite for constant w_i

$$H^2 = {H_0}^2\Big[\sum_{i=0}^{N}\Omega_{i,0}a^{-3(1+w_i)} + \Omega_k a^{-2} + \Omega_\Lambda] \tag{2.31}$$

Thus, knowing the energy content of the universe, you can get the time evolution.

Observations of the cosmic microwave background (add reference) and the large scale structure find that the universe is consistent with being at. Figure 2.4 shows the time evolution of the different energy densities for a at universe, how the different terms in Equation 2.22 vary with the scale factor. While today matter, and possibly cosmological constant dominate the universe, early on, radiation was the dominant constituent of the universe.

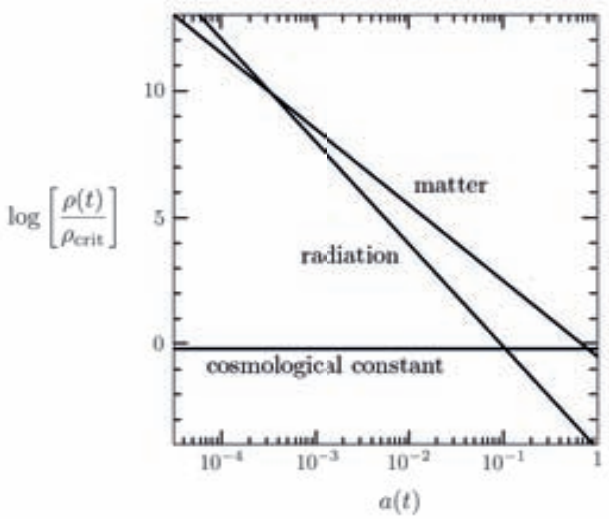

Figure 2.4: Energy density versus scale factor for different constituents of a at Universe (Dodelson (2003)).

2.3 Distances Measures in Cosmology

One very important comoving distance is the **comoving horizon** defined as the total portion of the universe visible to the observer. In other words, the distance that light could have traveled (in the absence of interactions) since $t = 0$. This is usually expressed as a time, the conformal time, η. If light travel a comoving distance, it is given by

$$\eta \equiv \int_0^t \frac{dt'}{a(t')} \tag{2.32}$$

where $d\eta = dx/a = ct/a$ ($c = 1$) and dx is the physical distance.

The regions of the sky that are separated by a distance greater that η are not causally connected. The causally connection implies $ds^2 = 0$. For the FRW Equation 2.9, in spherical coordinates with θ and ϕ constants:

$$\chi = \int_0^r \frac{d\mu}{\sqrt{1-k\mu^2}} = \int_{t(a)}^{t_0} \frac{dt'}{a(t')} = \int_a^1 \frac{da'}{a'^2 H(a')} \tag{2.33}$$

which is the distance between a distant emitter and us in which the expansion of the universe is factored out, which is called the **line of sight comoving distance**. We have change the integration over t' to one over z' using $H = (\frac{\dot{a}}{a})^2$) and $z = 1/(a-1)$.
Let us introduce now the normalized Hubble function $E(z)$ by

$$H(z) = E(z)H_0 \tag{2.34}$$

Using Equation 2.7 and 2.20 with constant w_i

$$E(z) \equiv \sqrt{\Omega_r(1+z)^4 + \Omega_M(1+z)^3 + \Omega_k(1+z)^2 + \Omega_\Lambda(1+z)^{3(1+w_i)}} \tag{2.35}$$

and the equation 2.33

$$\chi = \int_0^z \frac{dz'}{H(z)} \tag{2.36}$$

Note that this comoving distance χ depends of the matter and energy density of the Universe. The current contribution of the species to the total energy density, as measured from the Cosmic Microwave Background, is $\sim 10^{-4}$ times smaller than that of matter ad dark energy. Consequently the radiation term Ω_r is often neglected.

χ is is the fundamental distance measure in cosmography since, all others are quite derived in terms of it. Now the **causal or particle horizon**,d_H is given by:

$$d_H = a(t)\chi \tag{2.37}$$

The comoving distance between two events at the same redshift or distance but separated on the sky by some angle $\delta\theta$ is $\chi\delta\theta$ and the **transverse comoving distance** D_M is simply related to the line of sight comoving distance χ (Hogg (1999))

$$D_M = \begin{cases} \frac{c}{H_0}\frac{1}{\sqrt{\Omega_k}} sinh[\ \sqrt{\Omega_k}\chi\frac{H_0}{c}] & k = +1 \\ \chi & k = 0 \\ \frac{c}{H_0}\frac{1}{\sqrt{|\Omega_k|}} sin[\sqrt{\ \Omega_k\ }\chi\frac{H_0}{c} & k = -1 \end{cases}$$

The **angular diameter distance** d_A is defined as the ratio of an object's physical transverse size l to its angular size θ. It is used to convert angular separations in telescope images into proper separations at the source. Assuming that the angle is small, it is given by

$$d_A = \frac{l}{\theta} \tag{2.38}$$

In the at Friedman Universe it is related to the transverse comoving distance by

$$d_A = \frac{D_M}{1+z} \tag{2.39}$$

Another way of inferring distance in astronomy is to measure the ux F from an object of known absolute luminosity L (standard candle). Flux and luminosity are related through

$$F \equiv \frac{L}{4\pi d^2} \tag{2.40}$$

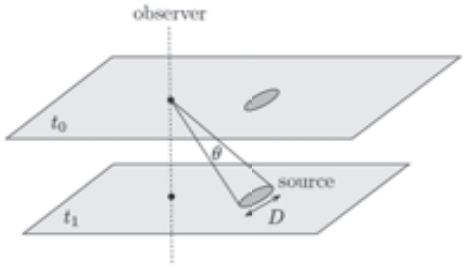

Figure 2.5: Geometry associated with the definition of angular diameter distance (D=l for Equation 2.38)

since the total luminosity through a spherical shell with area $4\pi d^2$ is constant. Because of expansion, the energy per unit time passing through a comoving shell a distance $\chi(a)$ from the source will be a factor of a^2 smaller than the luminosity at the source. Then the ux we observe will be

$$F = \frac{La^2}{4\pi\chi^2(a)} \tag{2.41}$$

where L is the luminosity at the source. We can keep Equation 2.40 in an expanding universe as long as we define the **luminosity distance** in a at universe

$$d_L \equiv \frac{\chi}{a} \tag{2.42}$$

Figure 2.7 shows the redshift dependence of the three distance measures d_m or χ, d_L and d_A. Note that all three distances are larger in a universe with dark energy (in a form of a cosmological constant Λ) than in one without. As we explain before, this fact was employed in the discovery of dark energy.

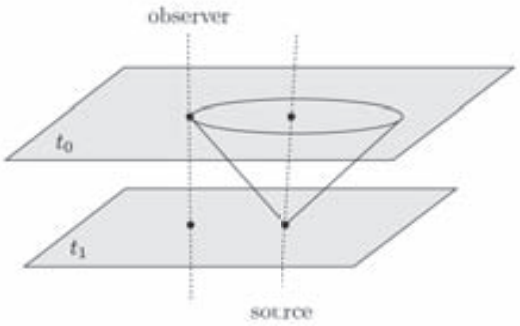

Figure 2.6: Geometry associated with the definition of luminosity distance

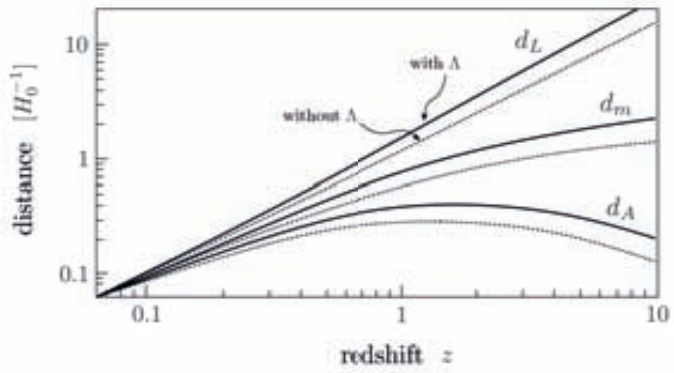

Figure 2.7: Distances measures in a at Universe (Dodelson (2003)), with matter only (dotted lines) and with 70% dark energy (solid lines). In a dark energy dominated universe, distances out to a fixed redshift are larger than in matter universe.

Chapter 3

Cluster as Probes of Cosmic Acceleration

Abstract: After an introduction to galaxy cluster we describe the clusters as cosmological probes. We explain the importance of the calibration of the mass observable relation as a key challenge in extracting precise cosmological constraints. We emphasize in the scatter of the mass observable relation. Finally, we will summarize the observational techniques to measure the mass of the clusters, in particular in the optical observable.

3.1 Clusters

Clusters of galaxies play an important role in observational cosmology. They are the most massive gravitationally bound structures in the Universe and therefore mark the most prominent density peaks of the large scale structure. Originally, clusters were characterized as such by the observed spatial concentrations of galaxies. Today, we know that although the galaxies determine the optical appearance of a cluster, the mass contained in galaxies contributes only a small fraction to the total mass of a cluster. It was discovered that galaxy clusters are intense sources of X-ray radiation which is emitted by a hot gas located between galaxies. This intergalactic gas (inter-cluster medium, ICM) contains more baryons than the stars seen in the member galaxies.

Typical galaxy clusters posses masses of the order of $10^{14} M_{\odot}$ and radio of $\sim 2Mpc$. The mass of the clusters consist of $\sim 3\%$ contributions from stars in galaxies and $\sim 15\%$ from intergalactic gas, whereas the remaining $\sim 80\%$ consist of dark matter which dominates the mass of the clusters. We deduce the existence of dark matter in galaxy clusters that dominates the

cluster mass from the dynamics of galaxies, from the properties of the X-ray emission of the clusters, and from the gravitational lens effect (Schneider (2006)).

The formation of galaxy clusters involves several steps, starting from the collapse of dark matter halos, followed by the occupation of such haloes by baryons and the formation of galaxies. Once formed, they are driven again by gravity and merge to compose the largest structures that can be approximately considered in virial equilibrium. Small sub-galactic objects are first to decouple, collapse a virialize. These small objects then collect into galaxies, and galaxies later collect into clusters of galaxies, whose masses now top out at roughly 10^{14} times that of the sun's. Thus, the growth and development of clusters directly traces the process of structure formation in the universe.

Clusters of galaxies are also the largest astrophysical laboratories in the Universe. Halos are multicomponent systems consisting of dark matter and baryons in several phases:black holes; stars; cold, molecular gas; warm/hot gas; and non-thermal plasma. The merging process is of considerable interest for cluster studies, driving astrophysical signatures that can test physicals models from the nature of dark matter to the magnetohydrodynamics of hot, dilute plasmas. But, merging also potentially confuses cosmological studies, by creating halo pairs that may appear as one cluster in projection and by introducing variance into observable signals (Allen et al. (2011)).

Therefore, various astrophysical processes play out within the photon-baryon components of the evolving cosmic web, including hydrodynamic, magnetohydrodynamics and radiative transfer effects. Except for the immediate vicinity of the black holes, these processes involve classical physics that is largely known (Allen et al. (2011)).

On the theory side, modeling the development of galaxies and the ICM medium within a cosmological framework of hierarchical clustering poses a formidable task. Although the physical processes are now firmly in hand, the complex, nonlinear interactions that govern their time evolution are analytically intractable. After decades of study via N-body and hydrodynamic simulations and related methods (see Borgani and Kravtsov (2009)), models for the detailed evolution of the baryons in clusters are growing in capability to describe an increasingly large and rich volume of observations.

Hydrodynamics simulations are computationally expensive and they still have many discrepancies with data. This leads to the necessity to implement semi-analytic or empirical models(Baugh (2013)). As we will see in Chapter 8, in this thesis we will populate dark matter halos with galaxies with an empirical model of Halo Occupation Distribution (HOD). Then, the number of galaxies will be specified by HOD or the probability distribution $P(N\ M)$ for a a halo of fixed virial mass M contains N galaxies. We will combine cosmological N-body simulations and an optical cluster richness mass relation

based on optical observations (see Section 3.4.1.2) for the construction of our cluster catalogs. We will implement empirical models, which in our case of galaxy clusters refers to the richness mass relation, such that the the mock catalogues match the observed properties of these objects.

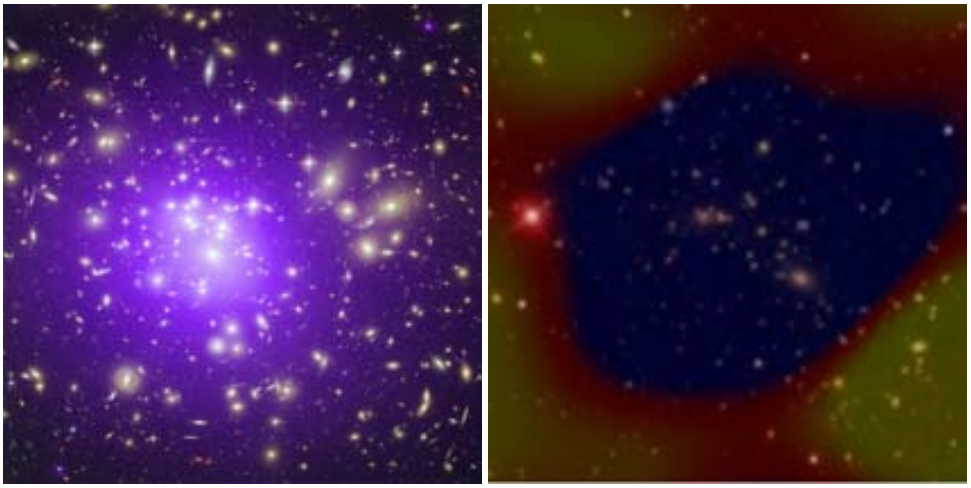

Figure 3.1: Left panel: composite X-ray/optical image of the galaxy cluster Abell 1689, located at redshift z = 0.18. The map shows an area of 556 kpc on a side. The purple diffuse halo shows the distribution of gas at a temperature of about 108 K, as revealed by the Chandra X-ray Observatory. Images of galaxies in the optical band, colored in yellow, are from observations performed with the Hubble Space Telescope. The long arcs in the optical image are caused by gravitational lensing of background galaxies by matter in the galaxy cluster, the largest system of such arcs ever found (Credit:X-ray: NASA/CXC/MIT; Optical: NASA/STScI). Right panel: optical image of cluster Abell 1914 from the Sloan Digital Sky Survey with the superimposed map of the temperatures of the Cosmic Microwave Background observed by the Sunyaev-Zeldovich array (SZA). The image illustrates the effect of up-scattering of the CMB photons by the hot ICM from low frequencies to higher frequencies. At the frequency of observation, the cluster appears as a temperature decrement in the CMB temperature map. (Credit: John Carlstrom and SZA collaboration).

3.2 Clusters as Cosmological Probes

Cluster of galaxies have a long history as cosmological probes (Weinberg. et al. (2013)). They provide the first line of evidence for the existence of dark matter (Zwicky (1933)), and cluster mass-to-light ratio measurements suggested that the matter density of the universe was subcritical ($\Omega_m < 1$) as far as the early 1970's (Gott et al. (1974)).

The evidence for low Ω_m was substantially strengthened by baryon fraction measurements (e.g., Briel et al. (1992)), and by the discovery of massive clusters at high redshift ($z \approx 0.8$) later that decade (Donahue. et al. (1998)). This last discovery presaged the ultimate discovery of dark energy from Type Ia supernova (SNIa) surveys .

Today, clusters remain an important cosmological tool, capable of testing cosmology in a variety of ways. Here we focus on cluster abundances, the clustering of cluster and weak lensing. In these studies is very important understanding the systematics effects associated with the use of directly observable quantities as proxies for mass. In Chapter 6 and 7 will study the halo abundance and clustering of halos respectively and later we will connect them with cluster observable, X.

The abundance of clusters of galaxies is now well established as a standard cosmological probe. It is sensitive to the amplitude of the matter power spectrum σ_8 (see definition in detail in Section 5.4.3), the matter density Ω_m and the comoving volume element dV.

The mean matter content of a sphere of radius $8h^{-1}Mpc$ is $\approx 2\times10^{14}M_{\odot}$. Thus, cluster-mass halos form from the gravitational collapse of uctuations of about this scale, and their abundance naturally tracks σ_8 (i.e., Eke et al. (1996)).

The quantity most tightly constrained by cluster abundance is a combination of the form $\sigma_8\Omega_m^q$, with $q \approx 0.4$ (White et al. (1993)). This degeneracy between σ_8 and Ω_m can be broken in many ways. First, one can simply measure Ω_m or σ_8 in some other way. Second, one can measure the evolution of the cluster mass function over a range of masses and rely on a precise measurement on the mass function's shape assuming that the CDM power spectrum (see section 5.3) is valid. Or, third, one can measure the evolution of the cluster mass function with redshift, which is highly sensitive to Ω_m. This last quantity can be extracted from large solid angle surveys that deliver tens of thousands of clusters. Notice that the statistical power of cluster surveys is ultimate limited by the total number of clusters in the observable universe, which is of order of 10^5 (Voit (2005)).

3.2.1 Evolution of the Cluster Mass function and Clustering of Clusters in Large Area Cluster Surveys

Within the context of the CDM paradigm, the number density of cluster-sized dark matter halos as a function of redshift and halo mass can be accurately predicted from N-body simulations (e.g., Jenkins et al. (2001) and Tinker et al. (2008)). Comparing these predictions to large-area cluster surveys that extend to high redshift ($z \geq 1$) can provide precise constraints on the cosmic expansion history (Haiman et al. (2001)).

For a given cluster sample we can measure the number of clusters dN

within a given solid angle $d\Omega$ and a redshift interval $[z, z + dz]$ that fall into the range $[X, X + dX]$ of the observable. With full knowledge of the mass observable relation $P(X\ M, z)$ as a function of redshift z and the selection function $f(X, z)$ we can derive the redshift distribution

$$\frac{d^2N(z)}{d\Omega dz} = \frac{1}{H(z)}\left(\int_0^z dz' \frac{1}{H(z')}\right)^2 \int_0^\infty f(X,z)dX \int_0^\infty dM \frac{dn(M,z)}{dM} P(X\ M,z) \tag{3.1}$$

This evolution of clusters with redshift would then provide strong constraints on cosmological models through both the comoving volume factor $d^2V/d\Omega dz$ and the mass function evolution factor $\frac{dn}{dM}$. The volume surveyed is the first term multiplying the integral in Equation 3.1)

Evolution of mass function is high sensitive to cosmology because the matter density controls the rate at which structure grows. As we will see in Chapter 6, the evolution of the mass function is controlled entirely by the growth function $D(z)$, which is well defined function of Ω_m, Ω_Λ and w. The effect of how change the growth factor manifest itself most strongly in high-mass clusters because they are the latest objects to form in a hierarchical cosmology with CDM power spectrum (Eke et al. (1996)).

Dependence on the mass function on Ω_Λ and w is a little more subtle. Haiman et al. (2001) showed that with future large surveys it should be possible to obtain precise measurements of the amount Ω_Λ and w. These parameters affect mass function evolution by altering the redshift at which $\Omega_m(z)$ departs significantly from unity for a given value of Ω_m at $z = 0$. The time at which dark energy begins to dominate the dynamics of the universe is later for both larger values of Ω_Λ and smaller (more negative) values of w, leading to greater evolution of the mass function between $z = 1$ and the present (e.g., Battye and Weller (2003)).

The sensitivity of the cluster redshift distribution to w for the South Pole Telescope (Ruhl et al. (2004)) and the Dark Energy Survey (see Chapter 4) is illustrated in Figure 3.2 for 3 at cosmologies with fixed $\Omega_m = 0.3$ and $\sigma_8 = 0.9$ (Mohr (2005)). Three redshift distribution for Sunyaev Zeldovich effect (SZ effect) cluster survey are shown; each correspond to a different value of w. The volume sensitivity dominates at intermediate redshift $z < 0.6$, and the growth rate sensitivity dominates at high redshift, $z > 0.6$. Note that for models with higher w there is less volume, reducing the number of clusters at $z = 0.6$, and structures grows less rapidly, increasing the number of clusters at higher redshift.

For large solid angle cluster surveys, there are additional observables including the spatial two-point correlation function of clusters (autocorrelation function) and their Fourier transform, the power spectrum, which we explain in detail in Section 5.4. The strong cluster correlation (Bahcall and Soneira (1983)) was the first to reveal the universe of large scale structures

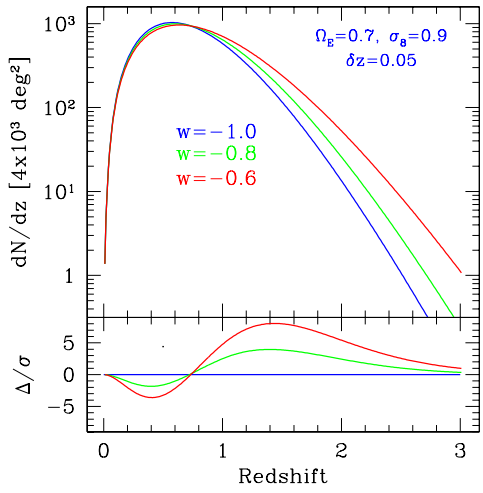

Figure 3.2: The expected redshift distribution (top) and quantified differences (bottom) for models where only the dark energy equation of state parameter w is varied. These models are all normalized to produce the same local abundance of galaxy clusters. Lower panel shows differences between the models relative to the statistical errors (Mohr (2005)).

to $\sim 50h^{-1}Mpc$ or more.

Galaxy clusters, like other cosmic objects, act as tracers of the underlying dark matter. The exact relationship between the cluster autocorrelation function and the dark matter autocorrelation function is well understood theoretically (e.g., Mo and White (1996)), and this relationship or biasing is function of cluster mass. Thus, measurements of the cluster correlation function provide important additional information about cosmology and cluster masses.

Finally direct measurements through weak lensing provide important additional leverage on cosmology on cluster masses.

Combination of these observables (clustering and abundances) and the weak lensing method will be discussed below (see next Section 3.2.2).

3.2.1.1 Additional Cosmological Information from Clustering

Here we will brie y describe some techniques that provide cosmological information with the clustering of clusters although these are beyond the scope of this thesis.

The broadband shape of the power spectrum is sensitive to the shape parameter $\Gamma = \Omega_m h$ (see Section 5.2.3.1), and thus is useful to establish the currently favored low matter density concordance model, as well as the

amount of baryons in relation to the total matter $f_b = \frac{\Omega_b}{\Omega_m}$. .

In addition to the precise measurement of the fullshape of the two point correlation function and the power spectrum , the spatial distribution of clusters can be employed in a simpler way by using the baryonic acoustic oscillation (BAO) signature as a probe of cosmic distance (see Section 5.2.3.1). Estrada et al. (2009) and Hütsi (2007) respectively analyzed the correlation function and power spectrum of clusters in the optically selected maxBCG catalog (see Section 3.4.1), finding a weak detection of the BAO peak. Recently, Balaguera-Antolínez et al. (2011) found no significant signal of the peak in the smaller X-ray selected REFLEX II power spectrum.

3.2.2 Calibration of the Mass Observable Relation. Self Calibration

Testing cosmology with the evolution of the cluster abundance requires that the theoretical mass function be transformed via the observable mass scaling relation, $P(X\ M, z)$, and a model of the selection process for distribution of clusters in the space of survey observables, $f(X, z)$ (e.g., X-ray ux and redshifts).

In addition to form and calibration of the core of the mass observable relation and the determination of the selection function, we can identify several sources of potential systematics uncertainties: errors in cluster redshift, incompleteness and purity (see Section 3.4.1) and the theoretical predictions of the mass function, $\frac{dn(z)}{dM}$. Here we will focus in the calibration of the scaling relation although we will also study the theoretical predictions in detail in next chapters.

The goal is to characterize the observable mass relation $P(X\ M, z)$. Popular choices of such observables include X-ray luminosities (e.g., Reiprich and Böhringer (2002), Mantz et al. (2008) and Rykoff et al. (2008)), X-ray temperatures (e.g.,Finoguenov et al. (2001)), optical richness and weak lensing shear (e.g., Johnston et al. (2007), Rykoff et al. (2008), Leauthaud et al. (2010) and Oguri and Takada (2011)) or the Sunyaev-Zel'dovich (SZ) effect (e.g., Bonamente et al. (2008)). In Section 3.4 we will explain more in detail the observables properties of clusters that enables us to measure their masses and the scaling relations. Since we are interested more in photometric cluster surveys, we will describe more in detail the optical properties and the red sequence method to detect clusters.

$P(X\ M, z)$ is the probability that a halo of mass M at redshift z is detected as a cluster with observable X. This relation is usually described by parameters that specify the mean relation, the variance or the standard deviation (the scatter) and perhaps a measure of the skewness or kurtosis, all of which can evolve with redshift. In this thesis we will discuss and emphasize in the scatter and the impact on cosmological constraints.

There are three general approaches to determine these parameters and address the di culties to calibrate the observable mass relation: simulations, direct method and statistical calibration. The direct method uses weak lensing and/or X ray hydrostatic mass estimates with a small subset of galaxy clusters (e.g., Voit (2005)).

Existing cluster cosmology constraints of $\sigma_8\Omega_m^q$ have come primarily from X-ray data (e.g., Schuecker et al. (2003)) where the X-ray observables can be related to mass via simulations and/or analytic approximations and by hydrostatic modeling for well observed clusters (e.g., Vikhlinin et al. (2009)). Cosmological analysis from optical samples have been typically less constraining because of the uncertain weak lensing mass calibration (Weinberg. et al. (2013)).

The final approach to calibrate the mass observable relation is statistical. Instead of relying on precise mass estimates of a subsample of galaxy clusters, the relation is calibrated using a large cluster sample complemented with statistical properties of the clusters that are sensitive to mass. Thus, we can simultaneously fit for cosmology and the observable mass relation. These types of analyses are often referred as self-calibration because they do not require direct mass calibration data. Operationally, one parametrizes the mass observable relation and then uses a standard likelihood methods to jointly fit for both cosmology and the $P(X\ M, z)$ parameters.

One such statistical method uses the spatial clustering of the cluster themselves and the cluster number counts for self calibration. The clustering is characterized by the variance of counts in cells (Lima and Hu (2004)), the sample covariance (Lima and Hu (2005)) or by the cluster correlation function or power spectrum (e.g., Schuecker et al. (2003); Majumdar and Mohr (2004)).

Lima and Hu (2005) studied self calibration with cluster counts and sample covariance. They claim that the exponential sensitivity of number counts to the cluster mass requires a calibration of the whole observable mass distribution before cosmological information of dark energy can be extracted on high redshift. They describe the observable mass distribution and the effect of the scatter, σ_{lnM}, in the cluster counts which we discuss in detail in 3.3.

The other statistical method is the stacked weak lensing, that it is the cluster-shear correlation function, which can be inverted to yield the mean 3D mass profile in the bin (Johnston et al. (2007)). Apart from calibrating the mass observable relation it can also be used on large scales to measure and remove the halo bias and thereby provide a direct measurement of $\sigma_8\Omega_m^q$ beyond the cluster counting technique.

One can easily obtain high signal-to-noise measurements even for low mass clusters and large angular distances (Mandelbaumand et al. (2008);Sheldon et al. (2009)). The underlying halo population is randomly oriented relative to the line of sight and thus the stacking weak lensing does not suffer

from orientation biases. However, the possible selection biases involved in a given cluster selection algorithm need to be explored and they must be calibrated carefully on simulations.

Cluster mass profiles can be determinate, leading to a virial mass estimates independent of a model for the density profiles. In addition, in a cluster survey we can measure the cluster abundance, $n(M, z)$, binned by any observable proxy for mass (i.e., richness), and use this inversion method to calibrate the virial mass observable relation as a function of redshift. This allow cluster surveys to probe cosmology, including dark energy more precisely. Rozo et al. (2010) achieved same level of precision as X-ray samples with comparable levels of systematics errors.

Finally, because this method relies on stacking all galaxy clusters, it only provides information about the mean of the mass observable relation, so additional data are required to provide tight constraints on the scatter. To solve this problem, Rozo et al. (2009) derived an empirical constraint on the scatter of the richness mass relation for clusters in the maxBCG cluster catalog. Their measurement is achieved by demanding consistency between available weak lensing and X-ray measurements of the maxBCG clusters, and the X-ray luminosity mass relation measured in the 400d survey (Vikhlinin et al. (2009)). They found that the scatter in the mass at fixed richness was estimated to be $\sigma_{M|N} = 0.45^{+0.20}_{-0.18}(95\%CL)$ (see Figure 3.3).

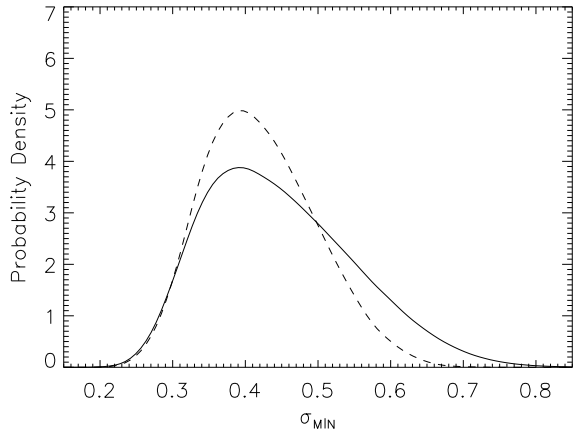

Figure 3.3: Marginalized likelihood distributions for $\sigma_{M|N}$. Solid lines are the results of the analysis of Rozo et al. (2009). The dashed curve is presented only to give a sense of how their results would improve with better understanding of the $L_X - M$ relation.

More recent work of Oguri and Takada (2011) also study the self calibration just with optical cluster surveys. Since, stacking weak lensing is the most promising route to meeting the stringent demands of next generation

cluster surveys, they combine number counts and cluster-cluster correlation function with stacked weak lensing measurement. They explore the potential of future optical cluster surveys, such as The Hyper Suprime-Cam (HSC) (Miyazaki et al. (2006), Takada (2010)), DES and Large Synoptic Survey Telescope (LSST) (LSST Science Collaboration et al. (2009)) for constraining cosmological parameters. Their results show how the combination of these observables can help self calibrate the mass observable relation (the mean mass and the scatter, see Figure 3.4) and the redshift uncertainty to obtain robust constraints on cosmological parameters without any priors on the nuisance parameters that model systematics uncertainties.

To summarize, large cluster surveys extending to $z \approx 1$ place much stronger constrains on the dark energy parameter as long as they are large enough to permit self-calibration of the mass observable relationship.

Now what it is important to say is that in this thesis we propose and test in simulations a new method to constrain the scatter for wide-field optical imaging survey using the bias of the cluster correlation function.

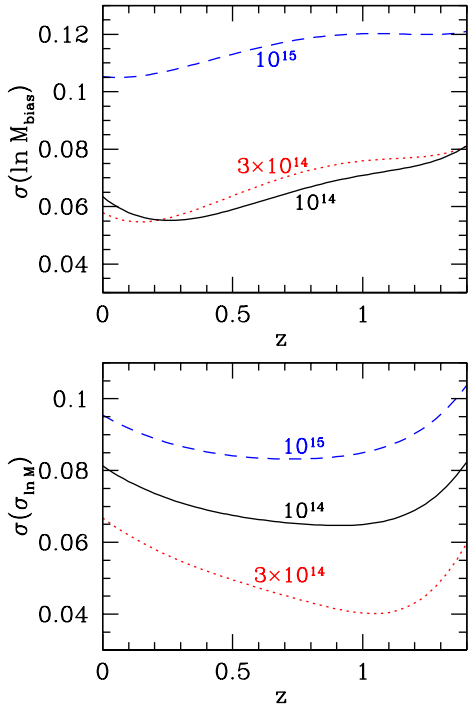

Figure 3.4: Self calibration of systematics (from Oguri and Takada (2011)). The parameters of the mass observable relation as a function of cluster redshift are constrained from the combination of all observables. The errors are shown for three different cluster masses.

3.3 The Scatter

As we mention before, the calibration task is to determine the mean relation and the scatter σ_{lnM} of the mass observable relation and to characterize any deviations from lognormal form that are large enough to affect the predicted abundance. Although is not our goal to study these deviations, later we will brie y discuss about them.

As in previous works which forecast constraints on cosmological parameters that can be achieved by cluster surveys (i.e., Ikebe et al. (2002), Lima and Hu (2005) and Oguri and Takada (2011)), we have assumed the scatter in the scaling relations to be lognormally distributed around the mean scaling relation, i.e., Gaussian or normal in lnM. Then the probability of observing the mass M_{obs} given the true underlying mass M is

$$P(M_{obs}\ M, z) = \frac{1}{\sqrt{2\pi\sigma^2_{lnM}}} exp[-x^2(M_{obs})] \tag{3.2}$$

with

$$x(M_{obs}) \equiv \frac{lnM_{obs} - lnM - lnM_{bias}}{\sqrt{2\sigma^2_{lnM}}} \tag{3.3}$$

As we will see in Chapter 8, we will use this distribution to create cluster catalogs and to predict the bias in clusters.

Lima and Hu (2005) describe how an unknown scatter, or, more generally, uncertainty in the distribution of the observable mass given the true mass causes ambiguities in the interpretation of number counts and degrades the cosmological constraints. For simplicity they allowed the mass variance σ^2_{lnM} and the mass bias lnM^{bias} to vary with redshift but not with mass.

Figure 3.5 shows the expected mass distributions of clusters above an observable threshold given a constant scatter $\sigma_{lnM} = 0.25$. The steepness of the mass function around the threshold in the observable mass determine the excess due to uppscatter versus downscatter. As the observable threshold reaches the exponential tail of the intrinsic distribution the excess of upscattered can become a significant fraction of the total. Given the relative effect of the scatter depends on the slope of the mass function, measuring the counts as a function of M^{obs} monitors the scatter in the mass observable relation. As we will see in Chapter 8 we will apply this same effect to calibrate the scatter using the average bias of the cluster correlation function.

Moreover, it is important to understand how the steepness changes with redshift and mass (see Figure 3.6). The impact of the scatter on the observed mass function is significantly greater at high mass and redshift. In other words, uncertainties in scatter can dominate those of bias for the steep mass function at high mass and redshift.

They also prospect the self calibration with cluster count and sample variance and asses the impact of the parameterization of the mass observ-

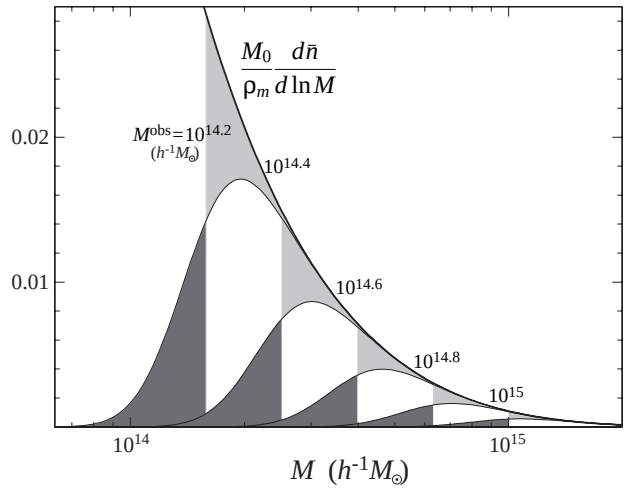

Figure 3.5: Expected mass distribution of above a certain M^{obs} given a scatter of $\sigma_{lnM} = 0.25$ (curves). The scatter changes the mass distribution to provide an excess of clusters scattering up (dark shaded) versus down (light shaded) across the threshold. The intrinsic mass function (thick line) has been normalized to $M_0 = 10^{14}h^{-1}M\odot$ and evaluated at $z = 0$ (Lima and Hu (2005)).

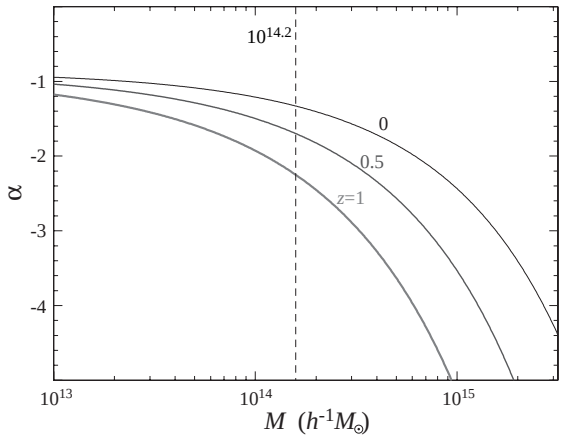

Figure 3.6: Local power law index α of the mass function as a function mass $\frac{dn}{dM}$ M^α for z=0, 0.5 and 1. The relative importance of the scatter compared with bias can be scaled through α (Lima and Hu (2005))

able relation on the dark energy. Figure 3.7 shows how uncertainties in mass bias and scatter cause degeneracies with dark energy. With only threshold binning, joint changes to the cosmology, mass bias, and scatter are degenerate with the dark energy equation of state w.

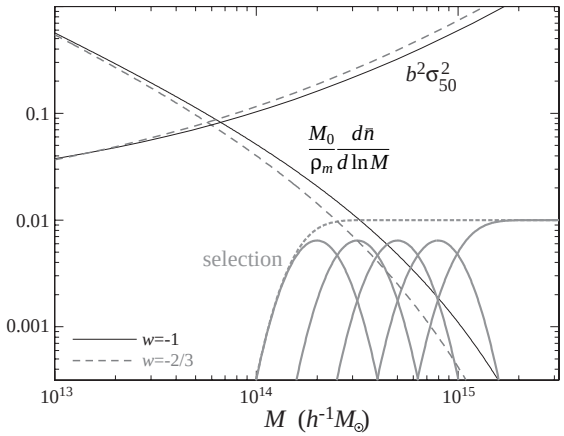

Figure 3.7: Simulations predictions of the sample variance of counts for a typical volume ($R = 50h^{-1}Mpc$) and the shape of the mass function as a function of mass (Lima and Hu (2005)). Self-calibration is assisted by binning the selection into 5 bins of $\Delta log_{10} = 0.2$ (solid lines) as opposed to a single threshold binning of $M^{obs} \geq 10^{14.2}h^{-1}M_\odot$(dotted lines). With only threshold binning, joint changes to cosmology, mass bias, and scatter are degenerate with the dark energy equation of state w (long dashed lines).

Oguri and Takada (2011) found that combining cluster observables with stacked weak lensing allows the mass and redshift dependence of the mean and mass variance to be parametrized in an extremely exible way while retaining enough information to yield strong cosmological constrains. Figure 3.4 shows the self calibration of systematics for the HSC. It show the marginalized 68% error on the parameters in the mass observable relation as a function of cluster mass and redshift. The mass calibration of more massive clusters are less accurate, simply because of the smaller number of clusters available for the stacked lensing analysis. They found that the scatter is constraint to $\sigma(\sigma_{lnM}) \sim 0.07$ for a wide range of redshift at $M = 10^{14}h^{-1}M_\odot$, indicating that the scatter is determined at 7% precision. The best result they found is that scatter is constrained to $\sigma(\sigma_{lnM}) \sim 0.04$ (4% precision) for $M = 3 \times 10^{14}h^{-1}M_\odot$ at $z \sim 1.1$.

As we mention before, there is the possibility that the core of $P(M_{obs}\ M, z)$ deviates from log-normal form. This problem was considered by Shawn et al. (2008) for wide are surveys, in particular for Sunyaev Zeldovich (SZ) (see section 3.4.3) and optical surveys such as SPT and DES. They parametrize the non-Gaussian scatter by incorporating the third and fourth moments

(skewness γ and kurtosis κ) into the distribution of $P(M_{obs}\ M, z)$.

They demonstrate that for low scatter mass proxies like SZ ux, higher order moments do not significantly affect the observed cluster mass and redshift distributions. However, the impact of the γ is more evident for higher scatter mass indicators such as optical richness. They found that for high scatter masses, the limiting mass threshold must be less than $10^{14}h^{-1}M_{\odot}$, to ensure that the skewness does not significantly effect dN/dz, especially at high redshift. An unknown level of non-Gaussian scatter is roughly equivalent to an additional uncertainty on the variance σ^2_{lnM} and thus may limit the constraints that can be place on the dark energy equation of state w.

This discussion demonstrates the value of finding improved optical richness estimators that have lower scatter relative to mass.

Numerical simulations predict distributions of X-ray observables that are close to lognormal (see Stanek et al. (2010)). We therefore do not expect X-ray studies to be sensitive to departures from a lognormal.

Rykoff et al. (2012) describe redMaPPer, a new red sequence photometric cluster finder algorithm that can deliver the necessary cluster samples to exploit near future photometric surveys such as the DES. Their goal is to develop improved richness estimators and reduce the scatter. In Rozo et al. (2014) is presented a comparison of the SDSS DR8 redMaPPer with SZ Planck 2013 cluster catalog with high quality mass proxy. They show that the redMaPPer richness λ is a low scatter mass proxy with high completeness and low impurity. Their results highlight the power of multi-wavelength observations to identify and characterize systematics errors in galaxy clusters such the scatter. While this work has focused on the application of redMaPPer to the SDSS DR8 catalog, we emphasize that this algorithm was developed specifically for upcoming large photometric surveys such as DES and LSST.

In next chapter, in particular at Section 4.3 we will address the problem of the scatter within the context of a DES-like cluster cosmology experiment and study how precisely must the scatter be known for cosmological analysis.

3.4 Observational Considerations

Here we outline how clusters are observed in all three of these wavebands and how these observations reveal a cluster total mass. We will discuss techniques to measure the masses of clusters and observable proxies that correlate tightly with mass.

A few major cluster detection methods have been used since Abell's time. Clusters contain a lot of hot gas, which radiates X-rays in a process known as Bremsstrahlung radiation; clusters can therefore be found thanks to their X-ray luminosity. A more exotic method uses the fact that cosmic microwave background radiation photons will be bumped to higher energies by interacting with the hot cluster gas (the Sunyaev Zeldovich effect).

Since DES is an optical survey, we will emphasize in the optical observations and the red sequence method.

3.4.1 Optical Observations

Optical identification of galaxy clusters has been going on for quite a long time. George Abell (Abell (1958)) compiled a catalog of clusters in which they identified regions in the sky that show an overdensity of galaxies. An extension of the catalog to southern sky was published in 1989 (Abell et al. (1989)). Abell's catalogs contain most of the known nearby galaxy clusters and are the foundation for much of our modern understanding of clusters, in particular if these catalogs are to be used for statistical purposes.

The selection of galaxy clusters from an overdensity of galaxies on the sphere is not without problems. The survey should be as complete (all objects which fulfill the selection criteria are contained in the catalog) and pure (it should not contain any objects that do not belong in the catalog because they do not fulfill the criteria) as possible.

The main drawback for optical cluster detection is projections effects. Because of them completeness and purity cannot be expected. Random overdensities on the sphere caused by line of sight projection may easily classified as clusters. The reverse effect is likewise possible: due to uctuations in the number density of foreground galaxies, a cluster at high redshift may be classified as an insignificant uctuation and thus remain undiscovered (Schneider (2006)).

Because the cores of galaxy clusters are dominated by red, early-types galaxies, an effective way to reduce the impact of projection effects is to use color information to select for overdensities of red galaxies. Many cluster are significantly redder than other galaxies at a similar redshift, owing to their lack of ongoing star formation. The colors of their aging stellar populations therefore place these cluster members on a narrow and distinctive locus known as red sequence in a plot of galaxy colors versus magnitude,

the E/SO ridge line (e.g., Gladders and Yee (2005)). Figure 3.8 shows the red sequence that is in place in cluster Abell 1084. Multicolor photometry

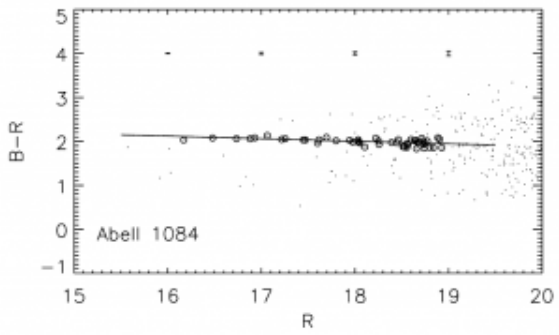

Figure 3.8: Here's an example of a red sequence, from the cluster Abell 1084. Each point describes the color and brightness of an individual galaxy in the cluster. A clear red sequence is present (the black line). The remarkable tightness of the correlation is a general feature of all clusters, which is why a method like this can work.

is needed to cover a broad range of redshift and to track the intrinsic 4000 angstrom break feature of old stellar populations.

While the projection effect systematics has been drastically suppressed in modern surveys with multi-band photometry and photometric redshift estimators, one still expects $5\% - 20\%$ of photometrically selected clusters to suffer from serious projection effects (Cohn et al. (2007); Rozo et al. (2011)).

The importance of projections effects increases with decreasing mass, so we expect it is projection effects will ultimately set the detection mass threshold for optical cluster finding in surveys (Weinberg. et al. (2013)).

3.4.1.1 Optical Mass Measurements

Optical observations offer two complementary ways to measure the cluster mass, through the orbital velocities of the member galaxies and thought the degree that to which galaxies lying behind the cluster are lensed by the cluster's gravitational potential (a review of the gravitational lensing can be found in Bartelmann and Schneider (2001)). As we discussed before, the weak lensing method is a very promising method for measure cluster masses that it is independent of the dynamical state, the cluster's baryon content, and mass-light ratio. The stacked weak lensing analysis have proved successful in calibrating the mass observable scaling relation down to relative masses.

3.4.1.2 Optical Richness and Weak Lensing Masses. The Mass richness Relation

Weak lensing masses are expected to correlate well with cluster richness. In this thesis we will use the form of the mean relation between cluster mass and richness used in Rozo et al. (2009). It is based on the results from the statistical weak lensing analysis in the maxBCG cluster catalog (Koester et al. (2007)). We will described this catalog and the mass observable relation after a few more words about the main observables for optical surveys, the richness, luminosity and colors.

Abell's catalog placed the clusters in categories of richness corresponding to the net excess of galaxies brighter than the magnitude limit used to define each cluster. Thus, richness is define as the number of galaxies within a detection aperture.

Invoking assumptions about the shape of the luminosity distribution helps to link richness more directly to a cluster's total luminosity. Cluster galaxies generally adhere to a luminosity distribution function following the form proposed by Schechter (1976), with the number of galaxies in luminosity range dL about L proportional to $L^{-\alpha}exp(-L/L_*)$, with $\alpha \approx 1$. L_* is a characteristic luminosity above which the distribution decrease exponential.
.

The Sloan Digital Sky Survey (SDSS) uses a dedicated 2.5-m wide-angle optical telescope, and takes images using photometric system of five filters (named u, g, r, i and z). The maxBCG catalog is a selected volume limited catalog of 13,823 clusters over the redshift range $z \quad [0.1, 0.3]$. The clusters were identified using and algorithm that identifies clusters as overdensities of red sequence galaxies. It exploits two well-known features of rich galaxy clusters. First, the bright end of the cluster luminosity function is dominated by galaxies occupying a narrow region of color-magnitude space (the E/S0 ridgeline). Second, clusters contain a brightest cluster galaxy (BCG) that is located near the center of the galaxy distribution. maxBCG uses a maximum likelihood method to evaluate the probability that a given galaxy is a BCG (brightest cluster galaxy) near the center of a red-sequence galaxy density excess.

The maxBCG is divided in nine richness bins spanning the range N_{200} ϵ $[11, 120]$. The richness measurement is defined as the number of red sequence galaxies brighter than $4L_*$ (in the i-band) within a scaled radius R_{200}. R_{200} is the radius within which the density of galaxies with $-24 < M_r < -16$ is 200 times the mean density of such galaxies (Hansen et al. (2005)).

The separate statistical weak lensing measurement of Johnston et al. (2007) and Mandelbaumand et al. (2008)) indicate that N_{200} is strongly correlated withy cluster virial mass. These separated weak lensing analysis are discussed in the Appendix of Rozo et al. (2009) and yield a mean relation

between cluster mass and richness given by

$$\frac{M \quad N_{200}}{10^{14}} = e^{B_{M|N_{200}}} \left(\frac{N}{40}\right)^{\alpha_{M|N_{200}}} (3.4)$$

3.4.2 X-ray Observation

X-rays are considered the cleanest method for selecting galaxy clusters. The primary advantages of X-ray are their completeness and purity and the tight correlation between X-ray observables and mass. However, the main di - culty for X-ray selection is a technological one, specially, the need for space-based observatories which makes their construction relative expensive.

X-rays searches are nearly free from projections effects.. The X-ray emission is scales as density squared, which enhances the relative contrast of a cluster in the sky and renders projections effects improbable. The X-ray temperature and the X-ray luminosity (i.e., Stanek et al. (2006)) are good indicators for the mass of the cluster. The X-ray temperature provides a very precise measure for their virial mass, better than the velocity dispersion. Although the temperature is the preferred measure for the cluster's mass, one will in many cases resort to the relation between mass and luminosity because determining the luminosity (in a fixed energy range) is considerable simpler than measuring the temperature, for which significantly longer exposure times are required (Schneider (2006)). .

3.4.3 Sunyaev Zeldovich Observation

The Sunyaev Zeldovich (SZ) effect was predicted in 1970. The Compton scattering leads to a reduced number of photons at lower energies, relative to the Planck spectrum. The energy of photons changes slightly through the scattering by the hot electrons, in a way that they have an average higher frequency after scattering. The cosmic microwave background (CMB) spectrum, measured in the direction of a galaxy clusters, deviates from a Planck spectrum; the degree of this deviations depends on the temperature of the cluster gas and on his density (Schneider (2006)).

While detection of SZ effect in know galaxy clusters date back as early as 1976, it is only recently that instrumentation advances have made large scale SZ searches feasible. The first large catalogs are currently under construction, using the South Pole Telescope (SPT), the Atacama Cosmology Telescope (ACT), and the Planck satellite (Tauber et al. (2010)).

SZ surveys are well suite, in principle, to searches for massive clusters at high redshift. Challenges to these projects include determining the optimal observables (i.e., the best mass proxies) to measure from the survey data in the low signal-to-noise ratio regime; calibration the mass scaling of these observables and understanding in detail the impact contamination by

radio and infrared sources. Projections effects are also expected to be more significant for SZ surveys than for X-rays (Allen et al. (2011)).

Chapter 4

The Dark Energy Survey Project

Abstract: In this chapter we introduce the Dark Energy Survey [1] and the instrument, the DECam camera where I was involved in the CCD R&D program. We summarize the four proposed techniques for probing dark energy, focusing on galaxy clusters and their systematics effects. As our goal is to measure the scatter of the mass richness relation, finally we will delve more into its study under the project DES.

4.1 Overview

Figure 4.1: Blanco Telescope

[1] http://www.darkenergysurvey.org

The Dark Energy Survey collaboration (The Dark Energy Survey Collaboration (2005)) was established with the objective of developing a new instrument for the Blanco 4 meter telescope at Cerro Tololo Inter-American Observatory (CTIO) (see Figure 4.1) in partnership with the National Optical Astronomy observatory (NOAO). The collaboration has been growing since 2005 and now consist of approximately 120 scientist located at 4 US national laboratories, 7 US universities, NOAO/CTIO, and consortia from United Kigdom, Spain, Brazil, Germany and Swizerland.

The survey data will allow us to measure the dark energy, the dark matter densities and the dark equation of state through four independent methods: galaxy clusters, weak gravitational lensing tomography, galaxy angular clustering and supernova distances. These methods constrain different combinations of cosmological model parameters and are subjects to different systematic errors. By deriving the four sets of measurements from the same data set, the dark energy survey will obtain important cross checks from the systematics errors and thereby make a substantial and robust advance in the precision of dark energy measurements. DES will allow to measure the dark energy equation of state w with a statistical precision of order $\delta w \leq 5\%$.

The DES comprises an optical to near infrared survey over 5000 deg^2 of the South Galactic Cap to $\sim 24th$ magnitude in the SDSS grizY bands and a time-domain griz survey over 30 deg^2 with a cadence of approximately six days. These interleaved surveys are carried out over 525 nights in the course of five years using the 570-megapixel imager DECam (Flaugher et al. (2012), Diehl and Dark Energy Survey Collaboration (2012)) mounted at the prime focus of the Blanco Telescope. DECam was commissioned in September and October of 2012, followed by an extended testing and survey commissioning period know as DES Science Verification (SV, November 2012-February 2013). Figure 4.2 shows a photo of DECam mounted at the prime focus of the Blanco telescope. The first observing season of the Dark Energy Survey (Y1) (Diehl and et al. (2014)) started on August 2013 and conclude on February 2014 . The 5000 deg^2 DES observing field wide-field (WF) will be accomplished in 10 dither patterns (tilings). Ten 3 deg^2 fields will be imaged repeatedly to produce supernova survey.

The WF has three main regions (see Figure 4.3). A broad roughly circular region (approximately, $RA = [0, 120]$ degrees and $DEC = [-70, -10]$ degrees) that provides a large contiguous area for the large scale structure (LSS) measurements. There is also a wide box-shaped region around SPT observing area (Ruhl et al. (2004)). Finally, the survey encompasses a part of SDSS Stripe 82, primarily for calibration purposes (Annis et al. (2011)). The major components of DECam are a 570 megapixel optical CCD camera (see Figure 4.4), a wide-field optical corrector (2.2 deg. field of view), a 5-band filter system with SDSS g,r, i, z and Y filters, guide and focus sensors mounted on a focal plane, low noise CCD read out, a cryogenic cooling sys-

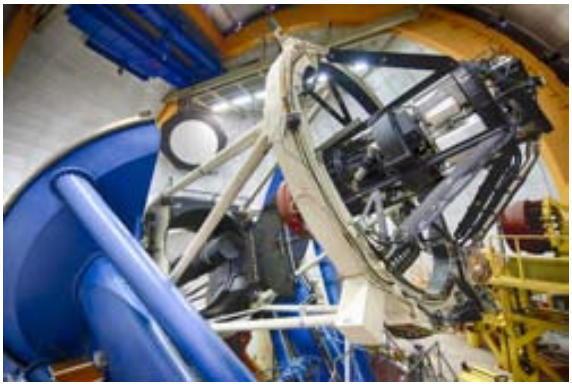

Figure 4.2: The Dark Energy Camera, mounted on the Blanco telescope at the Cerro Tololo Inter-American Observatory in Chile. Credit: Reidar Hahn/Fermilab.

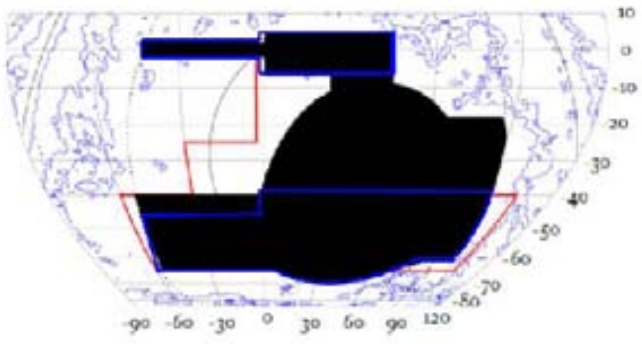

Figure 4.3: The Dark Energy Survey observing wide fields are shown in black on this plot of RA and DEC. During Y1 DES planned to observe the areas outlined in blue, which encompass SDSS Stripe 82 (upper) and SPT area (lower). The red line is an artifact, showing a previous version of the survey field.

tem to maintain the focal plane at 180 K, as well as a data acquisition and instrument control system to connect to the Blanco observatory infrastructure. The imager and corrector barrels are supported as a single unit by a

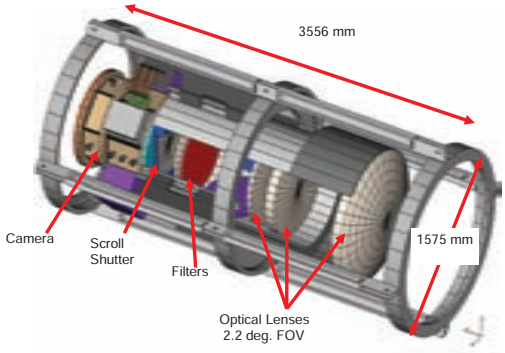

Figure 4.4: DECam design

6×6 hexapod that provides lateral adjustability as well as focus control.

The optical corrector consists of five fused silica lensed that produce an unvignetted 2^o diameter image area. The heart of DECam, the camera focal plane, consists of 62 $2k \times 4k$ CCDs $(0.27''/pixel)$ arranged in a hexagon covering an imaging area of 3 deg^2. Each device of the camera with $2k \times 4k$ format have 15 $\mu m \times 15$ μm pixels and is fitted with two readout amplifier. Smaller format CCDs for guiding and focusing will be located at the edges of the focal plane. These detectors will be the same type of CCDs but in a $2k \times 2k$ format.

To e ciently obtain z-band images ($\sim 1000nm$) at high-redshift ($z \sim 1$) galaxies, we have selected the fully depleted, high-resistivity, 250 μm thick silicon devices that were designed and developed at the Lawrence Berkeley National Laboratory (LBLN) (Holland et al. (2003)). The thickness of the LBLN design has two important implications for DES: fringing is eliminated, and the QE of these devices is $> 50\%$ in the z band, a factor of ~ 10 higher than traditional thinned astronomical devices (see Figure 4.6)

The bare silicon die were delivered to Fermilab and then assembled and tested in the Fermilab CCD facility where we take an active part (see Estrada

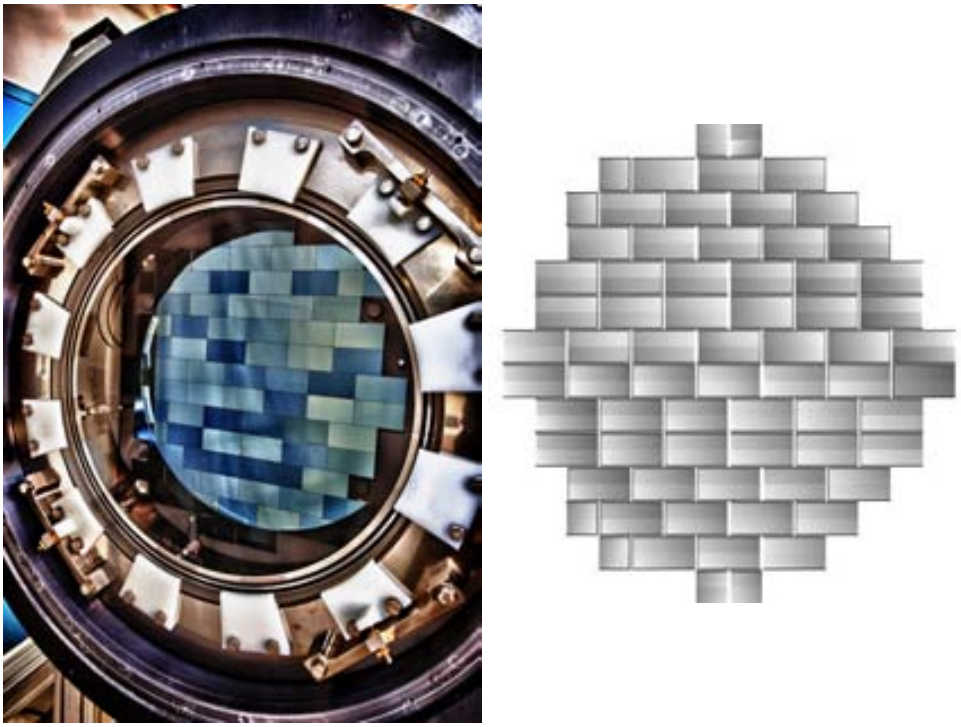

Figure 4.5: Left:The Dark Energy Camera features 62 charge-coupled devices (CCDs), which record a total of 570 megapixels per snapshot. Credit: Reidar Hahn/Fermilab. Right: A at-field obtained after shipping with the imager in the Coude room of the Blanco Dome.

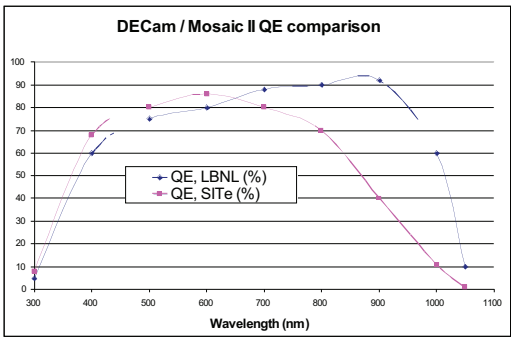

Figure 4.6: Quantum e ciency of the LBNL CCDs compared to those in the Mosaic II Camera previously used at prime focus on the V. M. Blanco 4-m telescope.

et al. (2006), Diehl et al. (2008) and Estrada et al. (2010)).

The DECam project introduced a number of new approaches to the construction of a major instrument for a ground based telescope. The major risks to the project cost and schedule were the CCDs, the front end electronics (FEE) and the large optics. I was involved in the CCDs R&D program efforts, particularly in the initial phase (Campa (2007), Estrada et al. (2006)). In the Appendix A we will describe the techniques and methods in which I was involved. We present the results of testing and characterization for these devices and compare the results with the technical requirements for the Dark Energy Survey.

4.2 Dark Energy Survey Techniques

In Chapter 3 we have discussed in detail the galaxy clusters as a cosmological probes. Here, we brie y summarize the four proposed probes that DES will use for probing dark energy. We provide additional details and context for the DES project. In next section we will emphasized in galaxy clusters.

- Galaxy Clusters

  The primary design driver of the DES is the detailed optical measurement of galaxy clusters, including photometric redshift, in conjuntion with the SPT Survey. The DES is designed to measure e ciently and accurately photometric redshifts for all SPT clusters to $z = 1.3$.

  As we discussed in previous chapter, the cluster counting method depends critically on accurate statistically cluster mass estimates and on well characterized completeness of the cluster samples as a function of redshift. The SZ effect ux is strongly and robustly correlated with cluster mass. The DES will statistically calibrate SZ effect cluster mass estimates using the cluster-mass correlation function inferred from weak lensing (Johnston et al. (2007)). In addition to measuring the photometric redshift of SPT clusters, the DES will detect clusters optically to lower mass thresholds than the SPT using the red galaxy color-magnitude sequence (Gladders and Yee (2005)). This will provide a cross-check on the completeness of the SPT cluster selection function as well as an important independently selected cluster sample in its own right.

- Weak lensing tomography

  The DES will measure the weak lensing (WL) shear of galaxies as a function of photometric redshift. The evolution of the statistical pattern of WL distortions and the cross-correlation between foreground galaxies and background galaxy shear, are sensitive to the cosmic expansion history through both geometry and the growth rate of structure (Hu and Jain (2004)).

- Galaxy angular clustering

  The DES will measure the angular clustering of galaxies in photometric shells out to $z \sim 1.1$. The matter power spectrum as a function of wavelength shows characteristics features (see details in Section 5.3), a broad peak as well as baryon wiggles arising from the same acoustic oscillations that give rise to the Doppler peaks in the CMB power spectrum. In combination with CMB observations, they serve as a standard rules for distance measurements, providing a geometric test of cosmological parameters.

- Supernova luminosity distances

  In addition of the wide-area, the DES will use %10 of its allocated time to discover and measure well-sample riz light curves for 1900 Type Ia supernovae in the redshift range $0.3 < z < 0.75$ through repeat imaging of a 30 deg^2 region. These SNe will provide relative distance estimates to constrain the properties of dark energy. Abbott et al. (2012) report the discovery of the first set of supernovae (SN) from the project .

  Figure 4.7 shows a composite 3-color image of one of the DES SN fields. It is the field-of-view of one exposure.

Figure 4.7: Composite Dark Energy Camera image of one of the sky regions that the collaboration will use to study supernovae, exploding stars that will help uncover the nature of dark energy. The outlines of each of the 62 charge-coupled devices can be seen. This picture spans 2 degrees across on the sky and contains 520 megapixels.

4.3 Clusters in DES

With the new instrument, DES will go beyond the reach of the SDSS by virtue of telescope aperture, median seeing, and CCD sensitivity particulary towards the infrared part of the spectrum. Consequently, the galaxy redshift distribution is expected to have a median $z \sim 0\,8$ and a significant tail beyond $z = 1$, which enables DES to detect clusters at high redshift ($z \sim 1$) and to use source galaxies for rigorous lensing analysis of clusters beyond $z \sim 0\,5$ (Melchior et al. (2014)).

Figure 4.8: Composite DECam image (combining images from 5 filters) of the cluster of galaxies SPT-CL J2332-5358. The center of the cluster is indicated by the yellowish galaxies in the middle of the picture. The bright galaxy in the upper left is in the foreground (closer to us than the cluster).

A key strength of DES is the ability to apply multiple techniques for both identifying clusters and inferring their masses, each with their own systematics. The SPT+DES cluster survey can achieve high statistical precision in constraining dark energy (see Figure 4.8 that shows a composite DECam image of the cluster of galaxies SPT-CL J2332-5358.). To approach that we need to understand the sources and the levels of systematics errors and develop methods to control them. Here we present an inventory of the systematics errors although we emphasize on the scatter in the mass observable relation. SZ effect method has a clean mass observable relation. However, work remains to be done in quantifying systematics in the optical mass observable scaling relations.

4.3.1 Systematics E ects

- Theory

  As we will see bellow, given the underlying cosmology and a spectrum of the initial uctuations, the evolution of the massive peaks in the density field can be calculated analytically or numerically. Predictions of the abundance and clustering of massive halos are becoming increasingly accurate. Therefore the main systematic concern for cluster cosmology is determining the mass-observable relations and, to a lesser extent, the observable selection functions.

- Selection Function

  The cluster sample must be both complete (above some threshold) and free of contamination, i.e., the cluster selection function must be well understood (The Dark Energy Survey Collaboration (2005)).

- Scaling relations: **The richness mass relation and the scatter for DES.**

  We need to measure the mass scaling relations and scatter. As we mention in Section 3.3, theoretically the scatter is a source of uncertainty in the predicted number of clusters.

  Rozo et al. (2011) define quantitatively when a source of scatter is observationally relevant. They measure how precisely must the scatter be know in a cluster counting experiment. They addres this problem within the context of a DES-like cluster cosmology experiment and adopt a lognormal model for $M_{obs} - M_{true}$ relation.

  Using Fisher matrix technique (Wu et al. (2008)), they estimate what the cosmological constraints derived from our fiducial cluster sample would like, assuming that the data is analyzed using the standard self calibration technique. Given any combination of σ_{true} and σ_{model}, they estimate the ratio $\frac{\Delta p}{\sigma(p)}$, where Δp is the offset $p_{obs} - p_{true}$ between the recovered value of the cosmological parameter p and its true value and $\sigma(p)$ the statistical uncertainty. Thus, they determine whether the difference between σ_{true} and σ_{model} is observationally relevant or not. Figure 4.9 shows contours of the ratio $\frac{\Delta p}{\sigma(p)}$ in the inference of dark energy parameters w_0 and w_a due to errors in the scatter. The y-axis σ_{model} indicates the scatter value we use in the analysis, while the x-axis σ_{true}, indicates the underlying true scatter. As can be seen, if $\sigma_{true} - \sigma_{model} \geq 0.05$, the recovered dark energy parameters will be significantly biased.

  DES employs a very similar richness estimator to the one that Rykoff et al. (2012) uses. In this paper they tested and optimized the richness measured proposed by Rozo et al. (2009) with maxBCG clusters in the

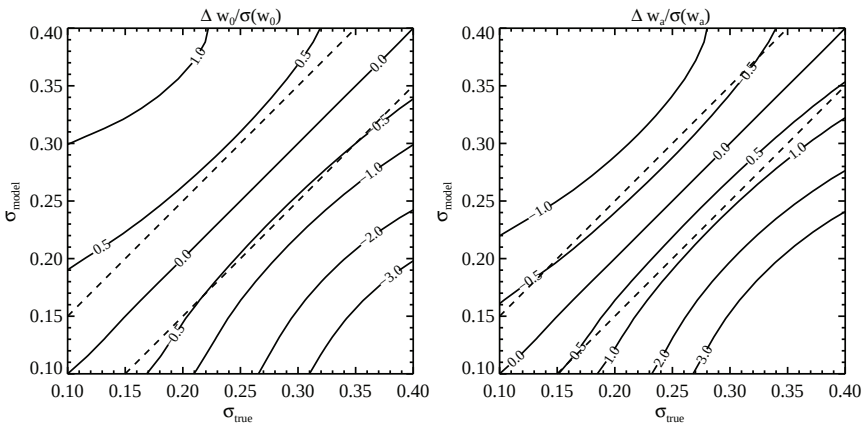

Figure 4.9: Systematics errors in the inference of dark energy parameters w_0 and w_a due to errors in modeling the scatter. Contours and numbers show the systematic errors Δw_0 (Δw_a) compared with statistical errors $\sigma(w_0)$ ($\sigma(w_a)$) (Rozo et al. (2011))

range $0.1 \leq z \leq 0.3$. Although the calibration of the mass observable relation is beyond the scope of this paper, they provide a rough calibration of the mass richness relation that may be used for comparison purposes as we will see below. They also give an estimation of the scatter which we will use as the expected value for the DES survey. They find that the total uncertainty in the mass of any given cluster is ≈ 0.33 at the 1σ level.

Here we also show the early results related to the mass observable relation from the DES science verification data given by Melchior et al. (2014). They measure the weak lensing masses and galaxy distributions of four massive clusters observed during the Science Verification phase of the survey. By fitting the NFW profiles to the clusters, they determine weak lensing mass that are in agreement with previous work. For Abell 3261, they provide the first estimates of redshift, weak lensing mass, and richness. In addition, the cluster-galaxy distribution showcase the potential of DECam and DES for detailed studied of degree scale features on the scale. They also perform a cross-check. Figure 4.10 shows their comparison of the DES data with the best fit solution from the mass richness relation for low redshift clusters provided by

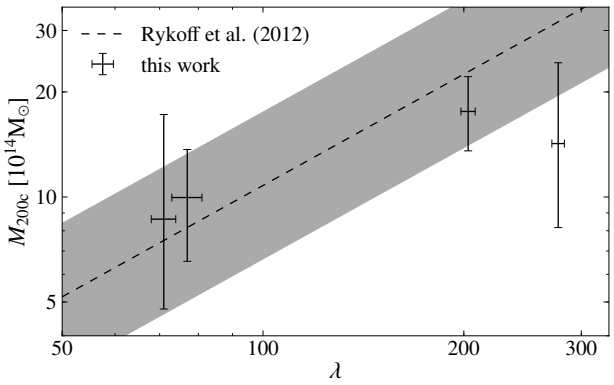

Figure 4.10: Lensing mass as a function of redMaPPer 's richness λ for the four clusters observed in the SV phase (Melchior et al. (2014)). The dashed line shows the expected scaling relation from Rykoff et al. (2012) with their proposed scatter at fixed richness (shaded region)

Rykoff et al. (2012). They also shows their proposed relative scatter of 33% at fixed richness mentioned before. They found that their measurements agree with the expectations, within the considerable scatter both measurements exhibit.

Chapter 5

Structure Formation and Statistical Description of Density Fluctuations

Abstract:

In this chapter we briefly summarize some of the results which are more relevant for describing structure formation quantitatively in the ΛCDM paradigm. This includes the analysis of the evolution of density perturbations over time to construct the linear power spectrum of matter, as well as the statistical description of density fluctuations that quantify the clustering of objects. This is intended to form the basis for subsequent chapters, where we will analyze the measurements of the dark matter halos and galaxy clusters distribution.

5.1 Introduction

The Universe is approximately homogeneous and isotropic on large scales (larger than 100 Mpc), but on smaller scales, we observe huge deviation from the mean density in the form of objects such as galaxies and clusters of galaxies. By structure formation we mean the generation and evolution of this inhomogeneity and how these objects are distributed, their clustering.

The current ΛCDM paradigm establish that the main ingredient for structure formation is a pressurless cold dark matter (CDM) composed of particles which decoupled from radiation at redshift when these particles where non-relativistic. The velocity dispersion of CDM is neglected and it is believed to dominate the other components of the Universe for its last period, until the cosmological constant becomes relevant. Such period is very important because is when it is created the potential wells that allow

the growth of density contrast of the baryons, the components of visible structures in our Universe.

Therefore, we will study the dark matter perturbations which in principle are coupled to other perturbations. However, in practice, perturbations to dark matter depends very little on the details of the radiation perturbations. Dark matter, by definition, is affected by radiation only indirectly, through the gravitational potentials (Dodelson (2003)).

5.2 Growth of Inhomogeneities

5.2.1 Introduction

First, we introduce the dimensionless density perturbation field or the relative density contrast $\delta(\bar{x}, t)$ to describe an inhomogeneous universe quantitatively

$$\delta(\bar{x}, t) \equiv \frac{\rho(\bar{x}, t) - \bar{\rho}(t)}{\bar{\rho}(t)} \tag{5.1}$$

where $\bar{\rho}(t)$ is the mean cosmic matter density in the Universe at time t.

The evolution of the inhomogeneities is directly observable and the Universe was less inhomogeneous at high redshift than it is today. The smallness of the CMB anisotropy suggest that at $z \sim 1000$ the density inhomogeneities must have very small amplitudes, $\delta << 1$. However, today these amplitudes are considerably larger; for example a massive cluster of galaxies contains within a radius of $\sim 1.5h^{-1}Mpc$ more than 200 times more mass than an average sphere of this radius in the Universe.

The model of gravitational instability describes the evolution of these inhomogeneities, and is most likely responsible for structure in the Universe. The seed of density inhomogeneities from quantum uctuations grows from the in uence of the gravitational forces; the pressure opposes this growth, so that the balance between pressure forces and gravitational force governs the temporal behavior of density contrast. This scenario is complicated by the fact that the Universe is expanding. The expanding rate inhibits the growth of perturbations and introduces a characteristic length scale, the Hubble scale .

Taking the expression of the density contrast given by Equation 5.1, the dynamics of the cosmic Hubble expansion is controlled by the gravitational field of the average matter density $\bar{\rho}(t)$, whereas the density uctuations $\rho(\bar{x}, t) - \bar{\rho}(t)$ generate an additional gravitational field (Schneider (2006)).

5.2.1.1 Three Stages of Evolution and the Power Spectrum

The evolution of cosmological perturbations breaks up naturally into three stages explained in Chapter 2. We want study how the different ambient

cosmological conditions (i.e matter or radiation domination eras) alter the growth rate and the solutions for different modes.

In order to use the correct theory of structure formation is essential to consider the scales of perturbations. We compare the perturbation scale with the comoving horizon $r_{H,com}(t)$

$$r_H, com = \int_0^t \frac{cdt}{a(t)} = \int_0^a \frac{da}{a} \frac{c}{aH(a)} \tag{5.2}$$

which is defined as the logarithmic integral of the comoving Hubble radius $1/aH$ or the total comoving distance that light travels. Perturbation at subhorizon scales, $L \sim \frac{2\pi}{k} < r_{H,com}$, can be treated with Newtonian perturbation theory (see Section 5.2.2), but scales which are close to horizon size or superhorizon, $L \sim \frac{2\pi}{k} \geq r_{H,com}$ require relativistic perturbation theory, which is based on General Relativity (see Section 5.2.3.1).

Figure 5.1 shows the gravitational potential as a function of scale factor for long, medium and short wavelength modes. Short scales enter the horizon first, large scales enter later.

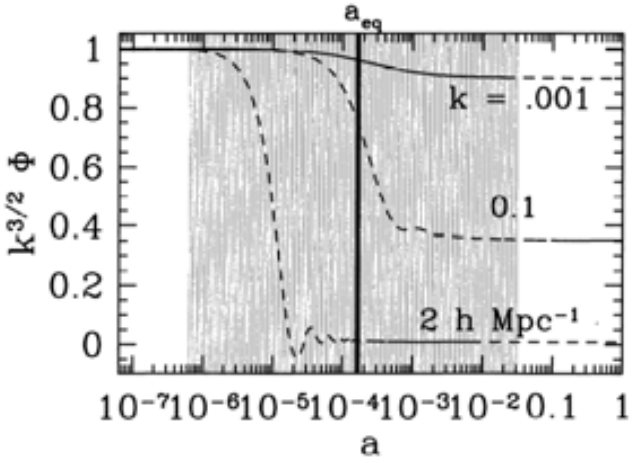

Figure 5.1: (From Dodelson (2003))The linear evolution of the gravitational potential ϕ. Dashed line denoted that the mode has entered the horizon. Evolution in the dashed region is described by the transfer function.

Early on, all the modes are outside the horizon and the potential is constant. At intermediate times two things happen: the Universe evolves from radiation domination to matter domination and the modes enter the

horizon. The large scale modes, which enter the horizon well after a_{eq}, evolve much differently than the small scale modes, which enter the horizon before equality. The potential is greatly affected at scales that enter the horizon during transitions and such scales are special because they characterize the present structure of the universe (see Section 5.3). Finally, at late times, all the modes evolves identically (Dodelson (2003)).

We are able to observe the distribution of matter at late epochs, in the third stage. If we wish to relate the potential during these times to the primordial potential setup during in ation, $\phi_p(\bar{k}, a)$, we write schematically

$$\phi(\bar{k}, t) = \phi_p \times \ TransferFunction(k) \ \times \ GrowthFunction(t) \qquad (5.3)$$

where we have roughly defined the transfer function and the growth factor. The transfer function describes the evolution of perturbations through the epoch of horizon crossing and radiation/matter transition (shaded region in Figure 5.1), while the growth function describes the wavelength independent growth at late times.

The potential uctuations, ϕ and the density perturbations, δ are related by the Poisson's Equation 5.10 that we describe later.

Therefore, the easiest way to probe the potential is to measure the matter distribution. The Fourier components δ_k evolve independently following the effects of the gravitational potential described before.

Since the linear power spectrum of the matter distribution is just the power spectrum of the linear density perturbation field δ (see Equation 5.27), we can express the linear power spectrum of the matter distribution in terms of the primordial power spectrum, the transfer function, $T(k)$ (see section 5.2.3.1, and the growth function, $D(t)$ normalized to get $D(z = 0) = 1$ (see Section 5.2.2.2).

$$P_{lin}(k, t) = Ak^{n_s}T^2(k)D^2(t) \qquad (5.4)$$

Thus, we can find the time dependent linear power spectrum of the matter perturbations as a results of the evolution of the initial spectrum k^{n_s} by a variety of processes. The spectral index, n_s, rules the behavior of this primordial power spectrum. If $n_s = 1$ this spectrum is scale invariant and is called Harrison-Zeldovich spectrum (Harrison (1970), Zeldovich (1972) and Peebles and Yu (1970)).

5.2.2 Results from Newtonian Hydrodynamics in an Expanding Universe.

We summarize some of the most important concepts and results from the evolution of the perturbations at subhorizon scales using the Newtonian perturbation theory. In addition, we assume for simplicity that the matter in the Universe consist only in dust that is described by the uid approximation.

We suppose that the universe is filled with an inhomogeneous, pressureless di, ideal and non relativistic uid that is governed by the basic hydrodynamical equations of Newtonian physics. The continuity and Euler equation are given by

$$\frac{\partial \rho}{\partial t} + \quad \cdot (\rho \bar{u}) = 0 \tag{5.5}$$

$$\frac{\partial \bar{u}}{\partial t} + (\bar{u} \cdot \quad)\bar{u} + \frac{1}{\rho} \quad p + \quad \tilde{\phi} = 0 \tag{5.6}$$

where ρ is the mass density, p is the pressure and $\bar{u}$ the velocity field. The Newtonian gravitational potential $\tilde{\phi}$, satisfies the Poisson equation

$$^2\tilde{\phi} = 4\pi G\rho \tag{5.7}$$

Moreover, our simple ideal uid does not account for diffusion process which erase small scale perturbations.

These equations have to be complemented by the equation of state $p = p(\rho)$ and the equation of the conservation of entropy. Assuming adiabatic perturbations ($\delta S = 0$, where S is the entropy), the equation of state which links the pressure and the density is usually given in the form of adiabatic speed of sound

$$c_s^2 = \left(\frac{\partial p}{\partial \rho}\right) \tag{5.8}$$

The hydrodynamical equations are nonlinear and its very di cult to find their general solution. We will solve them at first order (or linear regime) where $\delta << 1$ and the perturbed quantities are small compared to their background.

The gravitational potential $\tilde{\phi}$ is written as,

$$\tilde{\phi} = \phi_0 + \phi \tag{5.9}$$

where ϕ_0 is the Newtonian potential for a homogeneous density field, and ϕ is the perturbation of the gravitational potential ϕ that satisfies the Poisson equation

$$^2\phi = 4\pi G\bar{\rho}\delta \tag{5.10}$$

We write the governing equations in comoving coordinates and we use the density contrast δ instead of the density.

Then, the continuity and the Euler equations are combined to form a single second-order differential equation. If we consider plane wave solutions and we write these equations in Fourier space we obtain (see Peebles (1980), Peacock (1999) and Schneider (2006)).

$$\ddot{\delta_k} + 2H\dot{\delta_k} + \left[\frac{c_s^2 k^2}{a^2} - 4\pi G\bar{\rho}\right]\delta_k = 0 \tag{5.11}$$

This is sometimes called the Jeans equation (although Jeans considered a static, not an expanding uid) and is the one that governs the gravitational amplification of density perturbations. The term $2H\dot{\delta_k}$, occasionally referred as Hubble Drag , will serve to slow the growth of perturbations compared to the exponential form of a non-expanding universe.

The nature of the solution of Equation 5.11 depends on the sign of the factor in the brackets. The basic forces act in opposite directions. The first term in brackets is due to pressure gradients and the second term is due to gravity. Pressure tries to resist compression, so if this term dominates, we have oscillatory solutions, standing sound waves that are damped by the $2H\dot{\delta_k}$ term. Thus, the amplitude of oscillations decreases with time as a damped oscillator. However if the gravity dominates, the perturbations grow.

There is a critical proper wavelength, know as Jeans length which is the scale of uctuation where pressure support equals gravitational collapse.

$$\lambda_J = c_s\sqrt{\frac{\pi}{G\bar{\rho}}} \tag{5.12}$$

At this scale we switch from the possibility of exponential growth for long-wavelenghts modes to standing sound waves at short wavelenghts. However, owing to the expansion, λ_J will change with time, and a given perturbation may switch between periods of growth and stasis. These effect help to govern the form of the perturbation spectrum (Peacock (1999)).

5.2.2.1 Cold Dark Matter Perturbations and Meszaros E ect

Cold Dark matter is believed to be the dominant component in the Universe. Therefore, we get a reasonable approximation for the behavior of the CDM perturbations by ignoring the baryon component ($\rho \approx \rho_{cdm}$).

Since the CDM is pressureless ($c_s = 0$), all scales are larger than the Jeans length and perturbations grow at all scales. We will get the Equation 5.11 for this particular case

$$\ddot{\delta_k} + 2H\dot{\delta_k} - 4\pi G\bar{\rho}\delta_k = 0 \tag{5.13}$$

which has the general solution

$$\delta_k(t) = A(\bar{k})D_1(t) + B(\bar{k})D_2(t) \tag{5.14}$$

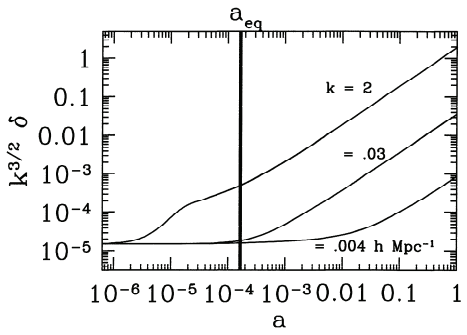

Figure 5.2: (From Dodelson (2003)) Evolution of perturbations for three different modes to the dark matter. The small scales enter the horizon well before matter/radiation equality. The growth is retarded starting at a 10^{-5} after the mode has enter the horizon and ending at a 10^{-4} when the universe becomes matter dominated. Well after a_{eq} all subhorizon modes evolve identically, scaling as the growth factor in a at matter dominated universe.

The partial solutions $D_1(t)$ and $D_2(t)$ are the growing and decaying modes that are not dependent on $\bar{k}$ and $A(\bar{k})$ and $B(\bar{k})$ are complex valued initial conditions. If, at some early time, both functional dependences were present, the increasing solution will dominate at later times, whereas the solution decreasing with time will become irrelevant. Therefore, for our purpose only this solution, $D_1(t)$ is relevant and we will study the general solution bellow. Note that $D_1(t)$ is the growth function $D(t)$ introduced in 5.2.1.

Now we want to study the linear perturbations from horizon entry to the present time, therefore we include the growth of perturbations even during the radiation domination period (see Figure 5.2). In this case, the radiation component ρ_r is taken as a smooth background component ($\rho_r = \rho_s$) and affects only the overall expansion rate. These background solution is governed by the Friedmann Equations 2.20 and 2.21, but the perturbation equations are the Newtonian perturbations equation (e.g. Peacock (1999)).

We get again the Equation 5.11 when $c_s = 0$. The difference is that now the gravity term still contains only the matter component, but the expansion law, $H(t)$ comes from the full background energy density $\bar{\rho} = \bar{\rho}_m + \bar{\rho}_s$.

At very early times, for scales greater than the horizon in the framework of Relativistic perturbation theory, perturbations in matter and radiation can grow together, so uctuations at early time grow at the same rate, independent of the wavenumber.

During the radiation domination epoch, CDM perturbations inside the horizon ($a_{enter} < a_{eq}$) evolved according the Meszaros effect (Peacock (1999)). The increased expansion rate due to the presence of a smooth component slows down the growth of dark matter perturbations. As the horizon gets larger with time, uctuations on bigger scales enter the horizon and cease to grow. However, for large enough scales, uctuations never enter the horizon and thus never halted their growth.

For uids (baryons) is the radiation pressure that prevents the perturbations from collapsing futher. For dark matter the rapid radiation driven expansion prevents the perturbation from growing until matter radiation equality (a_{eq}).

As we will see in next section, the Meszaros effect explain the qualitative behavior of the transfer function and thus, is critical in shaping the power spectrum.

As the universe get closer to matter domination, the pressure of the radiation becomes less important, and the perturbations begin to grow faster. When the CDM perturbations enter the horizon during the matter dominated epoch, the growth increases smoothly to $\delta \quad a$. Finally, in the era dominated by the cosmological constant, the perturbations are even entirely frozen (Knobel (2012)).

5.2.2.2 Linear Growth Function

The linear growth factor is easily solvable for any cosmological model. In the case where there is only matter and vacuum energy, it admits the integral representation as a function of Ω_m and Ω_Λ (Heath (1977))

$$D(a) = H(a)\frac{5\Omega_m}{2}\int_0^a \frac{da'}{[a'H(a')]^3} \tag{5.15}$$

Although this integral can be easily solved numerically, it is common to use the fitting formula that provides an accurate approximation at low redshift (Caroll et al. (1992))

$$D(z) \approx \left(\frac{5}{2}\right)\frac{\Omega_m(z)/(1+z)}{\Omega_m(z)^{\frac{4}{7}} - \Omega_\Lambda(z) + (1+\Omega_m(z)/2)(1+\frac{\Omega_\Lambda(z)}{70})} \tag{5.16}$$

In this thesis we will solve it numerically using the interactive software package iCosmo for low redshift universe. The code is freely available with documentation at http://www.icosmo.org.

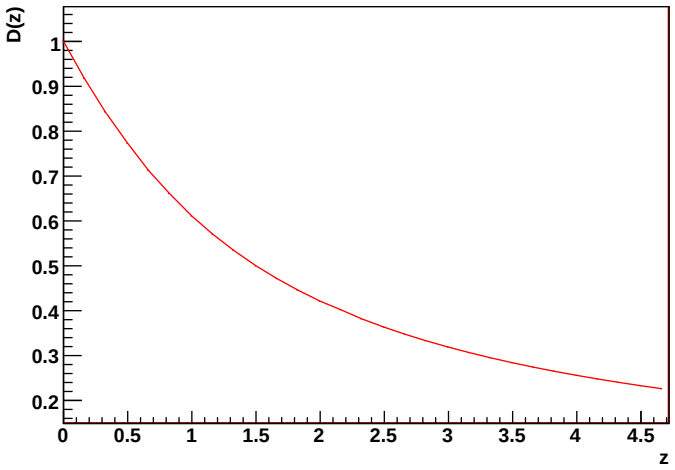

Figure 5.3: Growth function for Hubble Volume simulation ΛCDM cosmological parameters

For a at and matter dominated Universe the growth factor is simply equal to the scale factor for late times, $D(t) = a = 11 + z)$. Figure 5.3 shows the growth factor for ΛCDM cosmology using iCosmo. If we compare both models, growth is suppressed at late times for dark energy cosmologies. Whatever structure is observed today in a dark energy Universe was likely in place at much earlier times than in a a at and matter dominated Universe. (Dodelson (2003)).

5.2.3 Transfer Function

The real power spectra results from modifications of any primordial power by a variety of process: growth under self-gravitation, the effects of the pressure and dissipative processes. Now, we sum up the overall effect in the form of the linear transfer function and consider the dynamics of the perturbations outside the horizon (Peacock (1999)).

To obtain the precise form of it at all scales, one has to solve the general relativistic Boltzmann equation (Dodelson (2003) taking into account all sorts of energy in the Universe and the effect of these coupled perturbations. It includes the effect of matter and relativistic particles which does not behave as a simple uid. Solving for the exact transfer function is a complicated business, due to the coupling of photons and baryons.

There are in essence two ways in which the power spectrum that exists at early times may differ from that which emerges at the present, both of which correspond to a reduction of small scale uctuations (Peacock (1999)): 1)the Jean mass effects in CDM or baryon component, and 2) damping effects such

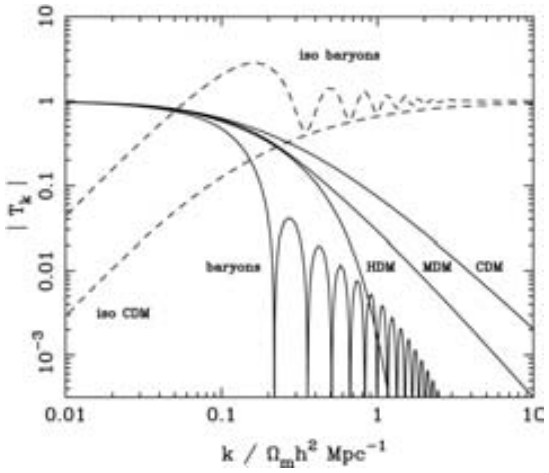

Figure 5.4: Transfer function for various adiabatics models, in which $T(k)$ 1 at small k (Peacock (1999)). The opposite is true for isocurvatures models. A number of possible matter contents are illustrated. For dark matter models the characteristic wavenumbers scales proportional to Γ, marking the break scale corresponding to the horizon length at matter-radiation equality, L_0. The scaling for baryonic models ($\Omega_m = 1$, $h = 0.5$) does not obey this exactly and contains the effect of the BAO.

as Silk damping of baryonic acoustic oscillation (BAO) (Silk (1968)) or free streaming of CDM.

Eisenstein and Hu (1998) employ the analytic small scale solution to derive an accurate fitting formula that move beyond those presented by Bardeen et al. (1986). They develop a formula for the matter transfer function for adiabatic CDM cosmologies that account for all baryons effects such acoustic oscillation, Silk damping, and cold dark matter suppression. The fitting formula is excellent to provide physical insight into the form of the power spectrum but it has high deviations with respect to the exact solutions (Sánchez et al. (2008)).

There are numerical codes to solve the multi species Boltzamnn equations that provide a more accurate calculations . In this thesis we choose the code called CAMB (Lewis and Bridle (2002)) based on CMBFAST (Seljak and Zaldarriaga (1996)) that compute the transfer function and the CMB power spectra.

Figure 5.4 shows the different shapes of the functions which are obtained for different components. The transfer function for dark matter has an asymptotical behavior. The bend visible is due to the Meszaros effect which continues until the universe is matter dominated. We therefore expect a turnover in the power spectrum around the comoving horizon scale at the epoch of equality ($L_0 = r_{H,com}(z_{eq})$). In conclusion, the shape of the transfer

function for dark matter depends on the combination kL_0, and thus on the shape parameter $\Gamma = \Omega_m h$.

The transfer function for baryons contains the effect of acoustic oscillations (BAO) before the universe become matter dominated leading to a strong oscillation pattern in $T_b(k)$. These oscillation are then transfered by gravitational interactions to the spatial distribution of dark matter particles producing a weak oscillation pattern in $T(k)$.

5.2.3.1 Evolution of baryonic density uctuations and BAO

The evolution of density uctuations of baryons differs from that of dark matter due to the interaction of baryons with photons via Thompson scattering. At early times there is a close coupling between the electrons, nuclei (baryons) and photons. The radiation pressure of photons is large compared to the gravitational forces in the perturbations until the recombination begins, with the result that perturbations in the baryon-photon uid oscillate as sound waves following the Jeans criteria (Peebles and Yu (1970); Sunyaev and B.Zeldovich (1970)) and with a decreasing amplitude due to Silk damping.

As the Universe passes from radiation to matter domination, CDM uctuations are allowed to collapse. After recombination, the photons decouple from the perturbations in the baryons and soon become smoothly distributed. The perturbations in the baryons are now subject to gravitational instability, just like the dark matter perturbations. The baryonic perturbations are allowed to collapse and fall within the dark matter potential wells to create the first stars, globular clusters and galaxies, establishing the bottom-up hierarchical scenario of structure formation. This mechanism then guaranties that the tiny baryonic uctuations can grow to generate the large uctuations that we observe today.

The acoustic oscillations are present in the matter power spectrum as series of damped oscillations. In the correlation function, this is translated into an excess of pairs at approximately (not equal, see Sánchez et al. (2008)) the scale of the sound horizon. This scale can be computed as the comoving distance that the sound waves could travel from the Big Bang until recombination at $z = z*$ (Hu and Sugiyama (1996); Eisenstein and Hu (1998)).

The first convincing detections of BAO came in 2005 from de SDSS Data Release (DR3) and final 2dFGRS samples(Eisenstein (2005);Cole (2005)). Eisenstein (2005) measured the large scale correlation function of Luminous Red Galaxy (LRG) sample and Cole (2005) measured the power spectrum of 2dFGRS galaxies. After that, the rapid development of the theory became the BAO as one of the leading methods for study dark energy.

5.3 Power Spectrum

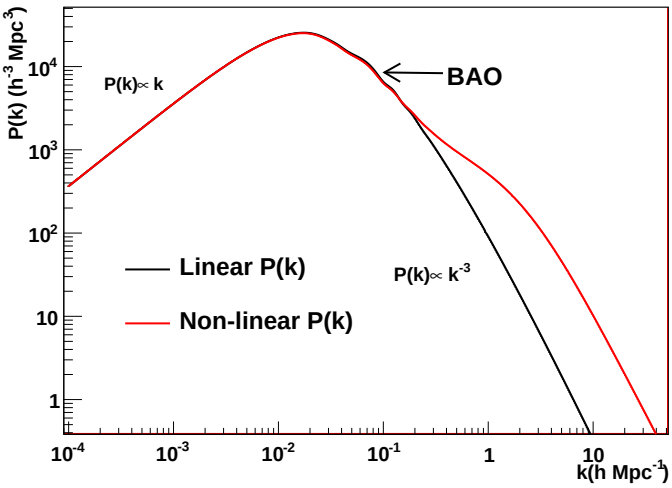

Figure 5.5: The linear power spectrum using CAMB code (black line) and non linear power spectrum using Halo-fit code (red line) for Hubble Volume Simulations ΛCDM cosmological parameters.

As we explain in the last sections the initial spectrum $P_i(k)$ is processed to yield $P(k)$ today. We have demonstrated that the linear power spectrum of the density uctuations (Equation 5.4) can be predicted in the framework of a CDM model, except for its normalization A which has to be measured empirically from observations as we will describe bellow in Section 5.4.3.

Figure 5.5 shows the linear power spectrum today for ΛCDM cosmology. Small scale uctuations (large k) were processed as they entered the horizon. They will be affected first and experience the strong suppression to their amplitude. The power spectrum follows a power law, $P \quad k^{-3}$. Large scale uctuations (small k) should retain their primordial shape, $P \quad k$. They will be unaffected until they enter the horizon after matter domination equality. The turnover point in the processed power spectrum is an indication of the horizon size at epch of equality.

Since the baryonic component is forced to oscillate displaying acoustic peaks, this also predicts the presence of BAO in the CDM power spectrum, though with smaller amplitude.

Rather than working with $P(k)$ itself, it is often more convenient to use the dimensionless quantity

$$\Delta^2(k) \equiv \frac{k^3 P(k)}{2\pi^2} \tag{5.17}$$

which is the power per logarithmic interval in wavenumber. Small Δ corre-

spond to small inhomogeneities, while large Δ indicates non-linear perturbations.

The deviations from the linear power spectrum appear due to mode coupling of the Fourier modes at low redshift, generating an increase in the power at small scales. The contribution of this non-linearities is practically negligible at early times and becomes more important as perturbations grow. An important scale to keep in mind is the scale above nonlinearities can't be ignored. This is roughly set by $\Delta(k_{nl})$ 1, which correspond to $k_{nl} = 0.2h^{-1}Mpc$ in most models (Dodelson (2003)). In Figure 5.5 the non-linear power spectrum is generated using Halo-fit code (Lewis and Bridle (2002)) and this will be our choice in this thesis. In Chapters 6 and 7 the non-linearities and their effects will be studied more in detail. In particular, in Section 7.2.1 we will describe the non linear power spectrum using the halo model formalism.

5.4 Statistic of Density Fluctuations

In order to characterize the structure in the universe and to compare observations of δ with theory, the theory of random fields is used. (For a detailed presentation of the theory of random fields and their realizations see, for example, the classical monograph by Adler (1981). We regard δ as a realization of a homogeneous and isotropic random field with zero mean, $\delta = 0$. The main features of such realizations depend on initial conditions and the way that those initial uctuations evolve with time.

Since all statistics of random fields are meant to be measured averaging over ensembles of fields, in cosmology we introduce the concept of ensemble of universes. N-body simulations of the Universe can be used to create large set of realizations with the same initial condition. A large statistical ensemble of universes are equivalent if they density fields δ have the same statistical properties. They cannot reproduce our Universe; instead, they are at best able to generate cosmological models that have the same statistical properties of our Universe.

However, the observable universe constitutes a single realization of this process, so the question arises how these ensemble averages ... might be measured in practice. Because we have only one universe, we can never get our hands on an ensemble, and we have to suppose that our field are ergodic or postulate the fair sample hypothesis.

Ergodicity refers to the mathematical property of random fields that volume averages converge to ensemble averages as the survey goes to infinity. In general it is hard to prove that a random field has this property. However, it can be shown that a zero mean, homogeneous, real Gaussian random field is ergodic if $\xi(r)$ 0 for r Adler (1981). This condition allows us to infer statistic of cosmological fields from the study of one realization of the

Universe and measure the correlation function $\xi(r)$. Of course, we have must always keep in mind that it is possible to have a universe with non-gaussian initial conditions.

On the other hand, the fair sample hypothesis (Peebles (1980)) states that we should look at widely separated parts of the space since the δ fields there should be causally unconnected. They can be regarded as independent realizations of the underlying stochastic process. Therefore the observable universe would contain many such realizations.

Whichever hypothesis finally applies, most present day galaxy surveys are too small (especially at high redshift) to constitute a fair sample and thus averages over the volumes of such surveys are subjected to statistical uctuations. This is called sample variance or cosmic variance if the sample is constrained by the size of the observable universe.

In this thesis we use N-body simulation with a single realization of the Universe to test our method before test in cosmological observations that are more di cult.

5.4.1 Two Point Correlation Function and Power Spectrum

The δ field inhabits a universe that it is isotropic and homogeneous in its large scale properties ($\delta = 0$) although it describes inhomogeneities. The two point correlation function is a second order statistic (second order moment of the density field) that characterizes these inhomogeneities and describe the matter density distribution. It traces the amplitude of the clustering of objects as a function of scale. Its importance in cosmology has been fully discussed by Peebles (Peebles (1980)).

The two point correlation function has been the mainstay of clustering studies for over the last forty years. There are two sorts of two point function. One describing the clustering as projected on the sky, thus describing the angular distribution of objects in a catalog. This is called the angular two point correlation function and is generally denoted by $w(\theta)$. The other describes the clustering in space and is called the spatial two point correlation function, $\xi(r)$. We frequently omit the word "spatial".

In order to provide a mathematical definition of the correlation function we will only consider the spatial two point function because this will be our choice for this thesis. The definition of the angular function follows similarly.

The two point correlation function of the overdensity field is given by (Peebles (1980))

$$\xi(\bar{x}_1, \bar{x}_2) = \delta(\bar{x}_1)\delta(\bar{x}_2) \tag{5.18}$$

Since our random field is homogeneous and isotropic, the correlation function can only depend on $\bar{r} = (\bar{x}_1 - \bar{x}_2)$ and

$$\xi(\bar{x}_1, \bar{x}_2) = \xi(\ \bar{x}_1 - \bar{x}_2\ ) \tag{5.19}$$

For $\bar{r} = 0$,

$$\xi(\bar{x}_1, \bar{x}_2) = \delta^2 = \sigma^2 \tag{5.20}$$

where σ^2 is the variance if the isotropic random field.

We want to explain the meaning of the two correlation function in a straightforward manner,so Equation 5.18 can be rewritten as Peebles (1980)

$$\rho(\bar{x}_1)\rho(\bar{x}_2) = n^2[1 + \xi(\bar{r})] \tag{5.21}$$

where ones defines the mean value of the density field as $n = \rho(\bar{r})$.

If $\rho(\bar{r})$ represents the density of a distribution of objects in space, the probability of finding a single object in a differential volume is just $\delta P = \rho(\bar{r})\delta V$. Likewise, the joint probability of finding two objects in two differential volumes δV_1 and δV_2 is just the product of individual probabilities, given by

$$\delta P = \rho(\bar{r}_1)\rho(\bar{r}_2)\delta V_1 \delta V_2 \tag{5.22}$$

If one averages this expression over all possible pairs of positions, leaving the result only in terms of the separation distance $\bar{r}$ between the two objects, and applies Equation B.1 then (Peebles (1980))

$$\delta P = n^2[1 + \xi(r)]\delta V_1 \delta V_2 \tag{5.23}$$

Thus, as indicated by Equation 5.23, the correlation function determines the probability of finding two objects at separation r in excess of the probability one would expect for independent distributions. If two distributions are uncorrelated, the probability of finding two objects, one in each distribution, is just the product of probabilities, given by $n^2\delta V_1 \delta V_2$.

5.4.1.1 Fourier Analysis of Density Fluctuations

The correlation structure is much simpler if we decompose the field in Fourier modes $\delta(\bar{k})$. The Fourier analysis is the natural tool to study a field as a superposition of many modes for a at comoving geometry. For other models, plane waves are not a complete set although normally this is neglected because the difference only matters on scales of order the present-day horizon (Peacock (1999)).
We represent the real space uctuations in the homogeneous density field as a sum over the Fourier modes

$$\delta(\bar{x}) = \Big(\frac{1}{2\pi}\Big)^3 \int \delta(\bar{k}) \exp(i\bar{x} \cdot \bar{k}) d^3k \tag{5.24}$$

and the inverse

$$\delta(\bar{k}) = \int \delta(\bar{x}) \exp(-i\bar{x} \cdot \bar{k}) d^3x \tag{5.25}$$

With this definitions the correlation function of our Fourier transformed quantities is given by

$$\delta(\bar{k}_1)\delta(\bar{k}_2 \ = (2\pi)^3\delta_D(\bar{k}_1 - \bar{k}_2)P(\bar{k}_1) \tag{5.26}$$

where $P(\bar{k}_1)$ is the spectral density of the field called the power spectrum

$$P(k) = \ \delta_k \ ^2 \tag{5.27}$$

and δ_D is the Delta Dirac function which constrains $\bar{k}_1 = \bar{k}_2$, meaning that the Fourier amplitudes are independently distributed.

Because $\delta(\bar{x})$ is real, we have $\delta(\mathbf{k}, t) = \delta(-\mathbf{k}, t)$ and the above formula can be written as

$$\delta(\bar{k}_1)\delta(\bar{k}_2 \ = (2\pi)^3\delta_D(\bar{k}_1 + \bar{k}_2)P(\bar{k}_1) \tag{5.28}$$

All these equations define the correlation function. Inserting the Fourier decomposition into Equation 5.18 yields

$$\xi_2(\mathbf{r}) = \frac{1}{(2\pi)^3}\int d^3\mathbf{k}\ \delta(\mathbf{k})\ ^2 \exp(-i\mathbf{k}\cdot\mathbf{r}) \tag{5.29}$$

In an isotropic universe, the spectral density cannot contain a preferred direction and must be a function of the norm $k = \ \mathbf{k}\ $. Therefore we have a isotropic power spectrum: $\delta\ ^2(\mathbf{k}) \ = \ \delta\ ^2(k)$ and the above formula can be simplified, integrating over angles first. In three dimensions, this yields

$$\xi(r) = \frac{4\pi}{(2\pi)^3}\int P(k)\frac{sin(kr)}{kr}k^2 dk \tag{5.30}$$

5.4.2 Gaussian Density Fields

In general, knowing the correlation function or the power spectrum is not sufficient to unambiguously describe and characterize any random field. However, the statistical nature of the isotropic homogeneous Gaussian density field with zero mean is completely specified by them (Bardeen et al. (1986)).

The Gaussian field is the simplest class of random field to describe a n-point joint probability distribution because it is a multivariate Gaussian

$$f(\delta(\mathbf{x}_1), ..., \delta(\mathbf{x}_N)) = \frac{1}{(2\pi)^{\frac{N}{2}}\sqrt{det(V)}}\exp\Big(-\frac{1}{2}\sum_{i,j=1}^{N}\delta(\mathbf{x}_i)(V^{-1})_{ij}\delta(\mathbf{x}_j)\Big) \tag{5.31}$$

where $V_{ij} \ = \ \xi(\ \mathbf{x}_i - \mathbf{x}_j\ )$ is the covariance matrix. Hence the correlation function $\xi(r)$ determines the random field entirely.

An important property of Gaussian random fields is that the Fourier transform of a Gaussian field is still Gaussian. Each Fourier mode $\delta(\mathbf{k})$ has a real and imaginary part which are independent and Gaussian distributed

with zero mean and dispersion $P(k)/2$. Additionally, each k-mode is independent from the others in contrast to the values of the $\delta(x)$ at different points in real space.

Moreover, gaussian fields play an important role in cosmology because the initial perturbation due to in ation are assumed to be Gaussian in the linear regime. During the evolution of the structure they evolve gradually away from Gaussianity. As an example, the matter density field $\rho(\mathbf{x})$ is close to Gaussian at the beginning, but that tends to be closer to lognormal at later stages (Coles and Jones (1991)).

The higher-order irreducible correlation functions and spectra of a Gaussian field are identically zero, so their determination from observations is a good test for Gaussianity of the field. .

5.4.3 Filtering and Normalization of the Power spectrum

In order to normalize the power spectrum and provide a whole set of useful statistically parameters to characterize a density field, it is very useful to look at the density fields convolved, or filtered. We have to take into account that objects have a finite size and we are not interested usually in the behavior of the field at smaller scales. Mathematically, this is obtained by convolving the matter density field with some window function $W(r;R)$ on a certain scale R.

We are often interested not only in the convolved field itself, but in its variance, for use as a statistic. Therefore, we study the statistical moments of the filtered linear overdensity field where the variance is the second moment and can be expressed by the linear power spectrum as

$$\sigma(R)^2 \equiv \ \delta(r;R)^2 \ = \frac{1}{(2\pi)^3}\int \ W(k;R)\ ^2 P_{lin}(k) d^3k \tag{5.32}$$

where $W(k;R)$ is the Fourier transform of the window function $W(r;R)$. The smoothing functions are selected because they yield simple analytical expressions and posses a well-defined volume. The most common filters are the spherically symmetric Gaussian and the top hat. For our calculations we use a top hat function

$$W(r;R) = \frac{3}{4\pi R^3}\theta(R-r) \tag{5.33}$$

where $\theta(x)$ is the theta-function. Its Fourier transform is given by

$$W(k,R) = \frac{3}{(kR)^3}(sin(kR) - (kR)cos(kR)) \tag{5.34}$$

The effective volume for this filter is

$$V = \frac{4\pi}{3}R^3 \tag{5.35}$$

The volumes are necessary when we wish to define objects by their mass. Therefore the two relevant mass and length scales, M and R, are related by calculating the mass contained in a sphere of the given mean density, that is, $M = \frac{4\pi}{3} R^3 \bar{\rho}$.

We have demonstrated in previous section that the power spectrum of the density uctuations can be predicted in the framework of a CDM model, except for its normalization which has to be measured empirically.

The first method to set the amplitude of power spectrum is to measure the uctuations in the cosmic background radiation (CMB). The COBE satellite measured them for the first time in 1992. Later, WMAP and Planck missions complements and improves these observations . These uctuation are caused by the uctuations of the initial gravitational potential, so the uctuations of the temperature of the CMB can be used to describe the density uctuations at recombination. The main reference for this normalization is the paper by Bunn and White (1997).

Another method of normalization is by the value of σ_8, defined as the square root of the variance with a window function with radius $R = 8h^{-1}Mpc$. This value of the radius is considered to be approximately the smallest scale where the dynamics is still almost linear. σ_8^2 is given by

$$\sigma_8^2 = \ \delta(r; R = 8h^{-1}Mpc)^2 \tag{5.36}$$

This value does not coincide with the observed rms variation of galaxy counts $\sigma_{8,g}$, which differs from σ_8 by the bias factor and by the effects of non-linear dynamical evolution. Thus, σ_8 should be treated as only a normalization constant.

Leaving aside non-linear corrections, we know from observed inhomogeneities in the local Universe that $\sigma_{8,g}^2 = 1$. Since the connection between dark matter and galaxies or cluster of galaxies is parametrized by the linear bias parameter factor b, we then obtain

$$\sigma_8 \approx \frac{1}{b} \tag{5.37}$$

Once we know the CMB normalization and the cosmological parameters, we can calculate σ_8, so it is not really a free parameter.

The clustering analysis focused on the amplitude of the power spectrum contains degeneracies between cosmological parameters, especially on σ_8 and Ω_m. This is due to the fact that these parameters in uence the strength of the matter uctuations in the same way. As we will see in Chapter 3, probes like cluster abundance have been introduced to break these degeneracies.

Chapter 6

The Abundance of Dark Matter Halos

Abstract:

One of the exciting developments of 1990s was the evolution of a number of techniques to study the abundance of galaxy clusters (called cluster mass function) as a function of mass and redshift. In addition to the brute-force approach of numerical simulations there are semianalytical techniques which have been remarkably successfully at prediction properties and abundances of different galaxy types. The Press and Schechter theory (Press and Schechter (1974)) forms the basis of this work and assume that objects collapse spherically to produce spherical dark matter halos. In Section 6.2 we explain the spherical collapse model and derive the model for the abundance of dark matter halos. Later in Section 6.3 we will introduce the more realistic ellipsoidal collapse and the calibrated formulas or fitting formulas from N-body simulations which provide more accuracy. Finally in 6.4 we will test this models in N-body simulations.

6.1 Introduction

The evolution of structures like clusters of galaxies cannot be treated within the framework of linear perturbation theory described in the last chapter. The non-linear evolution is more complicated. There are no general analytical solutions so it is necessary to use numerical methods such N-body techniques simulation (i.e., Bertschinger (1998) and Kuhlen et al. (2012)) to study the general case.

Although the full development of the gravitational instability cannot be solved exactly without N-body techniques, there are some very useful special cases and approximations that help us to understand the general case such the model of spherical collapse.

Clusters are formed when density fluctuations δ reach some critical threshold density δ_C and then collapse. However, in this chapter we will study the collapse and virialization of dark matter called dark matter halos. The direct link between the dark matter simulations and the observed properties of the Universe requires understanding of the relation of dark matter and the observable. We will return to these aspects later.

6.2 The Spherical Collapse Model and the Mass function

6.2.1 The Spherical Top Hat Collapse

The spherical top hat collapse model was first studied by Gunn and Gott (1972). Despite being a simplistic model, it represents the fundamental principles of gravitational collapse and yields approximate relations for collapse time and mean density inside the virialized region, as they are found from numerical simulation (Schneider (2006)).

We will follow the evolution of a spherical density perturbation that is embedded in a homogeneous background universe, from early times to gravitational collapse and virialization (Peacock (1999)). Because of Birkoff's theorem and the condition of spherical symmetry, the perturbation and the background evolves independently.

An overdense sphere is a very useful nonlinear model, as it behaves in exactly the same way as a closed sub-universe. The density perturbation need not be a uniform sphere: any spherically symmetric perturbation will clearly evolve at a given radius in the same way as a uniform sphere containing the same amount of mass. Therefore, density refers to the mean density inside the given sphere (Peacock (1999)).

How can we describe the dynamics of the perturbation? We treat the perturbation as a miniature FRW universe with higher density than the background. The perturbation is sufficiently large that we can neglect the local influence of cosmological constant.

The equation of motion of the radius is the same as the scale factor given by the Friedmann Equation 2.20 when $\Omega_\Lambda = 0$. It can be most easily solved if it is expressed in terms of the conformal time $d\eta = cdt/R$. Assuming that $\rho(t)$ can be written as $\rho(t) = \rho_0 R_0^3/R^3$ because of the conservation of the matter we then have

$$\left(\frac{dR}{d\eta}\right)^2 = \frac{8\pi G\rho_0 R_0^3}{3c^2} R - kR^2 \tag{6.1}$$

Defining the characteristic radius R_* as a useful scaling constant

$$R_* \equiv \frac{4\pi G\rho_0 R_0^3}{3c^2} \equiv \frac{GM_*}{c^2} \tag{6.2}$$

where M_* is the mass initially enclosed in our overdense sphere or the characteristic mass,the equation 6.1 is rewritten in terms of R_*

$$[\frac{d}{d\eta}\Big(\frac{R}{R_*}\Big)\Big]^2 = 2\Big(\frac{R}{R_*}\Big) - k\Big(\frac{R}{R_*}\Big)^2 \tag{6.3}$$

We are interested in the formation of the object, so we choose the case k=+1 when the expansion will change to contraction at a certain R. The solution is the well known cycloid. The two equations which completely describe the evolution of a spherically symmetry overdensity are thus

$$R(\eta) = R_*(1 - cos(\eta)) \tag{6.4}$$

$$t(\eta) = \frac{R_*}{c}(\eta - sin(\eta)) \tag{6.5}$$

For simplicity we assume that the equations of the motions of the background are the same as the scale factor (Friedmann Equation 2.20) for a matter dominated universe with $\Omega_\Lambda = 0$ and $k = 0$ (Einstein-de Sitter model)

$$\dot{a}^2 = \frac{8\pi G}{3}\bar{\rho}a^2 \tag{6.6}$$

with the solution $a(t)$ $t^{2/3}$. Inserting this solution into the Friedmann equation we obtain the explicit time dependence of the background density

$$\bar{\rho}(t) = \frac{1}{6\pi G t^2} \tag{6.7}$$

Using the Equations 6.4, 6.5 and 6.7 we can compute the full non-linear growth of the spherical overdensity as

$$\delta(\eta) + 1 = \frac{\rho(\eta)}{\bar{\rho}(\eta)} = (\frac{M}{4\pi R(\eta)^3/3})/(\frac{1}{6\pi G t(\eta)^2}) = \frac{9(\eta - sin(\eta))^2}{2(1 - cos(\eta))^3} \tag{6.8}$$

We can now take a look to the several states of evolution of the overdensity

Evolution for $\eta << 1$ (Linear regime) In order to describe the early expansion of the sphere, we expand the relation 6.8 to the first non vanishing order in η yielding

$$\delta(\eta) \quad \frac{3}{20}\eta^2 \tag{6.9}$$

The leading order terms for 6.4 and 6.5 are given by

$$R(\eta) \quad R_*\frac{\eta^2}{2} \tag{6.10}$$

$$t(\eta) \quad \frac{R_*}{c}\frac{\eta^3}{6} \tag{6.11}$$

so that eliminating η using the last equation we obtain

$$\delta(t) \quad \frac{3}{20}\Big(\frac{6ct}{R_*}\Big)^{\frac{2}{3}} \equiv \delta_{lin}(t) \tag{6.12}$$

We recover the results from linear perturbation theory for a matter dominated Einstein de Sitter universe since $\delta(t)$ is small at early time. The sphere expands with $a \quad t^{2/3}$ and density perturbations grow proportional to a, in accordance with the expansion of background universe.

As time passes, the perturbation grows and leaves the linear regime. There are three interesting epoch in the final stages of its development, which we can read from the cycloid solution. We compare the density enhancement of our evolving sphere relative to the cosmological background

Turnaround The sphere breaks away from the general expansion and reach the maximum radius at $\eta = \pi$. Therefore, the kinetic energy is zero. This state mark the epoch when the perturbation decouples entirely from the Hubble ow of the homogeneous background. At this stage the overdensity relative to the background is

$$1 + \delta_{max} = \frac{9\pi^2}{16} \tag{6.13}$$

Collapse If only gravity operates, then the sphere will collapse to a singularity at $\eta = 2\pi$. This occurs when $\delta_{lin} \quad 1.69$, which will be renamed as critical overdensity, δ_c.

Virialization The sphere will no really collapse to a single point; dissipative physics will eventually intervene and convert kinetic energy of collapse into random motions. The particles will scatter on these uctuations in the gravitational field and will virialize. Nonetheless, the threshold density δ_c is useful because it indicates when a perturbation enters the non-linear regime.

At the equilibrium the total kinetic energy is related to the potential energy by the virial theorem

$$V = -2K \tag{6.14}$$

To find the size of the halo, we search for the radius R_{vir} for which the virial condition 6.14 is satisfied. Since at the turnaround $E_{total} = V(R_{max})$ we obtain

$$R_{vir} = \frac{1}{2}R_{max} = R_* \tag{6.15}$$

In the spherical top hat model, following 6.4, this will occur at $\eta = \frac{3\pi}{2}$. However, some authors prefer to assume that the process of virialization take a little longer than the predicted by our symmetric model, and it is common to assume that R_{vir} is in fact reached at collapse (Peacock (1999)). In this case the full non-linear density contrast for an Einstein-de Sitter model is

$$\Delta_{vir} = 1 + \delta_{vir} \equiv \frac{9(\eta - sin(\eta))^2}{2(1 - cos(\eta))^3}_{\eta=\frac{3\pi}{2}}^{\eta=2\pi} = \frac{9}{2}(2\pi)^2 \quad 178 \tag{6.16}$$

Peacock (1999) derives an approximate expression for $\Omega_\Lambda = 0$ models

$$\Delta_{vir} = 1 + \delta_{vir} \quad 178\Omega_m^{-0.7} \tag{6.17}$$

For at Λ dominated models, Eke et al. (1996) give an analytical prescription. He calculates the lower Ω_m dependent critical thresholds from the spherical collapse solutions of Lahav et al. (1996) and Lilje (1992). The results show that, while δ_c is rather insensitive of the presence of cosmological constant, Δ_{vir} decreases for increasing Ω_Λ. Bryan and Norman (1998) provide a fitting formula for the density contrast at virialization of Eke et al. (1996) when $\Omega_{rad} = 0$ which it is accurate to 1% as

$$\Delta_{vir} = 18\pi^2 + 82\Omega_m(z) - 39\Omega_{mat}(z)^2 \tag{6.18}$$

Questions arise about the validity of the assumption of spherical symmetry in this analysis, especially as we would expect in general that overdense or underdense regions in our universe will be quite aspherical. It is found, however, that a density contrast 100-200 turns out to be quite successful at defining and hence finding halos in N-body simulations. A commonly used definition of the mass of a halo is M_{200}, defined as the mass encompassed by a sphere centered on a halo which $1 + \delta_{vir} = 200$. Such a virialized mass concentration of dark matter is called dark matter halo.

Later in Section 6.3.1 based on these concepts we will describe more the mass of the halo in numerical simulations.

6.2.2 The Dark Matter Halo Mass Function and the Press Schecther Theory

The halo mass function $\frac{dn}{dM}$ of dark matter halos is the comoving number density of halos with mass between M and $M + dM$ at a given redshift z. It is a key element to understand the distribution of matter and clusters of galaxies in the Universe. As we will see in next chapter, it sets the relative weighting for the different mass regimens in integrals used to determine the statistic of matter density and galaxy number density fields and thus plays an important role in determining the bias (see Equation 7.40 to obtain the averaged bias).

Here we start with a derivation of the Press-Schechter (Press and Schechter (1974)) (hereafter PS) mass function. Later, in Section 6.3, we proceed to discuss the fits to the halo mass function observed in N-body simulations.

The PS formalism is an attempt to analytically estimate the abundances of bound virialized objects in the Universe based on the assumption that these objects are formed following the spherical collapse model.

PS assume that the distribution of values of this linear density δ is Gaussian. Therefore, the probability that a given point lies in a region with $\delta > \delta_c$ required for a halo to collapse is

$$p(\delta > \delta_c; R_f) = \frac{1}{\overline{2\pi}\sigma(R_f)} \int_{\delta_c}^{\infty} exp\left(\frac{-\delta_M^2}{2\sigma^2(R_f)}\right) d\delta \tag{6.19}$$

$$= \frac{1}{2}\left[1 - erf\left(\frac{1}{\overline{2}}\frac{\delta_c}{\sigma(R_f)}\right)\right] \tag{6.20}$$

where R_f is the radius over which the density field has been smoothed. This radius is used to computed $\sigma^2(R_f)$, the variance of the smoothed linear power spectrum given by Equation 5.32. This expression can be expressed in terms of the linear power spectrum at z=0 $P_{lin}(k)$ as

$$\sigma^2(R_f) = D(z)^2\sigma_0(R_f)^2 = D^2(z) \int \frac{dk}{k} \frac{k^3 P_{lin}(k)}{2\pi^2} \, W(kR_f)^{\,2} \tag{6.21}$$

where $D(z)$ is the growth function explained in detail in Section 5.2.2.2 and δ_c is defined before. As we discuss in 5.4.3, the filter function $W(r; R_f)$ has some characteristic length R_f. The typical size of the filtered uctuations will be $\sim R_f$ and they can be assigned a mass $M \sim \rho R_f^3$.

The probability given by Equation 6.20 predicts the fraction of the volume that has collapsed into objects of mass $> M$. To get these fraction into a form more comparable with observations, we differentiate $p(\delta > \delta_c; R_f)$ with respect to M and multiply by a small interval dM. This gives the fraction of volume collapsed into objects in the range dM. Then multiply by the average number density of such objects $\frac{\bar{\rho}_m}{M}$ to get the number density of collapsed objects with mass between M and $M + dM$,

$$dn(M, z) = \frac{\bar{\rho}_m}{M}\left|\frac{dp}{dM}\right| dM \tag{6.22}$$

A factor of 2 had to be added into their model to match with simulations (Peacock (1999)). Thus, in terms of the variance this is

$$\frac{dn}{dM} = \frac{\bar{\rho}_m}{M^2}\left|\frac{dln\sigma}{dlnM}\right| \sqrt{\frac{2}{\pi}} \frac{\delta_c}{\sigma(R_f)} exp\left(-\frac{1}{2}\left(\frac{\delta_c}{\sigma(R_f)}\right)^2\right) \tag{6.23}$$

There is a typical mass scale, M_* at which the variance is $\sigma(M_*) = \delta_c$. For $M << M_*$ the mass function is close to a power law $\frac{dn}{dM}$ M^{-2}, and is exponentially cut off for $M \geq M_*$. Examples of the mass function will given in Section 6.4.

The factor 2 has long been recognized as the crucial weakness of the PS analysis. The problem was resolved after Bond et al. (1991) and Peacock and Heavens (1990) found physically motivated solutions within the so-called excursion set approach or extended PS theory.

We learn from this analysis that PS approach is a very simple model, based on assumptions that are not really justified in detail. Apart from the ad-hoc modifications, such as the multiplication by a factor of 2, it suffer from other drawbacks. First, the collapse of dark matter halos is a spherical symmetric process. Second, the collapse fraction is obtained using linear σ and finally the distribution of inhomogeneities is gaussian. Nevertheless, its predictions are in astounding agreement with the number density of halos from simulations.

6.3 Halo Mass Function in Numerical Simulation

Only since the mid-1990s, the numerical simulations have the precision and statistic to reach a level on which significants discrepancies with the PS model become clearly noticiable. The N-body simulations showed that this model overestimated the abundance of low mass halos and underestimates the abundance of the haloes in the high mass-tail (see Figure 6.1 taken from Jenkins et al. (2001) and Warren et al. (2006) paper).

There is a great effort to deal with previous mentioned drawbacks and more accurate formulae for the mass function of halos have been constructed using simulations. However the identification of the halo and the determination of its mass it is not trivial and various methods for this are applied (White (2001),White (2002), Luki et al. (2007))

6.3.1 Measures of Halo Mass

There are two common algorithms to find halos in simulations. The spherical overdensity algorithm (Lacey and Cole (1994)) is based in identifying overdense regions above a certain threshold, ρ_t. The threshold can be set with respect to the critical density ρ_c or the background matter density $\bar{\rho}_m$.

The mass M_Δ of the halo is defined as the mass enclosed in a sphere of radius R_Δ whose mean density is Δ times the threshold density, $\Delta\rho_t = \frac{3M_\Delta}{4\pi R_\Delta^3}$. The value of Δ is the overdensity within a sphere of radius R_Δ with respect to ρ_t, which it is typically chosen to be either the critical or background at the epoch of analysis

$$\Delta = \frac{3M_\Delta}{4\pi R_\Delta^3 \rho_t} \tag{6.24}$$

Common values for Δ range from 100 to 500. The disadvantage of defining a halo in this manner is that sphericity of halos is implied, an assumption which may be easily violated (Luki et al. (2007)).

The other method, the Friend-of-Friend (FOF) halo finder(Davis et al. (1985)) is based on the percolation algorithm defining dark matter particles to belong to a FoF group if they are separated by a distance smaller or equivalent to a linking length, b, of any other particle in the group. The FOF algorithm leads to halos with arbitrary shapes since no prior symmetry assumptions have been made. The halo mass is defined simply as the sum of particles which are members of the halo. While this definition is easy to apply to simulations, the connection to observations is di cult to directly establish. For a discussion of the different mass definitions see White (2001) paper.

6.3.2 Fitting Functions

Sheth and Tormen (1999) refined the extended PS mass function to give an improved analytical fit to results of GIF/Virgo simulations. They derive a parameterization of the mass function in terms of the dimensionless mass coordinate ν

$$\nu = \left(\frac{\delta_c}{\sigma(M)}\right)^2 \tag{6.25}$$

and obtain,

$$\frac{dn}{dM} = \frac{\bar{\rho}_m}{M} f(\nu) \frac{d\nu}{dM} \tag{6.26}$$

$$\nu f(\nu) = A(p)\Big(1 + (q\nu)^{-p}\Big)\left(\sqrt{\frac{q\nu}{2\pi}}\right) exp\Big(-\frac{q\nu}{2}\Big) \tag{6.27}$$

where $f(\nu)$ is the multiplicity function or the fraction of mass in collapsed object. A is determinate from $\int f(\nu)d\nu = 1$ to conserve the mass, giving

$$A = A(p) = \left[1 + \frac{2^{-p}\Gamma(1/2 - p)}{\overline{\pi}}\right]^{-1} \tag{6.28}$$

and $q \approx 0.75$ and $p \approx 0.3$ are their best fits. The extended PS formalism has the same form if $q = 1$, $p = 0$ and $A = 1/2$.

Later, Sheth et al. (2001) show that the shape of mass function given by Equation 6.27 is a plausible consequence of extending the excursion set approach to include the elliptical collapse model (Peebles (1980)). In this model the barrier height is not constant and depends on mass of the collapsing overdensity. This leads to a excursion set approach with a moving barrier that generates a first crossing distribution as Equation 6.27.

Jenkins et al. (2001) showed that the halo abundance is well described by a single functional form

$$\frac{dn(M,z)}{dM} = f(\sigma, z)\frac{\bar{\rho}_m}{M}\frac{dln[\sigma^{-1}]}{dM} \tag{6.29}$$

where $f(\sigma, z)$ is the mass fraction of collapsed object expressed in terms of $ln\sigma^{-1}(M, z)$ instead of the mass M and defined by

$$f(\sigma, z) \equiv \frac{M}{\bar{\rho}_m} \frac{dn(M, z)}{dln\sigma^{-1}} \tag{6.30}$$

All dependence on cosmological parameters is in $\sigma(M, z)$. When it is rescaled in this way the mass fraction is said to be universal. This means that results from all output times in simulations trace out the same $f(\sigma)$ curve and it does not depend on power spectrum and cosmological parameters.

They found a single formula that fits all mass functions of the Virgo simulations with an accuracy of 20% for $-1.2 \leq ln\sigma^{-1} \leq 1$

$$f(\sigma) = 0.315exp(-\ ln\sigma^{-1} + 0.61\ ^{3.8}) \tag{6.31}$$

Jenkins et al. (2001) conclude that the fitting function proposed by Sheth and Tormen (1999) is a very good fit to the universal mass function they found, and is close to the best fit they give as Equation 6.31. This is shown in Figure 6.2, which is taken from Zentner (2007). It compares the extended PS model for the fraction of mass in collapsed object with the results of a suite of cosmological numerical simulations.

Tinker et al. (2008) provide a fitting function that predict the halo mass function for spherical aperture mass defined with an arbitrary overdensity Δ respect to the mean density of the Universe $\bar{\rho}_m$ over a wide range of values. They choose the functional form given by 6.29 where the function $f(\sigma)$ is parametrized as

$$f(\sigma) = A\left[\left(\frac{\sigma}{b}\right)^{-a} + 1\right] exp\Big(\frac{-c}{\sigma^2}\Big) \tag{6.32}$$

The parameters A, a, b and c are constants calibrated in simulations. The best fit values of these parameters as a function of Δ were determining by fitting Equation 6.32 to z=0 simulations using χ^2 minimization.

Figure shows the function $f(\sigma)$ measured for simulations at $z = 0$ and $z = 1.25$ with $\Delta = 200$. The residuals of the measured mass function with respect to the best fit at $z = 0$ demonstrates that the mass function is not universal in redshift.

They provide redshift corrections to match mass function to simulations. Figure 6.4 shows the redshift evolution of the $\Delta = 200$ mass function at four redshifts. The solid curves shows a model in which the three first parameter of $f(\sigma)$ are allowed to vary as a power law of redshift

$$A(z) = A_0(1 + z)^{-0.14} \tag{6.33}$$

$$a(z) = a_0(1 + z)^{-0.06} \tag{6.34}$$

$$b(z) = b_0(1 + z)^{-\alpha} \tag{6.35}$$

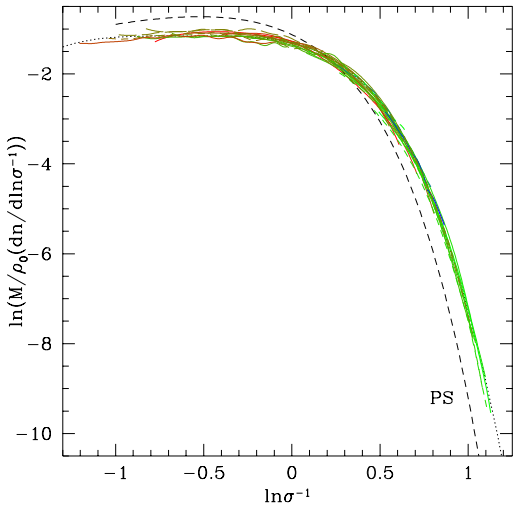

Figure 6.1: Comparison of analytic models of the halo mass function plotted in redshift independent form with results in N-body simulations (Jenkins et al. (2001)). Dashed line is the Press-Schechter mass function and the dotted line is the Jenkins fitting formula that fits all the mass function.

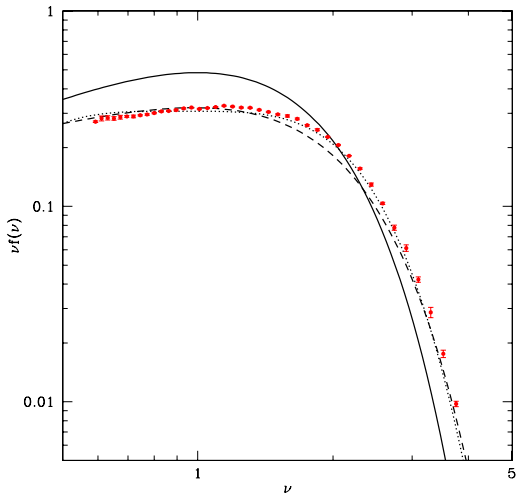

Figure 6.2: Collapsed mass fractions from Zentner (2007). The solid line represents the PS extended approach predictions. The dashed and dotted lines represent the improved fits of Sheth and Tormen (1999) and Jenkins et al. (2001) respectively. The red points are the numerical data from a suite of N-body simulations

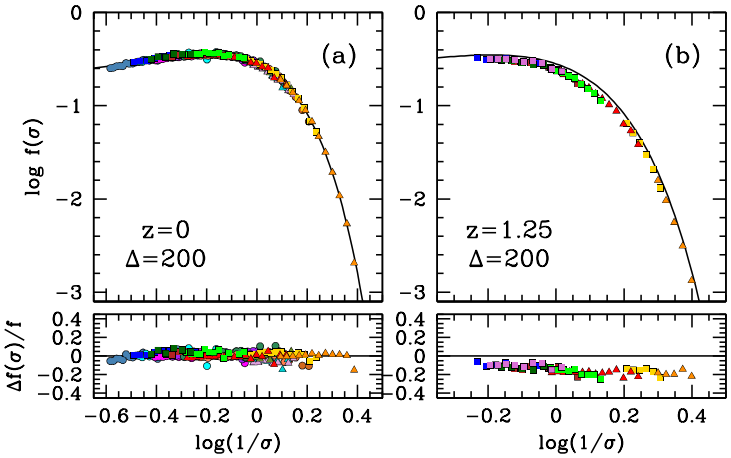

Figure 6.3: (From Tinker et al. (2008)). The solid line for both panels is the best fit function of Equation 6.32 calibrated at $z = 0$. Left: The measured $f(\sigma, z)$ from all simulations for $z = 0$ and for $\Delta = 200$. Right: The measured $f(\sigma, z)$ at $z = 1.25$ and $\Delta = 200$. They restrict to simulations for which they have previous redshift outputs. The lower window shows that the $z = 1.25$ mass function is offset by $\sim 20\%$ with respect to the results at $z = 0$.

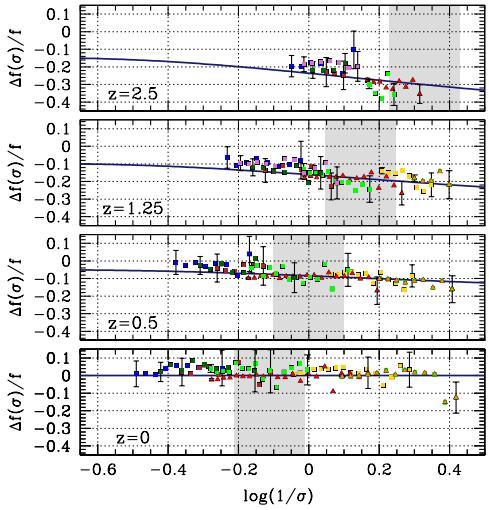

Figure 6.4: (From Tinker et al. (2008)). Redshift evolution of the $\Delta = 200$ mass function. Each panel shows the residuals of the z=0 mass function with respect to the measured mass function at $z = 0$, 0.5, 1.25 and 2.5. The solid curves represent the $z = 0$ mass function modified by Equations 6.33, 6.34 and 6.35.

$$log\alpha(\Delta) = -\left(\frac{0.75}{log(\Delta/75)}\right)^{1.2} \tag{6.36}$$

where subcript 0' indicates the value obtained at z=0 listed in Table 6.1. These are the best fits parameters of Equation 6.32 resulting from fits to many simulations for 9 values of the overdensity Δ (see Table 2 of Tinker et al. (2008) for more details).

Δ	A	a	b	c
200	0.186	1.47	2.57	1.19
300	0.200	1.52	2.25	1.27
400	0.212	1.56	2.05	1.34
600	0.218	1.61	1.87	1.45
800	0.248	1.87	1.59	1.58
1200	0.255	2.13	1.51	1.80
1600	0.260	2.30	1.46	1.97
2400	0.260	2.53	1.44	2.24
3200	0.260	2.66	1.41	2.44

Table 6.1: Mass Function Parameters for $f(\sigma)$ at $z = 0$

As we will see in Section 6.4.2 we will test the redshift evolution of Tinker et al. (2008) mass function model and we also perform a fitting method that correct the deviation from universality in redshift for the Sheth and Tormen (1999) model.

The accuracies of the halo mass function models should, however, be taken with caution. Uncertainties in the halo mass function are not only introduced by the definition of halos in simulations but also by effects due to the baryonic physics, which may cause larger deviations from the mass functions in pure DM simulations than the uncertainty stated above. (e.g., Stanek et al. (2009)).

All the fitting formulas for the halo mass function that we have mentioned before are derivate from N-body simulations of cosmological structure starting from Gaussian initial conditions. Pillepich et al. (2010) explored the behavior of the mass function in the presence of primordial non-Gaussianities.

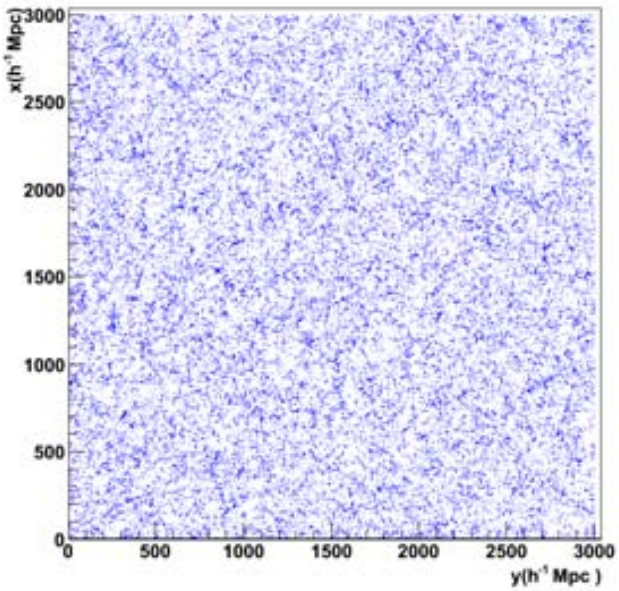

Figure 6.5: Density slice of ΛCDM Hubble Simulation snapshot at z=0. The volume is $3000 \times 3000 \times 100$ $(h^{-1}Mpc)^3$

6.4 Mass Function for Simulations Used in this Work

Massive clusters of galaxies have a very low number density. This is directly related to the exponential decrease of the abundance of dark matter halos with mass as described by the models. For this reason we need considerably large volumes to derive statistically meaningful results.

In this thesis, first we have used the z=0 snapshot from at ΛCDM Hubble Volume N-body simulations (hereafter HVS)(Jenkins et al. (2001)) that was run in a comoving box with side $L = 3000h^{-1}Mpc$. This large volume simulation ($V = L^3 = 27h^{-3}Gpc^3$) is particularly well suited to study the statistical properties of very massive structures like the distribution of galaxy cluster. It contains 10^9 particles with a mass of $2.25 \times 10^{12}h^{-1}M_{\odot}$. This means that mass and spatial resolution of this simulation are insu cient for studying galaxies. Dark matter halos are identified with a FOF algorithm with a linking length $b = 0.164$. Figure 6.5 shows a slice of the snapshot which is given directly in comoving coordinates.

In addition to the simulation output, we have used the DES v1.02 halo mock catalog light cone sky survey based on the Hubble Volume PO light cone output (Evrard et al. (2002)). We choose this catalog because it covers the same volume as it is predicted for DES. In this case the halo finder algorithm is the spherical overdensity (SO) where the threshold $\Delta = 200$ is

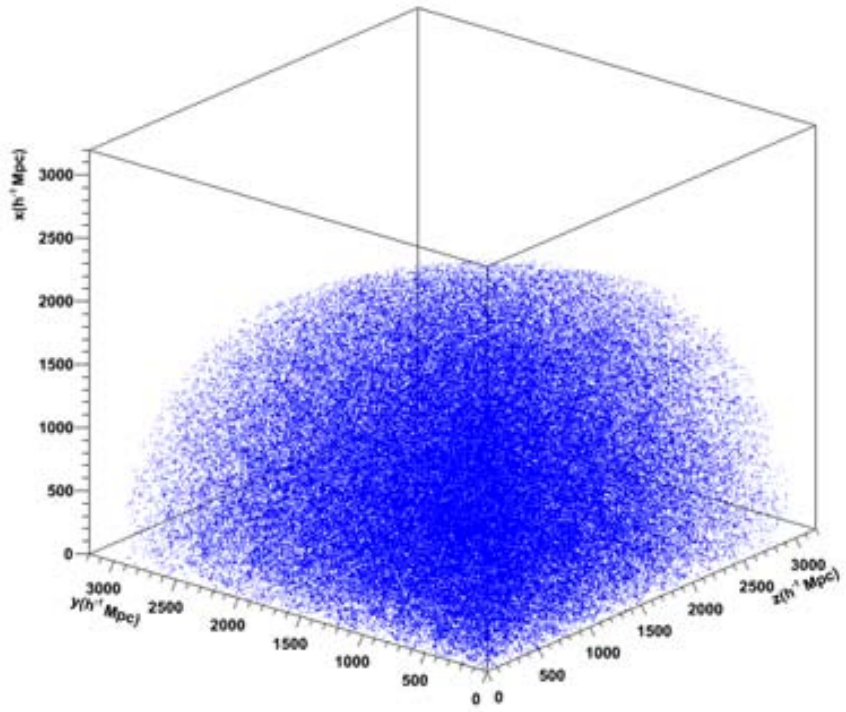

Figure 6.6: ΛCDM Hubble Volume light cone octant of the sky with DES volume. The observer is in the coordinate origin that corresponds to redshift z=0.

set with respect to the critical density $\rho_c(z)$. The value of the mass of the particle is the same as in the snapshot.

The positions of the halos in the light cone are given in angular and redshift coordinates $(RA, DEC; z)$. Figure 6.6 shows these positions after we convert them to cartesian coordinates (x, y, z). Each halo satisfy the parametric equations

$$x = \chi cos(DEC)cos(RA) \tag{6.37}$$

$$y = \chi cos(DEC)sin(RA) \tag{6.38}$$

$$z = \chi sin(DEC) \tag{6.39}$$

where we have converted the measured redshift to a comoving distance χ using Equation 2.36 for which a cosmological model is used. The cosmological parameters used in the simulations are: $\Omega_m = 0.3$, $\Omega_b = 0.04$, $\Omega_\Lambda = 0.7$, $\sigma_8 = 0.9$, $h = 0.7$.

6.4.1 Mass Function Result in the Hubble Volume Snapshot at z=0

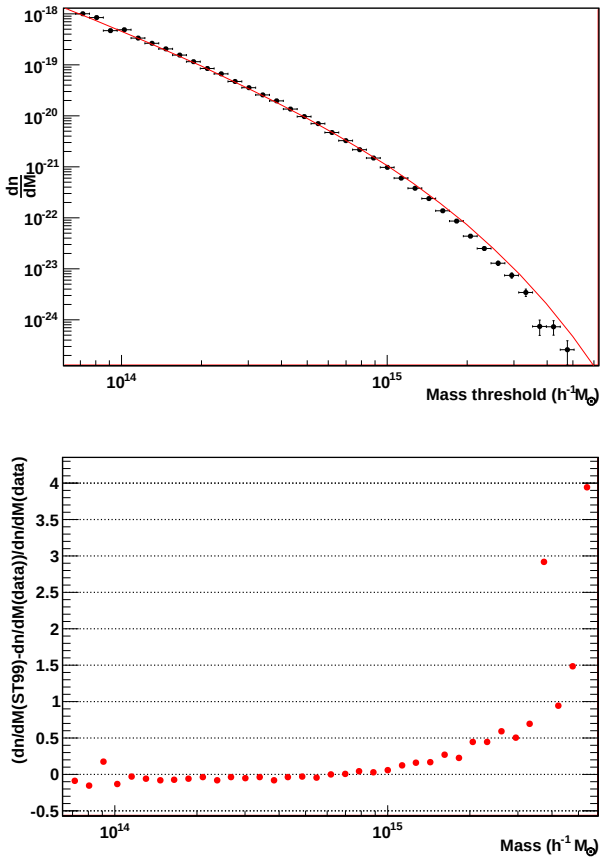

Figure 6.7: Results for HVS snapshot at z=0. Top: Sheth and Tormen (1999) mass function model with p and q fiducial and measurements. Bottom: Residuals of the measured mass function with respect to the Sheth and Tormen (1999) mass function model with p and q fiducial values.

We have measured th z=0 HVS halo mass function by counting the number of halos ΔN within a logarithmic mass bin of width $\Delta lnM = 0.12$

$$\frac{dn}{dM} = \frac{\Delta N}{V \Delta M} \tag{6.40}$$

where V is the volume of the simulation box.

Figure 6.7 shows comparison of the measurements with the Sheth and Tormen (1999) fitting formulae with p and q fiducial values. The vertical bars are the Poisson errors and the horizontal bars the bin width. Although Jenkins et al. (2001) provide a more accurate fitting formula for this simu-

lation we have used this model because it is used to derive the halo biasing formula in our calculations (see Chapter 7).

We find deviations of less than 1% in the mass range $10^{14}h^{-1}M_{\odot} \leq M \leq 7 \times 10^{14}h^{-1}M_{\odot}$ and an overprediction for $M \geq 7 \times 10^{14}h{-}1M_{\odot}$ which increases with mass. These results are in agreement with the Sheth & Thormen model comparison studied in Jenkins et al. (2001). We conclude that the value of the mass function is well matched by the Sheth and Tormen (1999) model. Small discrepancies are found in the low mass tail and they are greater in the highest mass bins where the number of halos is very small. There are less than 100 halos in the last six bins and one for the last. However, if we compare the systematic error with the statistic error, the deviations in the high mass tail are not significant.

Moreover, since the mass function sets the weight for the different mass regimes in the integral to obtain the bias, in the high mass tail the deviations we have found won't be significant for the bias results.

6.4.2 Mass Function in DES Light Cone Simulations

The mass function in the light cone is measured as in the previous section but now N is the number of halos in the redshift dependent comoving volume V. The volume element is given by

$$dV = \chi^2 d\chi d\Omega = \frac{\chi^2(z)}{H(z)} dz d\Omega \tag{6.41}$$

where χ is the comoving distance to redshift z and $d\Omega$ is the solid angle. The volume in the redshift bin $[z_1, z_2]$ is obtained through

$$V = \int_{\Omega} d\Omega \int_{z_1}^{z_2} \frac{\chi^2(z)}{H(z)} dz \tag{6.42}$$

The light cone has ~ 247700 halos in a total volume of $1.42 \times 10^{10}h^{-3}Mpc^3$. We divide it in redshift bins of width 0.2 where the volumes are calculated using Equation 6.42. The results are given in Table 6.2.

z bin	Volume $h^{-3}Mpc^3$
$0.2 - 0.4$	5.74×10^8
$0.4 - 0.6$	1.26×10^9
$0.6 - 0.8$	1.96×10^9
$0.8 - 1$	2.59×10^9
$1 - 1.2$	3.10×10^9
$1.2 - 1.4$	3.49×10^9

Table 6.2: Calculated volumes for redshift bins

First we compare the mass function measured for every redshift bin with the Sheth and Tormen (1999) model with the p and q fiducial values evaluated at the mean redshift. Figure 6.8 shows that there is a high disagreement in all the mass range. Therefore we fit the parametric model to the halo catalog measurements where we assume Poisson counts. Our fitting method consist in a simple χ^2 of the difference between the theoretical model and the measured counts in bins (e.g., Jenkins et al. (2001) and Manera and Gaztañaga (2011)). Table 6.3 shows the best p and q parameters which we have found fitting over all the mass range of the simulations for every redshift.

z	p	q
0.3	0.35	0.88
0.5	0.33	0.87
0.7	0.33	0.85
0.9	0.33	0.84
1.1	0.33	0.84
1.3	0.33	0.85

Table 6.3: Best fit values of the Sheth and Tormen (1999) p and q parameters to the simulation mass function

We also test the Tinker et al. (2008) fitting function and their redshift evolution. As we explained in Section 6.3.2 they provide mass function parameters for each Δ value respect to the mean density of the Universe, $\bar{\rho}_m$. However, the halo finder algorithm in the light cone define spherical regions that are overdense with respect to the critical density $\rho_c(z)$ where the mass is given by

$$M_\Delta = \frac{4\pi}{3}\Delta\rho_c R_\Delta^3 = \frac{4\pi}{3}\frac{\Delta}{\Omega_m(z)}\bar{\rho}_m R_\Delta^3 \tag{6.43}$$

So if we define a overdensity contrast as

$$\Delta' = \frac{\Delta}{\Omega_m(z)} \tag{6.44}$$

we can use the Tinker et al. (2008) functional form for any value of Δ' (Penna (2010)). We calculate the parameters that evolve with redshift using Equations 6.33, 6.34, 6.35 and 6.36, where

$$log\alpha(\Delta') = -\left(\frac{0.75}{log(\Delta'/75)}\right)^{1.2} \tag{6.45}$$

and the values of the parameters at $z = 0$ are calculated by spline interpolation of the parameters as a function of Δ'. Figure 6.9 shows the results of the measured mass function for 6 redshift bins and the Tinker et al. (2008) model.

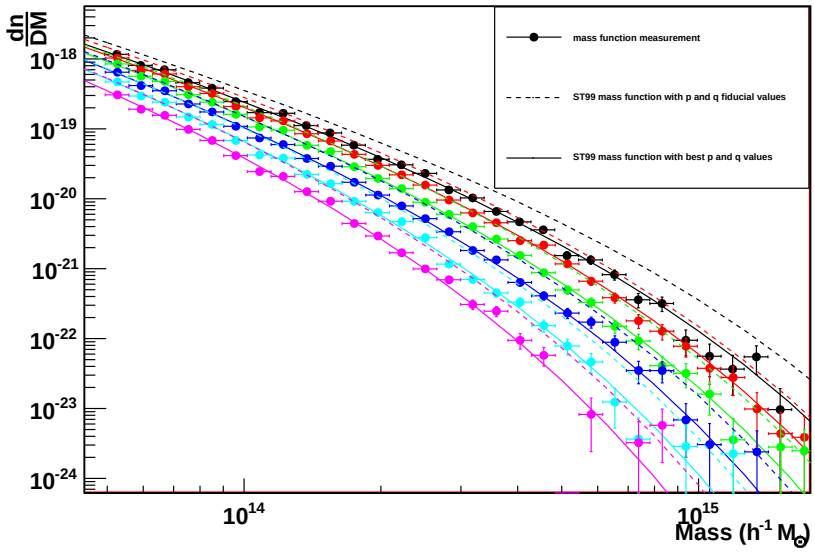

Figure 6.8: Points are mass function in DES light cone simulations for 6 redshift bins measurements, $z = 0.2-0.4$, $0.4-0.6$, $0.6-0.8$, $0.8-1$,$1-1.2$, $1.2-1.4$) (black, red, green, blue, light blue and magenta respectively). Solid lines are the Sheth and Tormen (1999) mass function fits with the best p and q. Dashed lines are the mass functions with the p and q fiducial values.

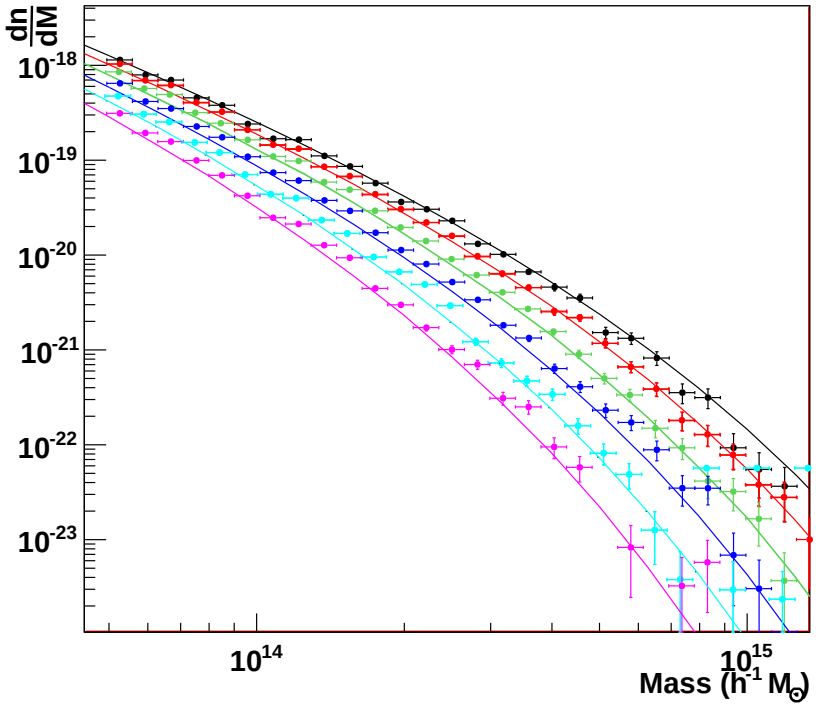

Figure 6.9: Tinker et al. (2008) fitting function comparison with the DES light cone measurements (points) for 6 redshift bins. The color code of the redshift bins are the same as previous figure.

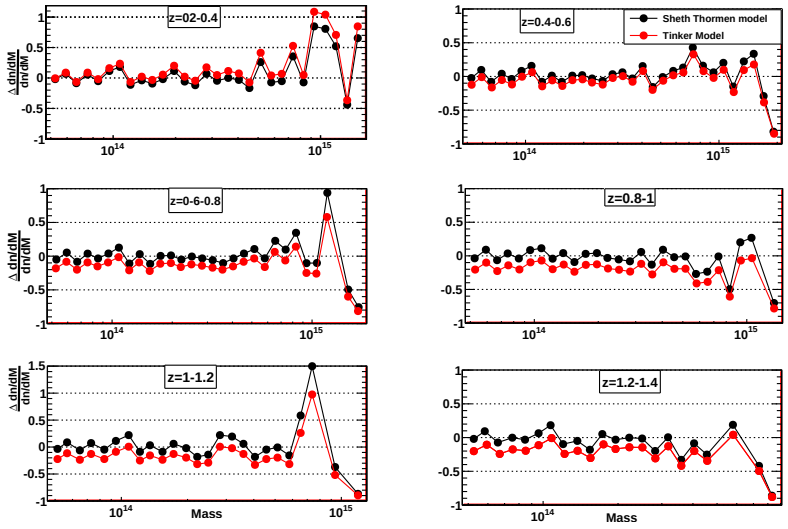

Figure 6.10: Ratio between the measured halo mass function for six redshift bins from the light cone simulation with the fitting functions. Black dots are the values of the Sheth and Tormen (1999) model with the best p and q parameters and red dots the Tinker et al. (2008) model. Note that the mass units are $M_{\odot}h^{-1}$

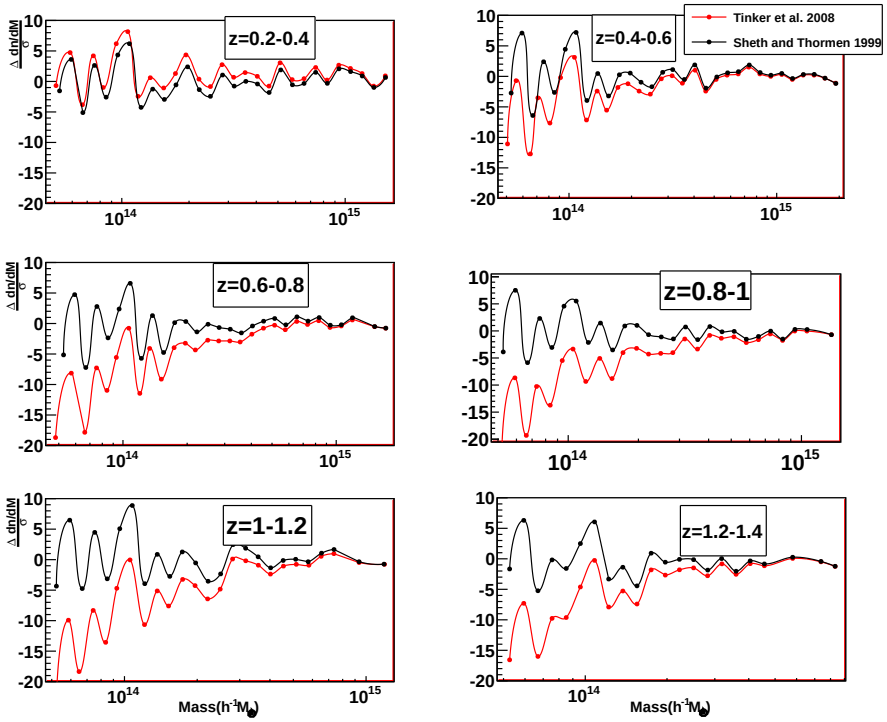

Figure 6.11: Systematic error $\Delta\frac{dn}{dM}$ compared to the statistical error σ for the previous redshift bins. Black dots are the values with Sheth and Tormen (1999) model with the best p and q parameters and red dots the Tinker et al. (2008) model.

In Figure 6.10 we compare the Sheth and Tormen (1999) mass function with the Tinker et al. (2008) mass function. It shows the ratios of the measured mass function to the fitting functions. In all the redshift bins we found that the deviations increase on the high mass tail for both models where the number of halos is rather small. In Figure 6.11 we compare the systematic error $\Delta\frac{dn}{dM}$ with the statistical error σ. These results show that these high deviations are not significant. Moreover, these deviations also won't be significant for the bias results.

The results also show that disagreement between models increase with redshift. We obtain approximately the same accuracy in all the bins with Sheth and Tormen (1999) model. However, we found that the deviations increase with redshift with Tinker et al. (2008) fitting function. Although at $z = 0.2 - 0.4$ both models agree, at $z \geq 0.4$ the last model underpredicts the measurements.

Our conclusion is that we found better results in the redshift evolution with the Sheth and Tormen (1999) mass function.

Chapter 7

Halo Bias and Clustering

Abstract: We study the accuracy of the model predictions of dark matter halo bias by comparing them with results from numerical simulation of non linear gravitational clustering.

7.1 Halo Bias

7.1.1 Introduction

It is now well established that dark matter halos are biased tracers of the underlying dark matter distribution. The literature contains different usages of the bias parameter, which are not equivalent to one another and we must always have careful with which is being used.

The simplest definition of the bias is given by Eq. 5.37 used to normalized the power spectrum of the galaxies. However, in this section we describe theoretical approaches designed to determine the linear halo dark matter bias, without galaxy formation process.

In our first definition, the uctuations of the number density δ_h of halos with mass, M can be written as a bias factor $b(M)$ multiplied by the uctuations of the underlying matter density δ_m.

$$\delta_h(\bar{x}, M) = b(M)\delta_m(\bar{x}) \tag{7.1}$$

The determination of halo bias is closely related to the description of halo abundance. They are not independent: an accurate model of halo clustering is part and parcel of an accurate model of halo abundances. As we describe below, two theoretical description of the halo abundance and distribution of halos with respect to dark matter have been designed: the theory of peaks (Kaiser (1984); Bardeen et al. (1986)) and the excursion set approach (Bond et al. (1991)).

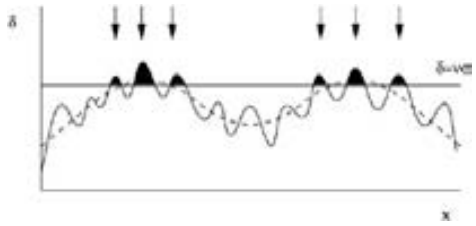

Figure 7.1: The high peak bias model.

The second definition refers to the relative size of the halo and matter correlation functions. The halo correlations are amplified as

$$\xi_{hh}(\bar{r}, M) = b^2(M)\xi(\bar{r}, M) \tag{7.2}$$

The bias depends on the mass of the halo, M (and the redshift as we will see). Moreover, this factor in general depends on the scale. However, it may well be adequately represent by a constant across some range of scales as long as we look to large enough scales which in practice more o less means scales in the linear regime (Liddle and Lyth (2000)). The bias for the non linear regime would be scale dependent.

7.1.2 Linear Bias from Peak Background Split

The peak background split (Kaiser (1984); Bardeen et al. (1986); Cole and Kaiser (1989)) applied on large scales shows how the local number of halos depends on the environment. In the context of clustering of peaks, the central idea it is to image an overdensity field δ that can be decomposed into a short wavelength δ_s and into a long wavelength background δ_b such that

$$\delta = \delta_s + \delta_b \tag{7.3}$$

The long wavelength mode modulates the number counts of the short wavelengths modes (peaks). The effect of this is to perturb the threshold required for a peak to collapse

$$\tilde{\delta}_c = \delta_c - \delta_b \tag{7.4}$$

The background reduces (or enhances) the threshold and then is more (or less) probable to find more collapsed objects where $\tilde{\delta}_c$ is large (small or ≤ 0) than in regions with low (high) background overdensities (Kaiser (1984)). The uctuations of a given strength collapse at different places at slightly different times. This causes the local number density to vary from place to place depending of δ_b.

The number density is therefore modulated. Since $\delta_b << 1$ at large scale, we can expand the mass function dn/dM

$$\frac{dn}{dM}(M) = \frac{d\bar{n}}{dM}(M) + \frac{d^2\bar{n}}{dMd\nu}\frac{d\nu}{d\delta_b}\delta_b + ... \tag{7.5}$$

If the mass function is given by PS, then

$$\frac{dn}{dM}(M) = \frac{d\bar{n}}{dM}(M)\left[1 + \frac{\nu^2 - 1}{\sigma\nu}\delta_b\right] \tag{7.6}$$

This gives a bias in the number density of halos in Lagrangian space, in which particles have fixed coordinates all time.

$$\delta_h^L(M) = \frac{\frac{dn}{dM} - \frac{d\bar{n}}{dM}}{\frac{d\bar{n}}{dM}} = \frac{\nu^2 - 1}{\sigma\nu}\delta_b \tag{7.7}$$

where the Lagrangian bias is

$$b_L(\nu) = \frac{\nu^2 - 1}{\sigma\nu} = \frac{\nu^2 - 1}{\delta_c} \tag{7.8}$$

The discussion above is not rigorous, because it is di cult to separate the background and the peak fields. However, it is useful to know that the higher the large wavelength plateaus of a random field, the higher the peak number density in these regions.

7.1.3 Linear Bias from Excursion Set Approach

Here we will see how Mo and White (1996) calculate the bias by using the extended PS formalism.

A key step to determine the halo bias is the conditional mass function which we want to define. First, Bond et al. (1991) derived the merger probability of masses, collapsed and virialized by an earlier moment, to be included now in larger masses. The fraction of the mass of a halo of initial radius R_0 , variance σ_0^2 and linear overdensity δ_0 which at redshift $z_1 < z_0$ was in subhaloes of mass M_1, variance σ_1^2 and extrapolated linear overdensity limit δ_1, is

$$f(\sigma_1, \delta_1\ \sigma_0, \delta_0)\frac{d\sigma_1^2}{dM_1}dM_1 = \frac{1}{\sqrt{2\pi}}\frac{\delta_1 - \delta_0}{(\sigma_1^2 - \sigma_0^2)^{3/2}} exp\left[-\frac{(\delta_1 - \delta_0)^2}{2(\sigma_1^2 - \sigma_0^2)}\right]\frac{d\sigma_1^2}{dM_1}dM_1 \tag{7.9}$$

which it is described by a similar Brownian walk with two absorbing barriers (Martinez and Saar (2002)).

Later, Mo and White (1996) used this relation to predict the halo bias and the enhancement of spatial correlations. The conditional mass function is the average number of halos of mass M_1 which collapsed at z_1 in a spherical region with comoving radius R_0, volume V_0 and mass M_0

$$N(M_1, z_1\ M_0, V, z_0) = \frac{M_0}{M_1}f(\sigma_1, \delta_1\ \sigma_0, \delta_0)\frac{d\sigma_1^2}{dM_1}dM_1 \tag{7.10}$$

This gives the overdensity of M_1 halos in M_0:

$$\delta_h(M_1, z_1\ M_0, V_0, z_0) = \frac{N(M_1, z_1\ M_0, V_0, z_0)}{(dn/dM_1)V_0} - 1 \tag{7.11}$$

where dn/dM_1 is the standard PS mass function (unconditional mass function) given by Equation 6.23 for a critical density required for collapse at z_1: $\delta_c(z_1) = \delta_1$ (Martinez and Saar (2002)).

This relation provides a relation between the overdensity of the halo distribution and that of the matter distribution. The halo bias is explored comparing the abundance of halos in this cell of size V_0 with the overall abundance given by dn/dM_1.

In the large cell limit R_0 , $\sigma_0 << \sigma_1$ and $\delta_0 << \delta_1$, the last equation is

$$\delta_h(M_1, z_1\ M_0, V_0, z_0) = b_h^L \delta_0 = \frac{\nu_1 - 1}{\delta_1}\delta_0 \tag{7.12}$$

where the Lagrangian bias b_h^L only depends of the mass of collapsed halos and the redshift at which halos are observed. It also coincides with the result of previous section (Equation 7.8).

7.1.3.1 Dynamical Evolution of Clustering. Eulerian Bias

The Lagrangian bias is calculated in the initial sphere. To compute the bias relation in the evolved Eulerian space, Mo and White (1996) relate the initial density contrast, δ_0, and radius R_0 to those at the desired redshift z, δ and R using a spherical collapse model.

First, from the mass conservation

$$R_0^3 = R^3(1 + \delta) \tag{7.13}$$

The physical radius R which had initial Lagrangian radius $R0$ is given for $\delta_0 > 0$ by

$$\frac{R(R_0, \delta_0, z)}{R_0} = \frac{3}{10}\frac{1 - cos\theta}{\delta_0} \tag{7.14}$$

and

$$\frac{1}{1+z} = \frac{3 \times 6^{2/3}}{20}\frac{(\theta - sin\theta)^{1/2}}{\delta_0} \tag{7.15}$$

If we assume that $z = 0$ at the time when the clustering haloes is examined, the relation between these two quantities can be approximated by

$$\delta_0 = -1.35(1+\delta)^{-2/3} + 0.78785(1+\delta)^{-0.58661} - 1.12431(1+\delta)^{-1/2} + 1.68647 \tag{7.16}$$

Finally, under the above assumptions the average density of dark haloes in sphere with current radius R and current mass overdensity δ is obtained

from equations 6.23 and 7.10

$$\delta_h(M_1, z_1\ M_0, V_0, z_0) = \frac{N(M_1, z_1\ M_0, V_0, z_0)}{(dn/dM_1(M_1, z_1))V} - 1 \tag{7.17}$$

Where $V = \frac{4\pi R^3}{3} = V_0/(1+\delta_0)$. Then, again for $M_0 >> M1$ and $\delta_0 << \delta 1$, we have

$$\delta_h = \left(1 + \frac{\nu_1^2 - 1}{\sigma\nu_1})\delta \right. \tag{7.18}$$

The resulting bias, referred as to Eulerian bias, is given by

$$b_h^E(\nu_1, z_1) = 1 + b_h^L(\nu_1, z_1) \tag{7.19}$$

This means that the halo uctuations have an unbiased component with respect to the collapsed region (the term +1) while being enhance due to the bias of the collapsed region with respect to the unclasped background (the term b_h^L).

In order to define the biasing and anti-biasing regimes, we shall define a mass M_* by $\delta_1 = \sigma(M_*)$. For larger masses the variance $\sigma^2(M)$ is smaller, so by 7.19 halos with $M_1 > M_*$ are (positively) biased and smaller halos are anti biased.

7.1.4 Linear Bias Improvements

As we saw in Chapter 4, Sheth and Tormen (1999) showed that a simple modification of the PS formula provides a good fit to the unconditional mass function. This allowed to derive a large scale bias relation.

In the large cell limit R_0 , $\sigma_0 << \sigma_1$ and $\delta_0 << \delta_1$, the bias in Lagrangian space is computed as in the last section.

$$\delta_h^L(M_1, z_1\ M_0, V_0, z_0) \approx \left[q\nu_1 - 1 + \frac{2p}{1+(q\nu_1)^p}\right]\frac{\delta_0}{\delta_1} = b_L(M_1, z_1)\delta_0 \tag{7.20}$$

When q=1 and p=0 the mass function has the PS form and this form reduces to the one given by Cole and Kaiser (1989) and Mo and White (1996). The bias in Eulerian space is obtained by subsititing this expression into Equation 7.19

$$b_h^E(\nu_1) = 1 + \frac{q\nu_1 - 1}{\delta_1} + \frac{2p}{\delta_1(1+(q\nu_1)^p} \tag{7.21}$$

Later, Tinker et al. (2010) using high resolution N-body simulations, gives a parameterization of the halo mass bias in terms of six parameters

$$b(\nu) = 1 - A\frac{\nu^a}{\nu^a + \delta_c^a} + B\nu^b + C\nu^c \tag{7.22}$$

where the parameters A, a and C depend on the density contrast Δ.

In Section 7.3.2 we will compare this numerical fits with direct measurements from N-body simulations with a DES volume.

7.1.5 The Distribution of Halos at Large scales: Deterministic Biasing

The linear halo bias formula is only accurate on large scales. To calculate the high order moments of peaks and halos or non linearities, Mo et al. (1997) and Scoccimarro et al. (2001) follows the general formalism developed by Fry and Gaztañaga (1993). The perturbative analysis assume that the halo overdensity is a function of the underlying matter overdensity, $\delta_h = F(\delta_m)$. It can be written as a Taylor expansion

$$\delta_h = \sum_{k=0}^{\infty} \frac{b_k}{k!} \delta^k \tag{7.23}$$

where b_k are constant. The term b_0 is constrained by the condition $\delta_h = 0$. By construction, the remaining coe cients must satisfy

$$\frac{1}{\bar{\rho}} \int dM M \frac{dn}{dM} b_k(M) = \begin{cases} 1 & \text{if } k = 1 \\ 0 & \text{if } k > 1 \end{cases} \tag{7.24}$$

Following discussion of Section 7.1.3, where we compute the linear halo bias in the large cell limit using the mass function of Equation 6.27, Mo et al. (1997) determined the first five bias coe cients, b_0, b_1, b_2, b_3, b_4, where b_1 is just given by Equation 7.21.

On large scales where deterministic biasing is a good approximation, the variance of halo counts in cells is

$$\delta_h(M_1, z_1\ M_0, V_0, z_0)^2 \ = \ \Big(\sum_{k=0}^{\infty} \frac{b_k}{k!} \delta^k\Big)^2 \ \approx b_1^2(M_1, z_1)^2\ \delta^2 \tag{7.25}$$

where it should be a good approximation to replace δ^2 by the linear theory estimation.

On smaller scales, the bias is both non linear and stochastic. A stochastic bias means that the scatter between δ_h and δ is significant. Accurate analytic models for this stochasticity are presented in literature (e.g., Dekel and Lahav (1999) and Manera and Gaztañaga (2011)).

Figure 7.2 taken from Jeong and Komatsu (2009) shows the matter power spectrum from the Millennium Simulation. It shows and example of how the analytical calculation of the third order perturbation theory reproduces the nonlinear matter power spectrum at high redshift up to certain maximum wavenumber, k_{max}. Note they assume that the bias is stochastic.

7.2 The Halo Model

The halo model is a simple attempt to describe the clustering of matter, galaxies and galaxy clusters in the linear and nonlinear regime. The motivation of this model stems from the failure of dark matter models to explain the observed power spectrum and correlation functions of galaxies.

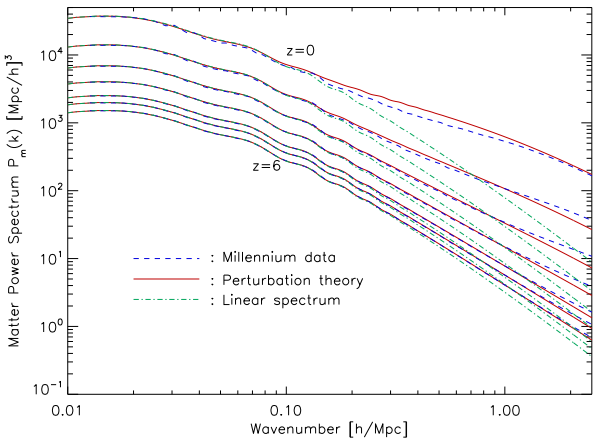

Figure 7.2: (From Jeong and Komatsu (2009)). Matter power spectrum at z = 0, 1, 2, 3, 4, 5, and 6 (from top to bottom) derived from the Millennium Simulation (dashed lines), the third-order perturbation theory (solid curves), and the linear perturbation theory (dot-dashed curves).

First, in this section, we would predict only the dark matter halo distributions. We calculate the halo model non-linear dark matter halo correlation function and their Fourier transform, the power spectrum. In next chapter (see Section 8.1), we will describe the galaxy and galaxy clusters distributions in order to check theory with observations.

The halo model was developed by Scherrer and Bertschinger (1991). They appear to have been the first to write the model for a continuous density field using Fourier space quantities. It allows one to incorporate a realistic halo-halo correlation function into the model (7.2.1). The model has become very popular and there are many literature about it (e.g., Cooray and Sheth (2002a), Seljak (2000) and Peacock and Smith (2000)).

We have formulae for the abundance, and spatial distribution of halos, as well as for the halo profile [1]. Therefore, now we are in position of construct the clustering of dark matter halos.

7.2.1 The Two Point Correlation Function and the Power Spectrum

The calculation of the two point correlation function can be broken into two parts(e.g., Seljak (2000)). The first term describes the case in which the distinct mass elements lie in the same dark matter halo, and the second term is due to mass elements in distinct pairs of halos. Thus the correlation

[1] In Appendix B we will discuss about the profile of dark matter halos

function can be written as

$$\xi(\bar{r} = \bar{x} - \bar{x}') = \xi^{1h}(\bar{x} - \bar{x}') + \xi^{2h}(\bar{x} - \bar{x}') \tag{7.26}$$

where the two terms can be computing by enumerating pairs of infinitesimal mass elements (e.g., Scherrer and Bertschinger (1991)) and require knowledge of how the halo abundance dn/dM and halo density profile u depend on mass (see Appendix B where we discuss about the halo density profile).

In the halo model all the mass is bound up into halos which have a range of masses and density profiles (Cooray and Sheth (2002a)). Therefore, the matter density at a position $\bar{x}$ is expressed as a contribution of the matter density of each halo as

$$\rho(\bar{x}) = \sum_i \rho(\bar{x} - \bar{x}_i\ M_i) \equiv \sum_i M_i u(\bar{x} - \bar{x}_i)\ M_i)$$
$$= \sum_i \int dM d^3x' \delta(M - M_i)\delta^3(\bar{x}' - \bar{x}_i) M u(\bar{x} - \bar{x}'\ M) \tag{7.27}$$

where the sum is done over all haloes. $\delta(M - M_i)\delta^3(\bar{x}' - \bar{x}_i)$ is the number density of haloes with mass M centered at a position $\bar{x}_i$ and u is the normalized profile, which is ρ divided by the total mass contained in the profile $\int d^3u(\bar{x} - \bar{x}'\ M) = 1$.

The halo mass function is given as the ensemble average of the number density of haloes

$$\frac{dn}{dM} = \Big\langle \sum_i \delta(M - M_i)\delta^3(\bar{x}' - \bar{x}_i) \Big\rangle \tag{7.28}$$

Then the mean density is the average of the total density $\rho(\bar{x})$

$$\bar{\rho} = \ \rho(\bar{x})\ = \Big\langle \sum_i M_i u(\bar{x} - \bar{x}_i\ M_i) \Big\rangle =$$
$$\int dM \frac{dn}{dM} M \int d^3x' u(\bar{x} - \bar{x}')\ M) = \int dM \frac{dn}{dM} M \tag{7.29}$$

The one halo term is

$$\xi^{1h}(\bar{x} - \bar{x}') = \frac{1}{\bar{\rho}^2} \int dM M^2 \frac{dn}{dM} \int d^3y u(\bar{y}\ M) u(\bar{y} + \bar{x} - \bar{x}'\ M) \tag{7.30}$$

which is just the convolution of two similar profiles of shapes $u(r\ M)$, weighted by the total number density of pairs contributed by halos of mass M.

The two halo term is given by

$$\xi^{2h}(\bar{x} - \bar{x}') = \frac{1}{\bar{\rho}^2} \int dM_1 M_1 \frac{dn}{dM_1} \int dM_2 M_2 \frac{dn}{dM_2} \times$$
$$\int d^3\bar{x}_1 u(\bar{x} - \bar{x}_1\ M_1) \int d^3\bar{x}_2 u(\bar{x} - \bar{x}_2\ M_2) \xi_{hh}(\bar{x}_1 - \bar{x}_2\ M_1, M_2) \tag{7.31}$$

where $\xi_{hh}(\bar{x} - \bar{x}' \; M_1, M_2)$ is the two point correlation function of halos of mass M_1 and M_2 centered at x_1 and x_2 respectively. If u_1 and u_2 were extremely sharply peaked, then could replace them by delta functions and the integrals over x_1 and x_2 would yield $\xi_{hh}(\bar{x} - \bar{x}' \; M_1, M_2)$.

The most commonly utilized assumption is that on large scales, where biasing is deterministic (see previous section)

$$\xi_{hh}(r \; M_1, M_2) \approx b(M_1)b(M_2)\xi(r) \tag{7.32}$$

In the limit of separations much larger than the sizes of the largest halos the dark matter halo autocorrelation function is determined by the two halo term alone ξ^{2h}. Therefore, on scales larger than the typical halo

$$\xi_{hh}(r) = \xi^{2h} \approx b_h^2 \xi(r) \tag{7.33}$$

where

$$b_h = \frac{\int dM \frac{dn(M,z)}{dM} b(M,z)}{\int \frac{dn(M.z)}{dM} dM} \tag{7.34}$$

Since we are dealing with convolutions of halo profiles, it is much easier to work in Fourier space, where expression become multiplications of the Fourier transform of the halo profiles. Thus, the power spectrum is a sum of one halo and two halo contributions

$$P(k) = P^{1h}(k) + P^{2h}(k) \tag{7.35}$$

where the one halo contribution is

$$P^{1h}(k) = \frac{1}{\bar{\rho}^2} \int dM \frac{dn}{dM} M^2 \; u(k \; M)^{\; 2} \tag{7.36}$$

and the two halo power is

$$P^{2h}(k) = \frac{1}{\bar{\rho}^2} \int dM_1 \frac{dn}{dM_1} M_1 u(k \; M_1) \int dM_2 \frac{dn}{dM_2} M_2 u(k \; M_2) P_{hh}(k \; M_1, M_2) \tag{7.37}$$

where $u(k \; M)$ is the Fourier transform of the dark matter distribution within a halo mass M given by Equation B.5 and $P_{hh}(k \; M_1, M_2)$ is the power spectrum of halos of mass M_1 and M_2. On large scales it can be approximated by

$$P_{hh}(k \; M_1, M_2) \approx b_1(M_1)b_1(M_2)P^{lin}(k) \tag{7.38}$$

The halo model concentrates its efforts in modeling the nonlinear clustering of dark matter with the one halo term. Nevertheless, Crocce and Scoccimarro (2008) showed that the halo model fails to reproduce the observed power spectrum in the nonlinear regime. Moreover, it fails to describe an important distortion to the baryonic acoustic oscillation. Despite these

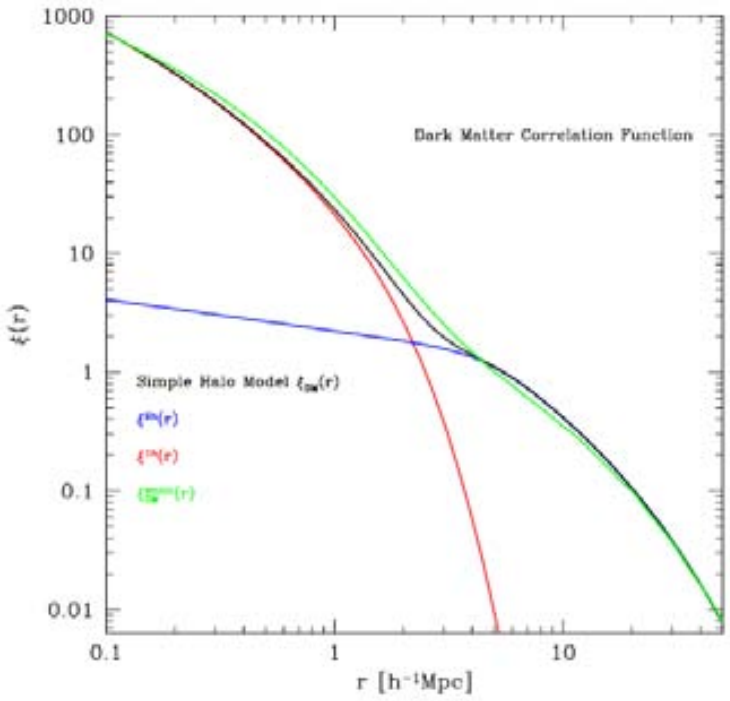

Figure 7.3: Dark matter correlation function computed according to a simple halo model (from Zentner (2005)). The solid black line show the full halo model, red line the one halo contribution, blue line the two halo contribution and green line shows the halo model based fitting formula provided by Smith et al. (2003)

two drawbacks it has still many applications as we discuss in modeling the galaxy and galaxy cluster correlation function for clustering analysis.

In this thesis we will use the halo model based fitting formula provided by Smith et al. (2003) to generate the nonlinear dark matter power spectrum, the so-called Halo-fit model. They use numerical simulations to model the nonlinear evolution of density perturbations that change the shape of the power spectrum. In the Halo-fit model, the power spectrum P_{NL} consist of two terms:

$$\Delta^2_{NL}(k) = \Delta^2_Q(k) + \Delta^2_H(k) \tag{7.39}$$

where $\Delta^2(k)$ is the dimensionless power spectrum given by 5.17. $\Delta^2_Q(k)$ is the quasi-linear term that represents the power generated by the large scale placement of haloes (the two halo term which dominates at large scales) and $\Delta^2_H(k)$ is referred as the one halo term, which is important at small scales.

7.3 Halo Bias and Two Point Correlation Function estimation in N-body Simulations

In this section we want to study the errors that come from the halo model predictions with Sheth and Tormen (1999) and Tinker et al. (2010) prescription to describe the linear bias for halos. In Section 7.3.2 we will compare the halo linear bias measurements in simulations with these predictions.

Since the simulation samples are for halos above a mass threshold, the expected value for the bias predictions for a mass sample $\bar{b}$ is the effective bias given by

$$\bar{b}(M \geq M_{th}, z) = \frac{\int_{M_{th}}^{\infty} dM \frac{dn(M,z)}{dM} b(M,z)}{\int_{M_{th}}^{\infty} \frac{dn(M.z)}{dM} dM} \tag{7.40}$$

On the other hand, we will measure the halo linear bias assuming that on the scales of interest the underlying halo linear bias is deterministic and scale independent

$$\xi_{hh}(\bar{r}) = \bar{b}^2 \xi_m(\bar{r}) \tag{7.41}$$

Once we have measured the two point correlation function $\xi_{hh}(r)$ as we will explain in next section, we will find the halo linear bias by fitting the matter correlation function model $\xi_m(r)$ at a given z to the one estimated with the simulations $\xi_{hh}(r)$ using Equation 7.41. Here the matter correlation function $\xi_m(r)$ is obtained via the Fourier transform of the non linear Halo-fit matter power spectrum calculated using Equation 5.30.

7.3.1 Two Point Halo Correlation Function Estimation

Here we describe how we estimate the two point correlation function $\xi_{hh}(\bar{r})$ for dark matter halos from N-body simulations. We will use the $3000(h^{-1}Mpc)^3$ volume ΛCDM Hubble Volume snapshot at z=0 and then DES halo light cone simulation based on the ΛCDM HV PO light cone described in Chapter 6. Figure 7.4 show a 2D slice of the light cone with volume $3000 \times 3000 \times 200$ $(h^{-1}Mpc)^3$ where the clustering evolution with redshift is observed. The observer is at z=0 that corresponds to the coordinate origin $(0, 0, 0)$.

In both samples, to obtain $\xi(r)$ we will calculate the comoving distance $\bar{r}$ between two objects with coordinates (x_1, x_2, x_3) and (x'_1, x'_2, x'_3) to estimate the correlation function through

$$\bar{r} = \sqrt{(x_1 - x'_1)^2 + (x_2 - x'_2)^2 + (x_3 - x'_3)} \tag{7.42}$$

In order to measure the bias as a function of mass, the former catalog is subdivided in four samples using the following mass thresholds $M \geq 1, 2, 3, 4 \times 10^{14} M_{\odot} h^{-1}$. The result numbers of halos for each sample is given in Table 7.1.

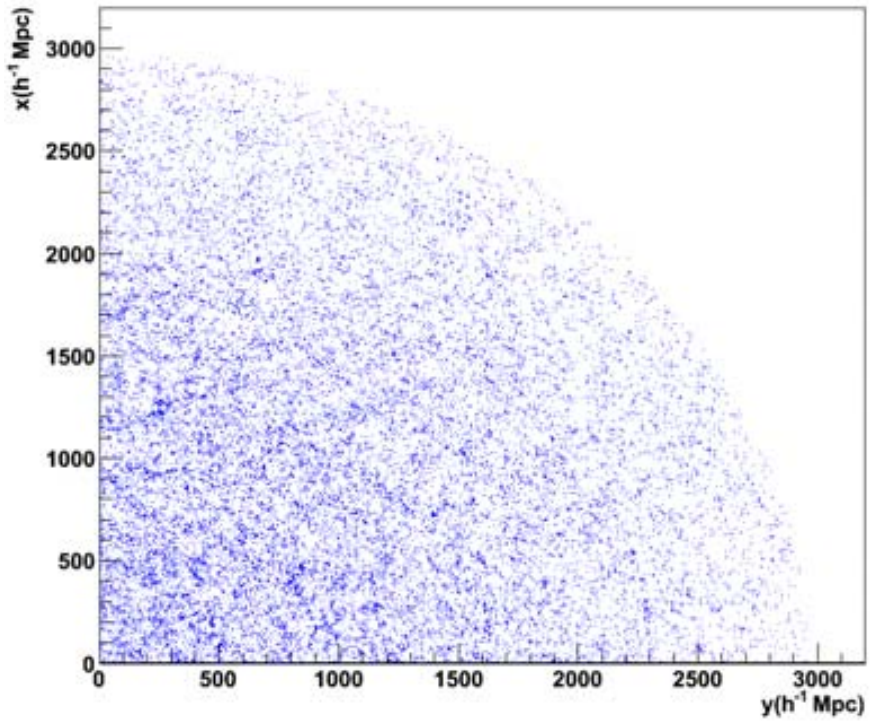

Figure 7.4: 2D light cone profile with volume $3000 \times 3000 \times 200$ $(h^{-1}Mpc)^3$. Here we can see better the clustering evolution with redshift

subsample	N_h
$M \geq 1 \times 10^{14}$	910814
$M \geq 2 \times 10^{14}$	314782
$M \geq 3 \times 10^{14}$	154338
$M \geq 4 \times 10^{14}$	86467

Table 7.1: Number of halos N_h in each subsample created in the HVS snapshot at z=0.

The light cone is divided in 4 samples of mass thresholds $M_{th} \geq 4.95, 6, 8, 10 \times 10^{13} M_{\odot} h^{-1}$ for six redshifts of width 0.2. .

7.3.1.1 Correlation Function Estimator

In practice, the correlation function is estimated simply by counting the number of pairs within volumes around point sources (i.e., galaxies or galaxy clusters) in the sample, and comparing that with the number that would be expected on the basis of a Poisson distributed sample having the same total population. There are subtleties however due to the fact that objects lying near the boundary of the sample volume have their neighbors censored by the bounding volume. In other words, one need a way of dealing with edge corrections.

The common practice is to deal with this by means of an equivalent random catalog with identical geometry to measure the excess of probability. This random catalog is used to calculate the expected number of pairs in the absence of clustering. We achieve this by constructing random catalogs with Monte Carlo Techniques according to the radial and angular distributions of the catalogs under analysis (see next section for more details).

Correlations functions estimators generally count pairs either within the two catalogs or between catalogs, giving a variety of possible estimators for $1 + \xi(r)$ as a ratio of pair counts. In Appendix C we discuss about the different estimators. In this thesis we choose the Landy and Szalay (1993) (LS) estimator that give us the most robust results. It is defined by

$$\xi_{LS}(r) = \frac{DD(r) - 2DR(r) + RR(r)}{RR(r)} \tag{7.43}$$

Here we suppose that the data catalog contains N_D points and the random contains N_R points. Since the random catalogs are denser than the data sample the pair counts are suitably normalized to match the expected pair counts. Therefore the normalized counts are

$$DD(r) = \frac{2P_{DD}(r)}{N_D(N_D - 1)} \tag{7.44}$$

$$RR(r) = \frac{2P_{RR}(r)}{N_R(N_R - 1)} \tag{7.45}$$

$$DR(r) = \frac{P_{DR}(r)}{N_R N_D} \tag{7.46}$$

where $P_{DD}(r)$ represents the clusters pairs in the data separated by a distance $r + \frac{\Delta r}{2}$, $P_{RR}(r)$ is the number of pairs in the same separation bin in the random catalog and $P_{DR}(r)$ is the number of pairs with one member of the pair from the data sample and the other from the random catalog.

The simplest way to compute pair counts is to construct a serial code with a double integral over the catalogs that we are searching pairs. The number of operations required to calculate the correlation function of N number of objects by direct pair counting scales as N^2. Hence, when we have random catalogs constructed denser than the data or we need to repeat the calculation many time to estimate the covariance errors with the jack-knife resampling method (see Section 7.3.1.4), the serial approach becomes computational unfeasible. It is too slow when we compute DD, DR and RR.

Our option is parallelize the code using GPU cores in shared memory machines using OpenMP [2]. We divide the two loops between all available cores to speed up the calculations. Although we reduce the time we still need to improve the code in a future work.

There are many other solutions to compute in a faster way the two point correlation function. Between the solutions are to assign the data field to a density grid (e.g., Barriga and Gaztañaga (2002)), or perform a k-tree code.

7.3.1.2 Creating Random Samples

Generating random samples from the survey volume is an important component of the correlation function. These samples are generated to have not only the same geometry, but also the same selection function as the real sample. In this section we describe how we create the random catalogs for the snapshot and the light cone simulations that we use in this thesis. In this case we don't have to determine the selection function derived from the luminosity function because we treat with dark matter halo simulations. However, for a real catalog, errors in the selection function generate additional errors in the correlation function estimator and, consequently, the selection function must be determinate carefully.

For the ΛCDM Hubble Volume (hereafter HV) snapshot at z=0 we generate a uniform distribution of points with Cartesian coordinates (x, y, z) in a box of side L. We use the algorithm called Mersenne twister (Matsumoto and Nishimira (1998)) for generating uniform pseudorandom numbers available in the software libraries of ROOT [3]. The algorithm provides an extremely long period and it is recommended because of its speed and good random properties.

For the DES light cone simulations we have neither selection effects in the radial (redshift) distribution nor we have to apply the mask in the angular distribution as in real catalog. Figure 7.5 shows the redshift and the angular distributions of the DES light cone cluster catalog.

Although we could generate the random numbers according to the radial

[2] http://www.openmp.org
[3] http://www.root.cern.ch

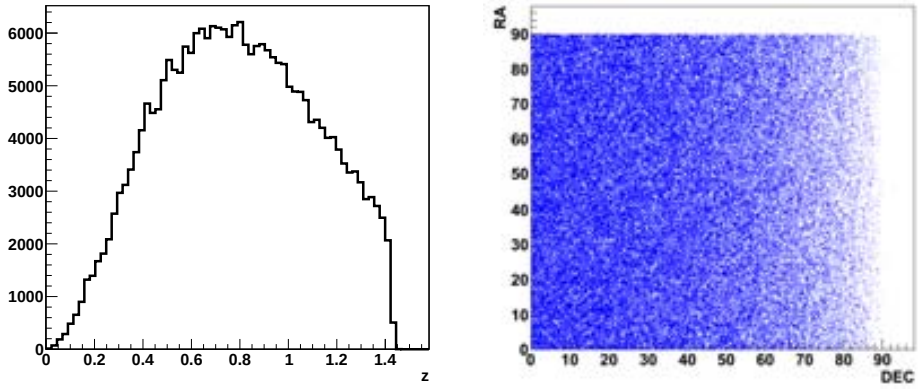

Figure 7.5: Left:Redshift distribution for the DES light cone . N is the number of halos per $\Delta z = 0.02$. Right:DES light cone angular distribution.

and angular distribution without divide the simulation in redshift bins, we prefer divide the sample to proceed in a similar manner that having a real catalog. We randomly sample each redshift and mass bin until we have constructed a random catalog of the desired size.

For each redshift bin of the DES light cone , we generate random numbers according to the declination, right ascension and redshift distributions of the slice.

Since we assume isotropy in the 3D directions, the density is proportional to the solid angle Ω which differential element is $d\Omega = cos(DEC)d(DEC)d(RA)$. Hence we generate a RA and $sin(DEC)$ uniform distributions in the region $(0 < RA < 90,\ 0 < DEC < 90)$.

Finally, the random redshift distribution of the each bin is generated with the acceptance-rejection method (Von Neumann) (Beringer et al. (2012)).

Figure 7.6 shows the resulting redshift distributions for two of the six redshift bins and Figures 7.7 and 7.8 show the results for the angular distributions for the same redshift bins. The distributions of the data and random halos are in good agreement. In these examples the random catalog have the same number of points as the halo catalog, however to minimize the shot noise, we will also create random samples denser than the data sample with the same technique.

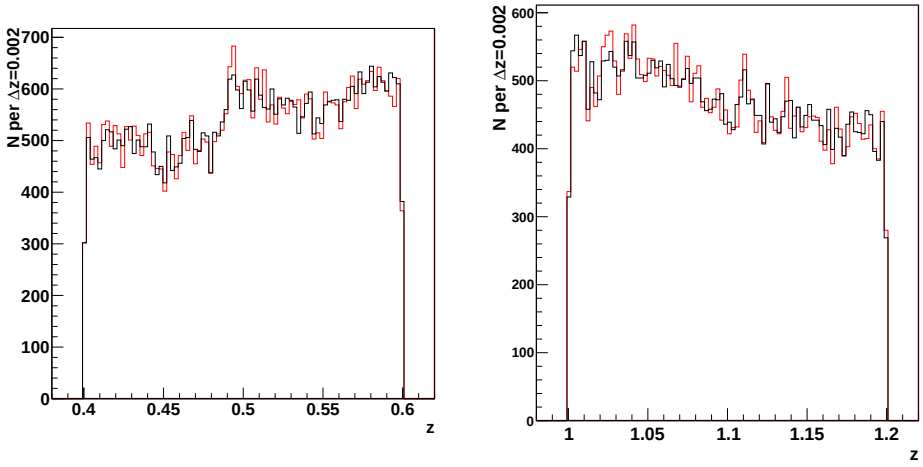

Figure 7.6: Left: light cone z distribution (red line) and Monte Carlo Random generation (black line) for the redshift bin z=0.4-0.6. Right: Light cone z distribution and Monte Carlo Random generation for the redshift bin z=1-1.2

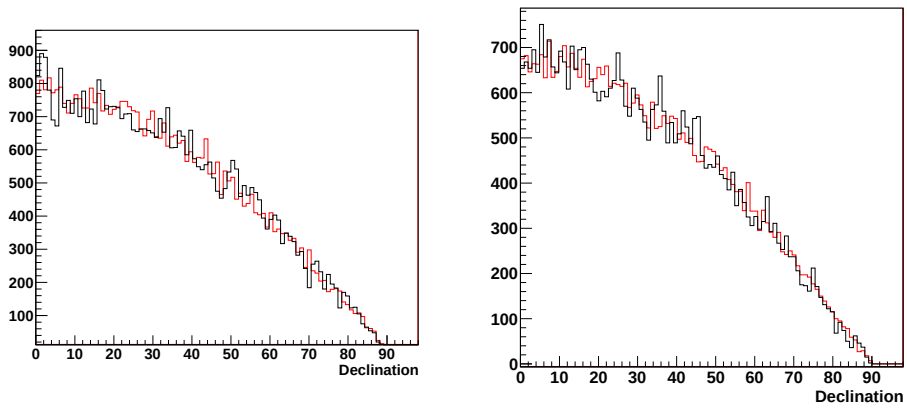

Figure 7.7: Left: Light cone declination distribution (black line) and Monte Carlo Random distribution generation (red line) for the redshift bin z=0.4-0.6. Right: Light cone declination distribution (black line) and Monte Carlo Random distribution generation (red line) for the redshift bin z=1-1.2

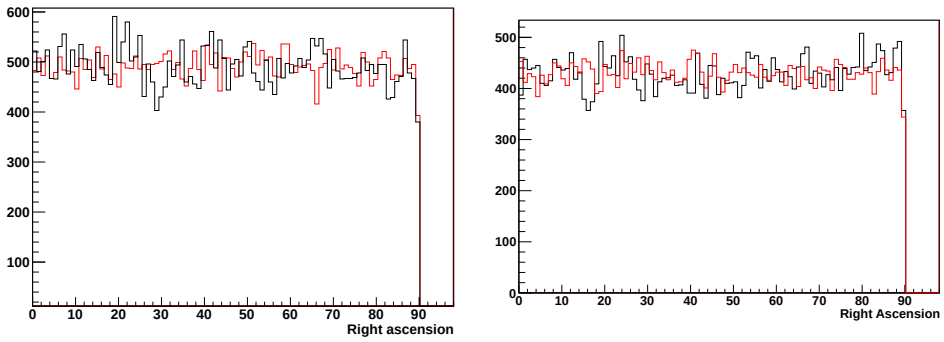

Figure 7.8: Left: Light cone right ascension distribution (black line) and Monte Carlo Random distribution generation (red line) for the redshift bin z=0.4-0.6. Right: Light cone right ascension distribution (black line) and Monte Carlo Random distribution generation (red line) for the redshift bin z=1-1.2

7.3.1.3 Poisson Error Estimation of the Correlation Function

The Poisson errors are derived assuming that the count pairs $DD(r)$ follows a Poisson distribution Peebles (1973). This implies that the standard deviation counts of pairs is just the square root of the count,

$$\sigma_{DD}(rr) = \sqrt{P_{DD}(rr)} \tag{7.47}$$

Similar expressions are valid for P_{DR} and P_{RR}.

To minimize the shot noise, we create random sample denser than the data sample. An approximate expression of the Poisson errors associated with the four estimators is

$$\sigma_{\xi}(r) \quad \frac{1+\xi(r)}{\overline{P_{DD}}} \tag{7.48}$$

where it has been considered that the terms $1/P_{DR}$ and $1/P_{RR}$ vanish when choosing a large enough random sample. However, instead of using the previous approximation, we will estimate the full expression of the effect of standard deviation counts of pairs on the Landy & Szalay correlation function estimator, the propagation of the uncertainty.

Here we will study how the Poisson error of the correlation function estimator is minimized for our scales of interest when we increase the density of the random data. Our samples are the HV snapshot at z=0 and the DES light conecatalogs. Although our goal is to measure the bias at intermediate scales we also studied the errors at large scales for BAO studies.

Figure 7.9 show the measurements of the correlation function $\xi(r)$ for various sizes of the random sample relative to the data sample. It also shows

the shot noise, σ_ξ, and the noise to signal ratio, $\frac{\sigma_{\xi(r)}}{\xi(r)}$. For the first cut in mass, we don't create a random sample denser than the data because it contains 910814 halos. In this case, the Poisson errors are small enough in our scales of interest. For the remaining figures, we use two random samples that contains 910814 and 3×10^6 halos. The results show how the Poisson errors change and how they are minimized for each halo sample. We find that although the error values increase when the number of halos decrease, for each halo sample their values are minimized for the random sample that contains 910814.

Figure 7.10 shows the results for two redshift slices of the light cone when $M_{200} > 4.95 \times 10^{13} h^{-1} M_\odot h$. For each one we create two random samples five and ten times denser than the data and they yield approximately the same Poisson errors. Therefore, we find that the shot noise is minimized when we choose a random sample five times denser.

To summarize we find the following conclusions:

For both catalogs we find that the shot noise $\sigma_{\xi(r)}$ and the noise to signal ratio $\frac{\sigma_{\xi(r)}}{\xi(r)}$ is minimized when we create a random data denser that the data sample. Moreover, the correlation function $\xi(r)$ is smoothed at large scales when the number of random data increase. The improvement is more significant at large scales for BAO studies that at intermediate scales where we estimate the bias. For a given random sample, although the shot noise decreases at large scales, the noise to signal ratio increases and approaches to value 1.

Finally, we also find that for a given mass threshold the Poisson error increases with redshift.

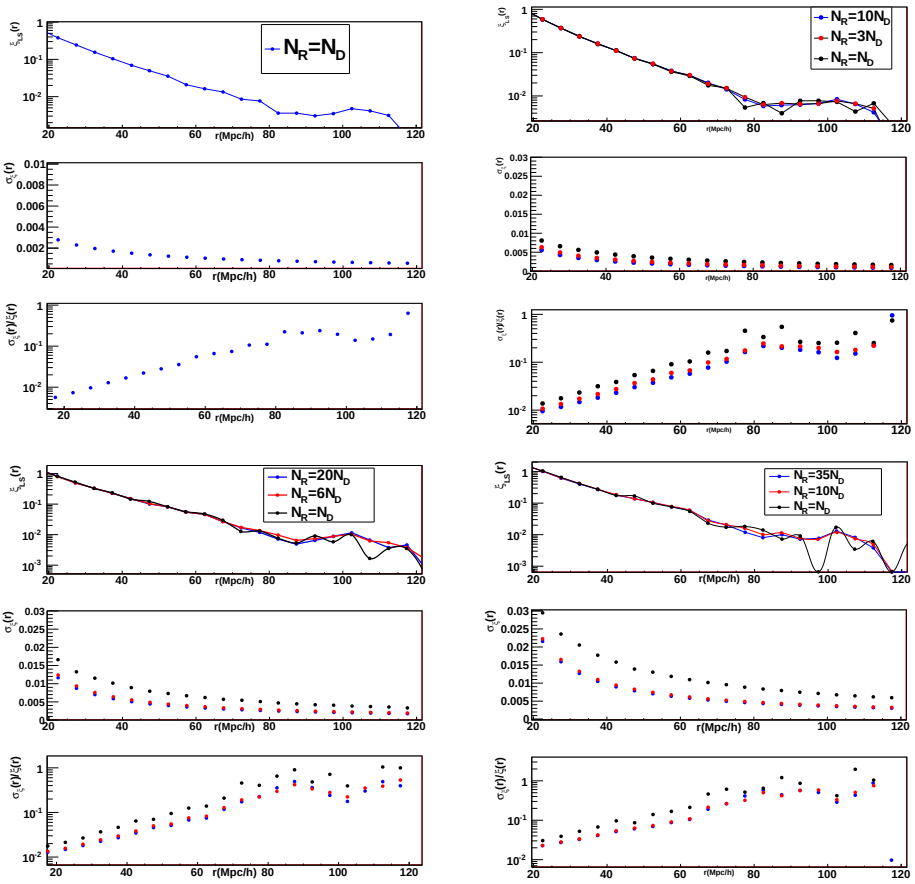

Figure 7.9: Two point correlation function with LS estimator, Poisson error and noise to signal for four mass cuts in the HVS snapshot catalog at z=0. The results are shown in different colors for different sizes of the random samples and the ratio of random to data points are in the legend. Top Left: $\xi(r)$, σ_ξ and $\frac{\sigma_\xi}{\xi(r)}$ when $M_{200} > 1 \times 10^{14} h^{-1} M_\odot$. Here we only use one random sample with the same number of points as the data sample because the Poisson errors are small enough. Top Right:$\xi(r)$, σ_ξ and $\frac{\sigma_\xi}{\xi(r)}$ when $M_{200} > 2 \times 10^{14} h^{-1} M_\odot$. Bottom Left:$\xi(r)$, σ_ξ and $\frac{\sigma_\xi}{\xi(r)}$ when $M_{200} > 3 \times 10^{14} h^{-1} M_\odot$. Bottom right:$\xi(r)$, σ_ξ and $\frac{\sigma_\xi}{\xi(r)}$ when $M_{200} > 4 \times 10^{14} h^{-1} M_\odot$

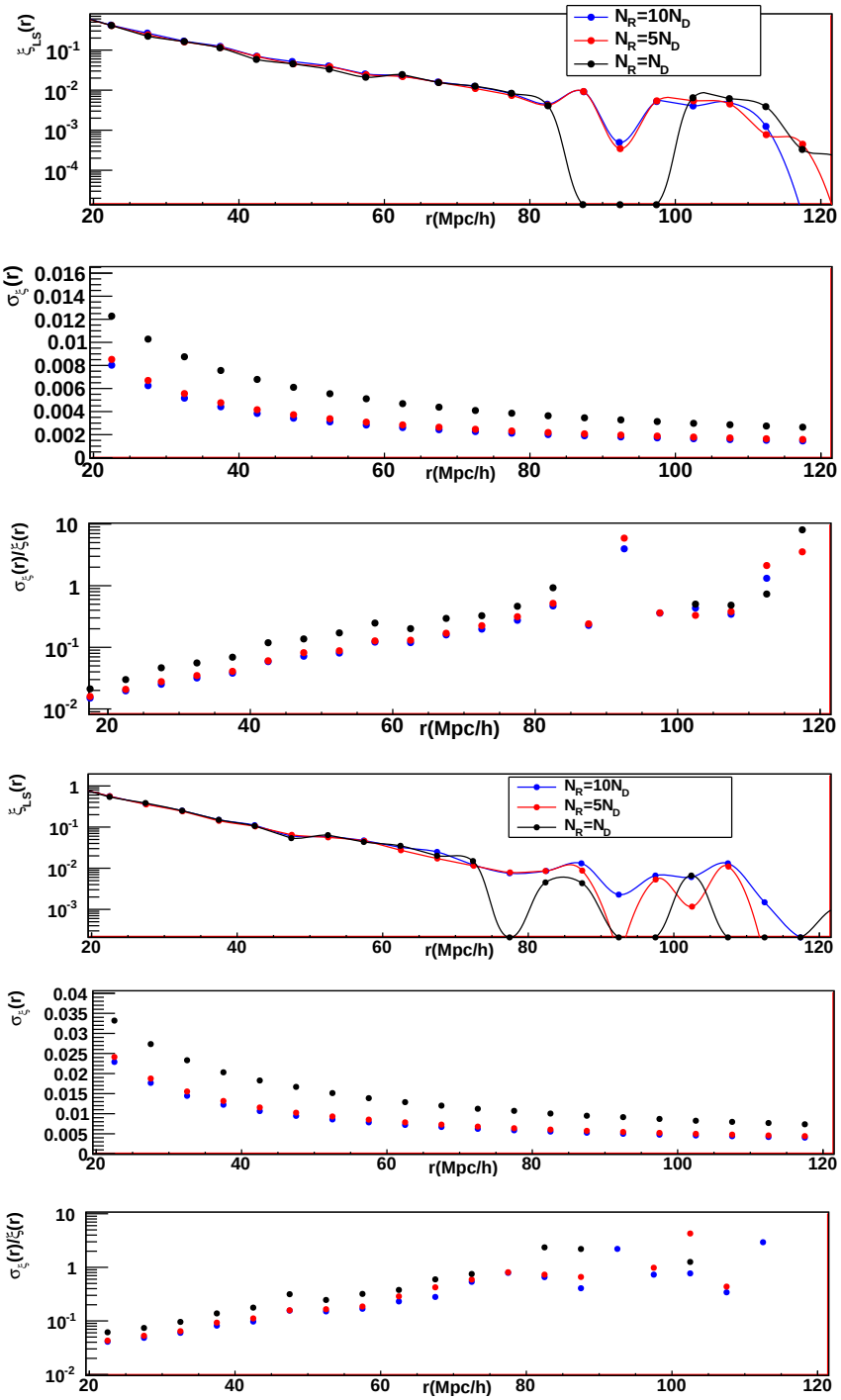

Figure 7.10: Two point correlation function with LS estimator, Poisson error and noise to signal for two redshift bins when $M_{200} > 4.95 \times 10^{13} h^{-1} M_\odot h$. The results are shown in different colors for three sizes of the random samples. Top: Redshift bin z=0.4-0.6. Bottom:Redshift bin z=1.2-1.4

7.3.1.4 Covariance Estimation

The errors caused by the finite volume of the sample (cosmic variance) are difficult to estimate. Because these estimates require information about scales that have not yet been directly observed, we can find these only by using theoretical assumptions; either using the variance among a large number of survey mocks (e.g., Manera et al. (2013) with galaxy mocks) or, on large scales using analytic prediction (e.g., Estrada et al. (2009) estimates the error covariance for the cluster correlation function assuming Gaussian perturbations).

However, there are simpler methods called resampling techniques to estimate the median, the variance and the covariance of the correlation function by using subsets of the observed data (jackknife) or drawing randomly with replacement from a set of observed data points (bootstrapping). Both methods have the advantage of being independent of model assumptions, but it may not properly account for variance due to modes on scales larger than those spanned by the survey (Estrada et al. (2009)).

In this thesis we choose the jackknife resampling method because our goal will be to measure the bias observationally in galaxy surveys. We perform an estimation of the cosmic variance in a single subsample of the light cone and postpone a more complete analysis of all the subsamples described before to understand the systematic effects arising in clustering analysis techniques.

The jackknife resampling method, first described by Tukey in 1958, consists of splitting the data-set into N sub-volumes of approximately equal area and then systematically omitting each one in turn. The resampling of the data set consist of N-1 remaining sub-volumes, with volume $(N-1)/N$ times the volume of the original data-set. The clustering measurement is then repeated on the resampling of the original data-set. We quote here the standard relation used to estimated the jackknife covariance matrix (e.g., Norberg et al. (2009) and Zehavi et al. (2002)). The covariance matrix for N jackknife re-samplings is estimated using

$$Cov(\xi_i, \xi_j) = \frac{N-1}{N} \sum_{l=1}^{N} (\xi_i^l - \bar{\xi}_i)(\xi_j^l - \bar{\xi}_l) \tag{7.49}$$

where ξ_i^l is the correlation amplitude in the i^{th} separation bin, r_i, for the subsample l, N is the number of subsample and $\bar{\xi}_i$ is the mean expectation value of ξ_i measured in the N samples

$$\bar{\xi}_i = \sum_{l=1}^{N} \frac{\xi_i^k}{N} \tag{7.50}$$

The jackknife method also accounts for the lack of independence between subvolumes with the N-1 term; recall that from one copy to the next, only two subvolumes are different.

Note that if the number of regions is increased the estimated covariance converges to a stable answer.

We estimate the covariance matrix in the light cone subsample for $M_{200} \geq 4.95 \times 10^{13} h^{-1} M_{\odot} h$ at the redshift bin $z = 0.4 - 0.6$. First, we divide the RA-DEC space into 25 equal area regions on a grid. For each recalculation of the correlation function, one cell of the grid is left out a time. Then, we repeat the procedure with 400 sub volumes. Figure 7.11 shows an example when a cell is left out when we want to divide the light cone in 25 sub volumes.

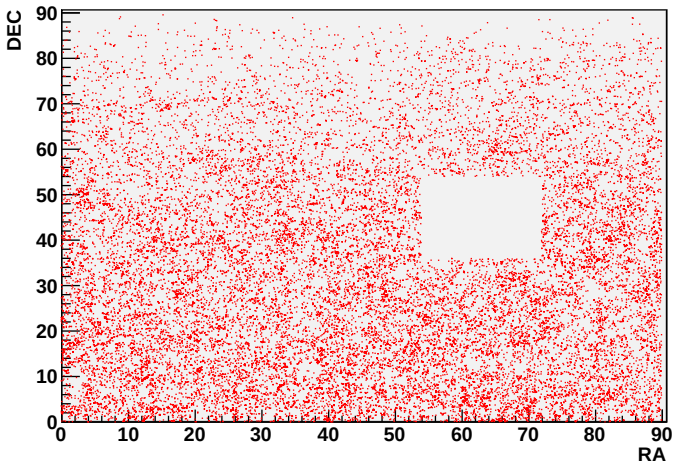

Figure 7.11: Example of subsample in the RA-DEC space using the jackknife method when one cell of the 25 subareas is left out.

Figure 7.12 shows the cross correlation coe cients, defined by

$$C_{i,j} \equiv \frac{Cov(\xi_i, \xi_j)}{\sqrt{Cov(\xi_i, \xi_i) Cov(\xi_j, \xi_j)}} \tag{7.51}$$

when we divide the sample in 25 and 400 subsamples. The off-diagonal elements differs significantly when we increase the number of sub-samples and we choose N=400 as a stable answer.

Figure 7.13 shows the measured correlation function for the last sub-sample with the shot noise and standard deviations, $\sigma_{\xi}(r_i) \equiv \sqrt{cov(\xi_i, \xi_i)}$, estimated using the jackknife method. The error comparison shows that the shot noise is $\sim 50\%$ lower than the jackknife standard deviation. Since we estimate the covariance matrix in a single subsample, we will apply this factor to estimate the covariance matrix of the other subsamples using the Poisson errors of the correlation function.

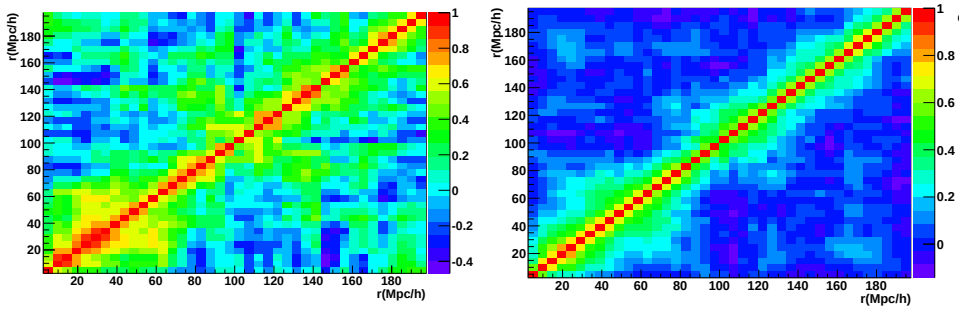

Figure 7.12: Comparison of cross correlation coe cients, $C_{i,j}$ in the subsample for $M_{200} \geq 4.95 \times 10^{13} h^{-1} M_{\odot} h$ at the redshift bin $z = 0.4 - 0.6$ when we divide it in 25 (Left) and 400 (Right) sub volumes.

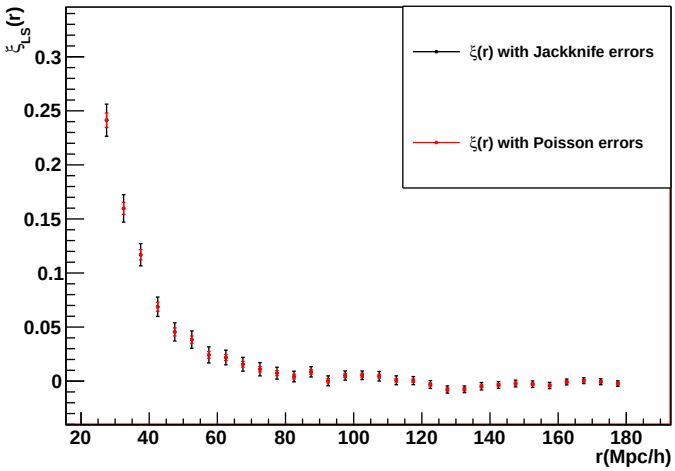

Figure 7.13: Measured correlation function for $M_{200} \geq 4.95 \times 10^{13} h^{-1} M_{\odot}$ at the redshift bin $z = 0.4 - 0.6$. The error bars are the standard deviations $\sigma_{\xi}(r_i) \equiv \sqrt{cov(\xi_i, \xi_i)}$ estimated using the jackknife method (black points) and the shot noise (red points).

7.3.2 Halo Bias Results in Simulations

First, we will test the linear bias model predictions using the Hubble Volume snapshot at $z = 0$. Later we will study the clustering evolution with redshift in the light cone.

7.3.2.1 Hubble Volume Snapshot at z=0

We have measured the two point correlation function ξ_{hh} in the snapshot for four mass thresholds. Figure shows 7.14 these measurements with the LS estimator with the Poisson errors. As expected, the more massive the halos the more biased the correlation function. The correlation function from the simulation also shows the acoustic peak at $\sim 105h^{-1}Mpc$. We display the measurements made with the denser random catalog to minimize the Poisson error. As we studied more in detail in 7.3.1.3(see Figure 7.9), the error bars increase for larger scales and for higher halo mass threshold where the number of halos is lower. We calculate the halo linear bias by

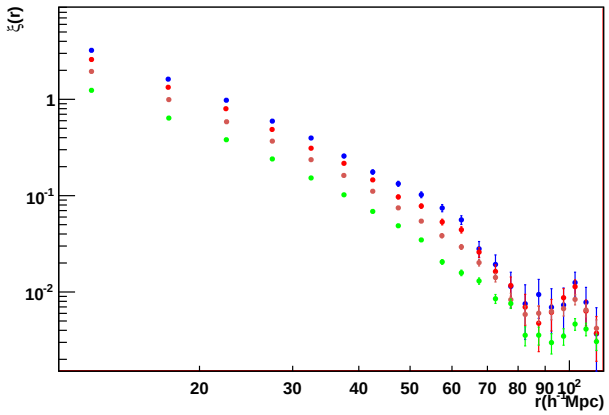

Figure 7.14: Data points are the measured two point correlation function for four mass thresholds of the HVS snapshot at z=0: $M \geq 1, 2, 3, 4 \times 10^{14}h^{-1}M_{\odot}$ (Green, brown, red and blue respectively). Error bars are the Poisson errors.

fitting the matter correlation function at z=0 to the one estimated with the simulations shown before in the interval $r = 22.5 - 57.5h^{-1}Mpc$ (Equation 7.41). The bias is expected to be constant at large scales and we don't find scale variations of b. The best fits are shown in Figure 7.15 (solid lines) and the bias measurements in the four mass thresholds are shown in Figure 7.16. The predictions for the halo linear bias derived from the Sheth and Tormen (1999) model using Equation 7.21 are also displayed with the p and q fiducial values. We observe a good agreement in the four mass threshold.

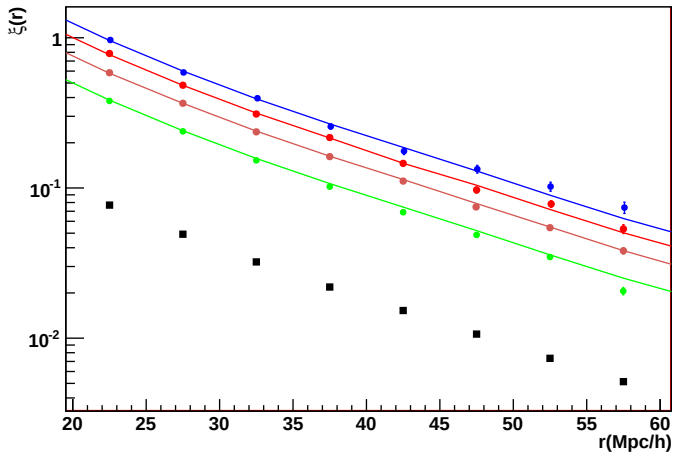

Figure 7.15: The same measured two point correlation functions but now from $r = 22.5 - 57.5\ h^{-1}Mpc$. Solid curves are the best fits for the non linear Halofit matter correlation function. The bottom black points are the theoretical predictions for the non linear Halo-fit matter correlation function at $z = 0$, $\xi_{mm}(r)$.

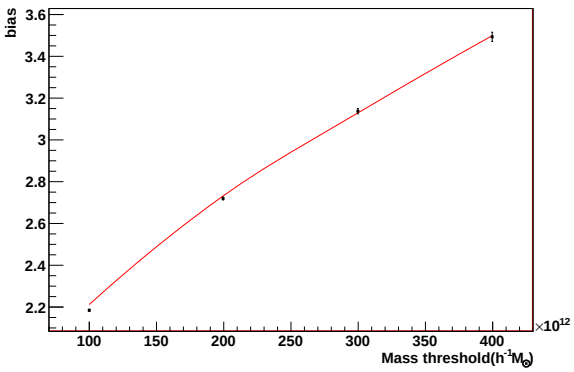

Figure 7.16: Comparison of the different measurements of the halo linear bias with the Sheth and Tormen (1999) model predictions. Black dots are the measurements for the four mass thresholds using HVS snapshot at z=0 and red line is the model prediction.

7.3.2.2 DES Light cone simulations

Using the measurements of the halo correlation function for the four mass thresholds and six redshift bins of the light cone simulations we measure the halo linear bias. In this case, for each redshift bin we fit the matter correlation function calculated at the mean of the redshift bin, $\xi_{mm}(r)$, to the one estimated with simulations. Figure 7.17 shows the matter correlation function, ξ_{mm}, at the mean value of the six redshift bins. They are calculated using Equation 5.30, where $P_{NL}(k)$ is the non linear Halofit power spectrum at z.

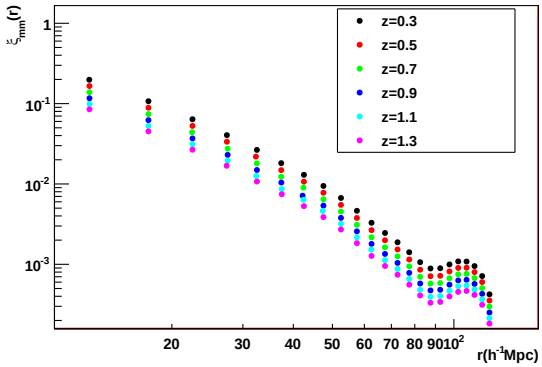

Figure 7.17: Matter correlation function ξ_{mm} for the mean of the six redshift bins calculated using the Fourier transform of the nonlinear Halo-fit power spectrum.

To calculate the bias, $b(M_{th}, \Delta z)$, we minimize the χ^2 when the ξ_i are not independent but rather have a covariance matrix, $V_{ij} = Cov(\xi_i, \xi_j)$, described before. Then

$$\chi^2(b(M_{th}, \Delta z)) = \sum_{i,j} (\xi_i - b^2(M_{th}, \Delta z) * \xi_{i,mm}) V_{i,j}^{-1} (\xi_j - b^2(M_{th}, \Delta z) * \xi_{j,mm}) \tag{7.52}$$

where ξ_i and $\xi_{i,mm}$ are the measured and matter correlation function respectively for each separation bin, i, and $b(M_{th}, \Delta z)$ is the fit parameter. Note that the inverse of the covariance matrix have to be computed.

Figure 7.18 shows the best fits in the interval $r = 22.5 - 57.55\ h^{-1}Mpc$ at $z = 0.4 - 0.6$ and $z = 1.2 - 1.4$ for four mass thresholds, $M \geq 0.45, 0.6, 0.8, 1 \times 10^{14} h^{-1} M_{\odot}$. For this analysis, we compare the bias results using different separation intervals (i.e., $r = 22.5 - 57.5\ h^{-1}Mpc$, $r = 20 - 195\ h^{-1}Mpc$ and $r = 60 - 195\ h^{-1}Mpc$) and we don't find significant scale variations. The predictions for the halo linear bias are calculated using Equation 7.40. In this case, apart from the Sheth and Tormen (1999) model, we also study the Tinker et al. (2010) prescription because the SO algorithm is used in the

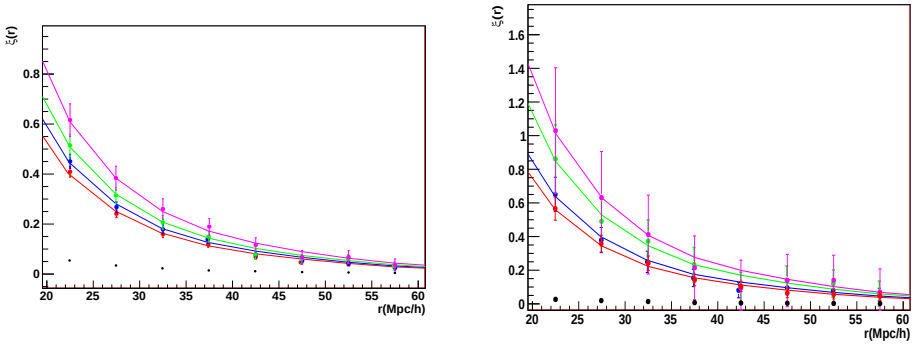

Figure 7.18: Measured correlation function at $z = 0.4 - 0.6$ $h^{-1}Mpc$ (Left) and $z = 1.2 - 1.4$ (Right) for the four samples $M \geq 0.45, 0.6, 0.8, 1 \times 10^{14} h^{-1} M_{\odot}$ (Red, blue, green and pink points respectively). Error bars are the jackknife errors. The bottom black points are the theoretical predictions for the non linear Halo-fit matter correlation function, $\xi_{mm}(r)$, at $z = 0.5$ and $z = 1.3$. The solid curves are the best fit models in the interval $r = 22.5 - 57.5 h^{-1} Mpc$ (solid curves). Error bars are the jackknife errors.

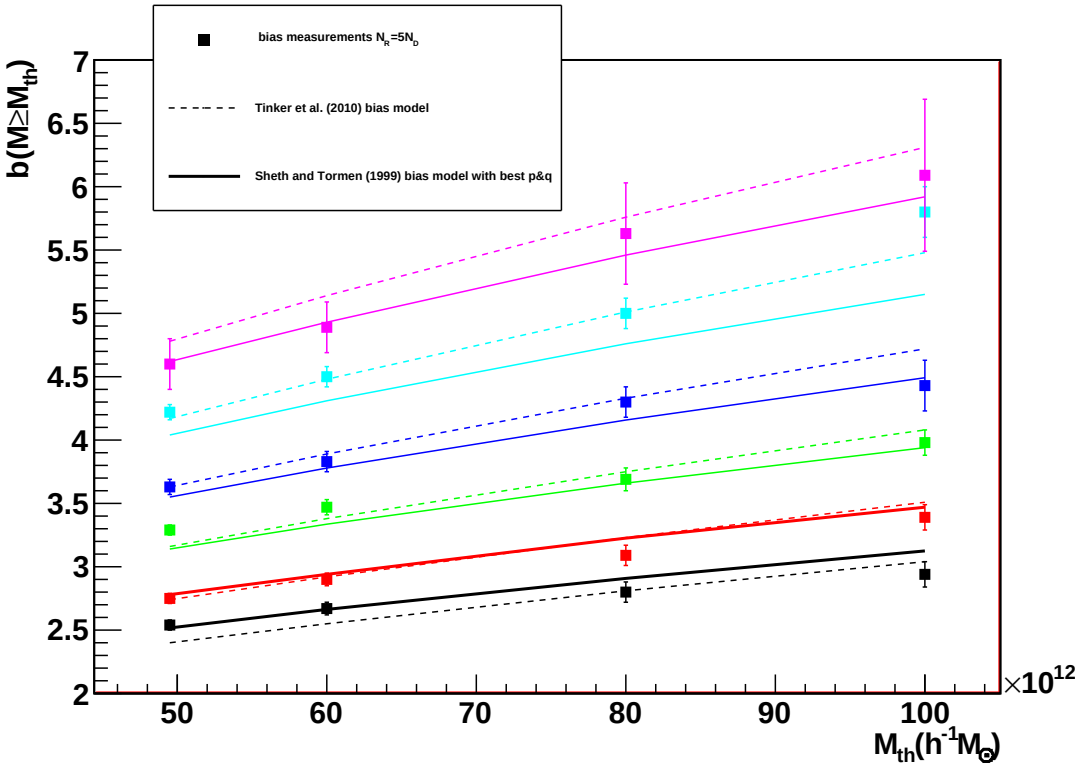

Figure 7.19: Comparison of Tinkelight coner (dashed curves) and best p and q ST model (solid curves) with measurement in light cone for $N_R = 5N_D$.

light cone. Figure 7.19 shows the comparison of the bias predictions models with the measurements in simulations. The results shows how the bias errors increase with increasing mass and redshift because the number of halos is lower.

Chapter 8

From Halos to Clusters. Measuring the Scatter of the Observable-Mass relation

Abstract: We will use the halo model to predict galaxy and cluster clustering and construct a model for the bias to compare with observations . Then we will show how measurements of clusters clustering can constrain the scatter of the scaling relation. In particular, we will use the DES simulations to study how accurately we will measure the scatter in the near future DES cluster catalog.

8.1 Halo Model of Galaxy Clustering

As we mention in previous chapter, see Section 7.2, unfortunately it is hardly possible to measure dark matter halos directly. So it is an important question how to connect theory that has developed to the Universe which can be easily observed.

We need a theory on how galaxies form within the dark matter framework although the details of this process are not well understood.

In the approach of White and Rees (1978), the central galaxies form at the center of dark matter halos as baryonic matter falls into the halo and cools. During the evolution of large scale structure, some of the dark matter halos merge to build larger halos. When a big halo merges with a small one, the galaxy of the small becomes a satellite galaxy within the resulting halo.

In the course of time more and more galaxies get assembled in the dark matter halos. In the case of a very huge halo it is called galaxy cluster. More massive the halos may contain many galaxies and typically low mass halos may contain no galaxies.

The halo model (Cooray and Sheth (2002b)) is based in a few straightforward assumptions in the framework explained before.

First, all galaxies reside within halos according to a certain spherical density profile, where there is always a galaxy at the center of the halo.

Second, in order to compute galaxy clustering statistics, it is necessary to specify the number of galaxies and the spatial and velocity distributions of galaxies within halos. The number of galaxies is specified by the probability for a halo of fixed virial mass M, to play host to N galaxies, $P(N\ M)$. The distribution $P(N\ M)$ is called halo occupation distribution (HOD) (as we mentioned in Chapter 3) and it is the main ingredient of the halo model. As we explain in next subsection, the HOD is one of the most powerful methods to describe the galaxy bias and it also provides recipes to place galaxies within dark matter halos (see Section 8.2).

The third assumption is that the galaxy content of halos is statistically independent of the halo environment and depends only on the mass M of the halo.

All these assumptions are reasonable to some extent or are warranted by observations, but they also show the limitations of the halo model. There is some evidence that this last assumption does not hold to high accuracy. There are discussion in the literature about the dependency of the HOD on the cosmic envirement in addition to the mass of the halo (i.e., Croft et al. (2012)).

In the following we develop the formalism of the halo model keeping as simple as possible.

8.1.1 The Galaxy Correlation Function and Bias

From the assumption that all galaxies resides within dark matter halos it follows immediately that given a halo population and a HOD, we can calculate the galaxy autocorrelation function. This correlation is conventionally written as the sum of two terms.

$$\xi_{gg}(\bar{r}) = \xi^{1h}_{gg}(\bar{r}) + \xi^{2h}_{gg}(\bar{r}) \tag{8.1}$$

The one halo term ξ^{1h}_{gg} is due to pairs of galaxies at separation $\bar{r}$ that lie within the same halo and the two halo term ξ^{2h}_{gg} is due to pairs of galaxies that reside in distinct halos. We can derive approximate expressions for these two terms by counting pairs at fixed separations.

The one halo term is given by

$$\xi^{1h}_{gg}(\bar{r}) = \frac{1}{\bar{n}^2_g} \int dM \frac{dn}{dM}\ N(N-1)\ M\ \int d^3y u(\bar{y}\ M) u(\bar{y} + \bar{r}\ M) \tag{8.2}$$

and the two halo term

$$\xi_{gg}^{2h}(\bar{r}) = \frac{1}{\bar{n}_g^2}\int dM_1 \int dM_2 \frac{dn}{dM_1}\ N\ M_1\ \int dM_2 \frac{dn}{dM_2}\ N\ M_2\ \times$$
$$\int d^3\bar{x}_1 u(\bar{x}-\bar{x}_1\ M_1)\int d^3\bar{x}_2 u(\bar{x}-\bar{x}_2\ M_2)\xi_{hh}(\bar{x}_1-\bar{x}_2\ M_1, M_2) \qquad (8.3)$$

where ξ_{hh} is the two point correlation of halos of mass M_1 and M_2 and $\bar{n}_g^2$ is the mean number density of galaxies given by

$$\bar{n}_g = \int dM \frac{dn(M)}{dM}\ N\ M \qquad (8.4)$$

The one halo term depends upon the HOD through the mean number of galaxy pairs per halo as a function of mass $N(N-1)\ M$ while the two halo term is sensitive to the mean number of galaxies per halo $N\ M$.

Also note that there are more changes respect to the Equations 7.30 and 7.31. First, the $u(\bar{x}\ M)$ denotes the mean radial galaxy density profiles rather than dark matter around the halo center. Second, in the one halo term for halos which contains only a single galaxy, it is natural to assume that the galaxy sits at the center of its halo. To model this Cooray and Sheth (2002a) give an analytic approximation to deal with this complication.

On large scales the two halo term dominates the correlation function. The pairs come from separated halos and separations are larger than the virial diameter of largest halos. We can express the two halo term in terms of the weighted value of the halo bias (Berlind and Weinberg (2002)). Thus, the galaxy correlation function simplifies to

$$\xi_{gg}^{2h}(\bar{r}) = b_{gal}^2 \xi_m(\bar{r}) \qquad (8.5)$$

where b_{gal} is the mean large scale bias of any particular galaxy population given by

$$b_{gal} = \frac{1}{\bar{n}_g}\int dM \frac{dn}{dM}\ N\ M\ b(M) \qquad (8.6)$$

and $b(M)$ is the halo bias.

8.2 Construction of the Cluster Catalog with a DES volume

We create a cluster catalog using the DES v1.02 halo mock catalog light cone in order to measure the bias for clusters with $N \geq N_{th}$, where N_{th} is the richness threshold. Then we will apply our method to constrain the scatter in the mass richness relation, σ_{lnM}.

We assign a richness N to dark matter halos by means of a lognormal conditional distribution $P(N\ lnM)$

$$P(N\ lnM) = \frac{1}{\sqrt{2\pi\sigma^2_{lnM}}} exp\Big[-\frac{1}{\sqrt{2\sigma^2_{lnM}}}(ln\ M\ N\ \ - lnM)^2\Big] \tag{8.7}$$

Note that this expression comes from the Equation 3.2 where the observable is the richness, N. The true underlying mass M is the halo mass M_{200} defined by the spherical overdensity $\Delta = 200$ measured in the light cone simulation and the mass richness relation $M\ N$ is given by Equation 3.4. In Table 8.1 are the fiducial values of α and B of the mass richness relation or the priors described by Rozo et al. (2009). For simplicity we ignore the bias term given in Equation 3.3 and concentrate on the impact of scatter σ_{lnM} alone. This scatter σ_{lnM} will not vary neither with redshift nor mass.

Parameter	Prior
$\alpha_{M\|N}$	$1.06\ \pm 0.08(stat) \pm 0.23(sys)$
$\mathrm{B}_{M\|N}$	$0.95\ \pm 0.07(stat) \pm 0.10(sys)$

Table 8.1: Priors from M-N relation

To resume, we have introduced a scatter to each halo with mass M_{200}

$$lnM_{measured} = lnM_{200} + x \tag{8.8}$$

where x is a variable generated by a normal distribution with mean zero and standard deviation σ_{lnM}. And then we assign the richness N.

Figure 8.1 shows $P(N\ lnM)$ for our HOD model when $\sigma_{lnM} = 0.2$. Each point represents the number of galaxies that occupy a particular dark matter halo showing that the observable mass tracer N is noisy. We create cluster catalogs with three scatter values ($\sigma_{lnM} = 0.1, 0.2$ and 0.4) in order to measure the bias and recover the scatter. Our method, which we discuss below in Section 8.4, compares the bias measured with a model that we define now in next section.

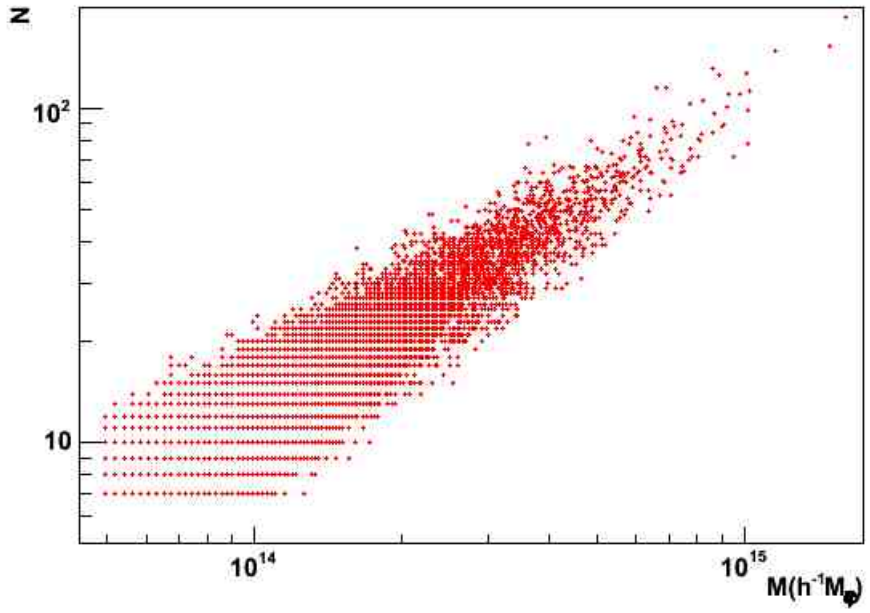

Figure 8.1: $P(N\ lnM)$ for our HOD model when $\sigma_{lnM} = 0.2$.

8.3 Theoretical Predictions of the richness bias using the Halo Model

In this section we define the model for the bias for a richness cut $N \geq N_{th}$. This is given by

$$b(N_{th}, z) = \frac{\sum_{N=N_{th}}^{\infty} b(N, z) n_{measured}(N, z)}{\sum_{N=N_{th}}^{\infty} n_{measured}(N, z)} \tag{8.9}$$

where $n_{measured}$ is the number of halos per redshift and richness value measured in the simulations created as is explained in Section 8.2, and $b(N, z)$ is modeled using the halo model of galaxy clustering explained before in Section 8.1. The bias expected for a richness value is given in terms of the halo mass function, $\frac{dn}{dlnM}(lnM, z)$ and the underlying bias, $b(lnM, z)$

$$b(N, z) = \frac{\int dlnM \frac{dn}{dlnM}(lnM, z) P(lnM \quad N) b(lnM, z)}{\int dlnM \frac{dn}{dlnM}(lnM, z) P(lnM \quad N)} \tag{8.10}$$

where the $p(lnM\ N)$ is proportional to the conditional probability of assigning a richness N to a dark matter halo of mass M, $p(N\ lnM)$ if we apply the Bayes Theorem. As we describe in Section 8.2, $p(N\ lnM)$ is given by the lognormal distribution (Equation 8.7) where the mean is given by Equation

3.4 and a scatter σ_{lnM}. Therefore,

$$P(lnM\ N) \quad exp\Big[-\frac{1}{\sqrt{2\sigma^2_{lnM}}}(ln\ M\ N\ - lnM)^2\Big] \tag{8.11}$$

Figure 8.2 shows the predictions of the richness bias for the three catalogs created with $\sigma_{lnM} = 0.1$, 0.2 and 0.4 when we use the Sheth and Tormen (1999) model for the halo mass light cone function and bias. The bias is shown as a function of richness threshold for 3 redshift values using the light cone ΛCDM cosmological parameters. In order to evaluate the predictions we measure the number of clusters per richness and Δz value, $n_{measured}(N, \Delta z)$.

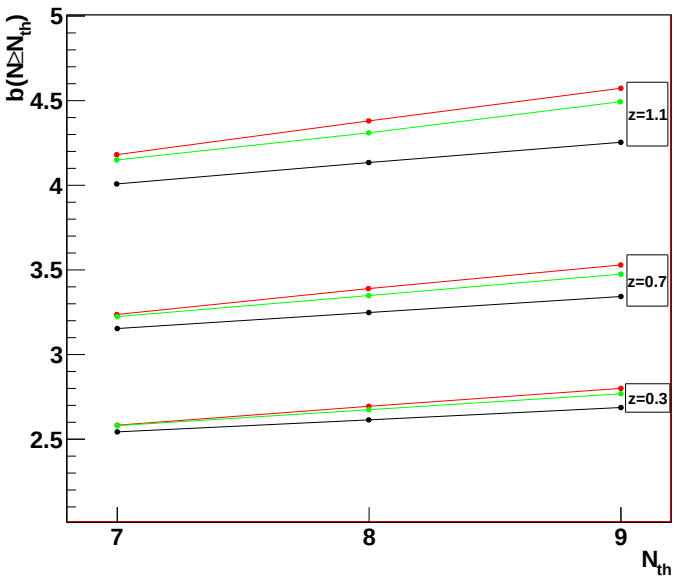

Figure 8.2: Richness bias predictions for catalogs created with $\sigma_{lnM} = 0.1$ (red), 0.2 (green), and 0.4 (black) at z=0.3 0.7 and 1.1. The upper value corresponds to z=1.1 and the lower to z=0.3.

The impact of the scatter is significant greater at high mass and redshift. The model shows how the decrement of the bias with the scatter increase with the redshift z and richness threshold N_{th}. This is due to the shape of the mass function. As we explained in Section 3.3, the steepness of the mass function around the threshold determine the excess due to upscatter (left side of the mean). As the observable threshold, N_{th} reach the exponential tail of the mass function, the excess of upscatter versus downscatter can become a significant fraction of the total (Lima and Hu (2005)) and the bias decrease. As higher is the scatter more the bias decrease. For a fixed richness, the

steepness of the mass function is higher at high redshift than at low redshift and the bias decrement will increase (see left of Figure 8.3). Following the same reasoning, for a fixed value of redshift the bias will increase more at higher N since we are further in the exponential tail (see right of Figure 8.3).

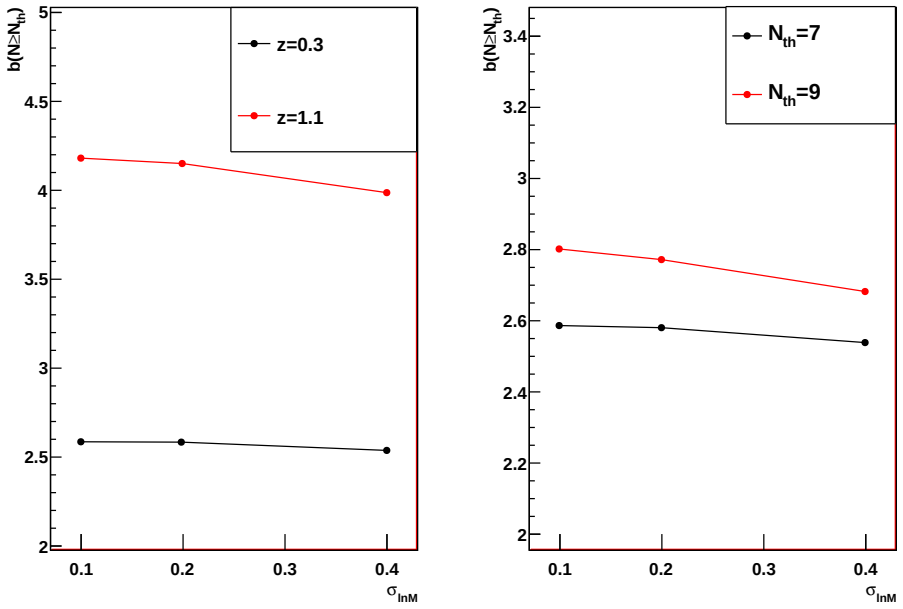

Figure 8.3: Left: Richness bias model as a function of σ_{lnM} at z=0.3 and z=1.1 for $N_{th} = 7$. Right: Richness bias model as a function of σ_{lnM} at z=0.3 for $N_{th} = 7$ and $N_{th} = 9$.

8.4 Likelihood Analysis. Constraining the Scatter

We divide the catalogs in redshift bins Δz and make cuts in richness to measure the bias with the two point correlation function. Therefore, we have a set of n bias measurements, $b_i^{measured}(N \geq N_{th}, \Delta z)$ and their bias error, $\sigma_{b_i}^{measured}$. We assume a model for the bias, $b^{model}(N_{th}, z)$, with parameters $\theta = (\Lambda, \alpha_{M|N}, B_{M|N}, \sigma_{lnM})$. Since our goal is to constrain the scatter σ_{lnM}, we will consider a one dimensional likelihood given by the conditional probability distribution of the data, $\mathcal{L} = p(b^{measured}\ \theta = \sigma_{lnM})$

$$p(b^{measured}(N_{th},z));\theta) = \frac{1}{\overline{2\pi}\sigma_{bmeasured}} \exp \frac{(b^{measured}(N_{th},z) - b^{model}(N_{th},z))^2}{2\sigma^2_{b^{measured}}} \tag{8.12}$$

then the probability of all n measurements, the likelihood, is the product of the probabilities of the individual measurements

$$\mathcal{L} = \prod_{i=1}^{n} p(b_i^{measured}(N_{th},z);\theta) \tag{8.13}$$

We can transform from the likelihood to the probability for the parameters given the data $p(\theta = \sigma_{lnM}\ b_i^{measured})$ using Baye's Theorem. This requires multiplying by a prior p.d.f and divide by the probability of the data, $p(b_i^{measured})$.

We set $p(b_i^{measured}) = 1$. For simplicity, we don't treat with priors and assume we know the cosmological parameters of the simulation and the α and B parameters. Therefore,

$$p(\sigma_{lnM}\ b_i^{measured}) \quad \mathcal{L} \tag{8.14}$$

where we include the normalization factor in the p.d.f that involve σ_{lnM}. Since we ignore the priors, we can find the most likely σ_{lnM} maximizing the likelihood.

8.5 Forecast and Error Estimation for the Scatter on DES volume

We want to estimate the error for the scatter σ_{lnM} using the likelihood analysis explained before. Instead of the data values we use the theory predictions for a fiducial model with scatter σ_{lnM}^{true}. We use the Sheth and Tormen (1999) and Tinker et al. (2010) models. We assume that each point has its expected experimental error, $\sigma_{b_i}^{measured}$, obtained from the fits to the correlation function. The data samples are the same we described in Figure 8.2 except the cut on N=8.

Table 8.2 and Figures 8.4 and 8.5 show the 68% errors on the scatter, $\sigma(\sigma_{lnM})$ and their recovered values, σ_{lnM}. We also show the results when we take the lower mass limit of the simulation into account to model the richness bias. These are called $\sigma(\sigma_{lnM})^*$ and σ^*_{lnM} .

The predictions show high accuracy to recover the scatter. The precision to measure the scatter may be better at higher values because the second derivative of the bias with the scatter is negative, $\frac{\partial^2 b(N_t h,z)}{\partial \sigma^2_{lnM}} < 0$.

Figure 8.6 show the richness bias as a function of the scatter using the richness catalog created with $\sigma_{lnM} = 0.2$. Since we want to perform the

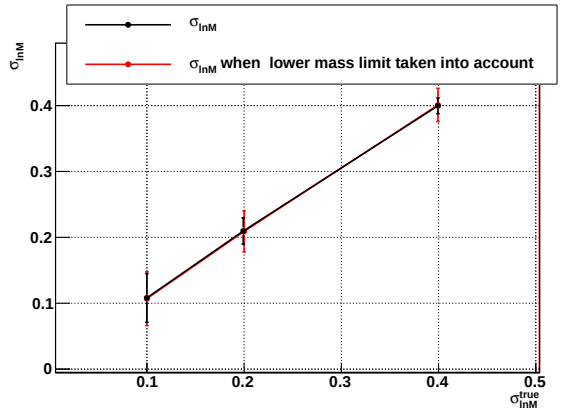

Figure 8.4: Scatter recovered values, σ_{lnM} for different scatter values taken as fiducial model. The expected errors (68% C.L.) σ^{true}_{lnM} are also shown. The red dots show the results when the lower mass limit of the simulation is taken into account.

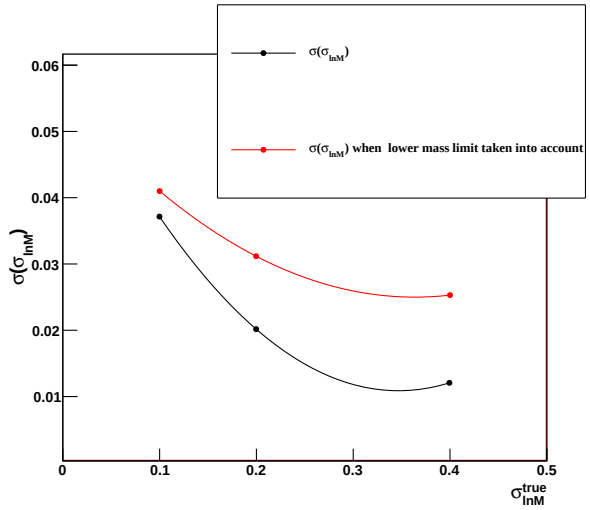

Figure 8.5: Expected errors (68% C.L.) for different scatter values taken as fiducial model, σ^{true}_{lnM}. We loose precision when the lower limit of the simulation is taken into account (red dots).

σ_{lnM}^{true}	σ_{lnM}	$\sigma(\sigma_{lnM})$(68 % CL)	σ_{lnM}^{*}	$\sigma(\sigma_{lnM})^{*}$ (68%CL)
0.1	0.108	0.037	0.107	0.041
0.2	0.208	0.020	0.209	0.031
0.4	0.399	0.012	0.400	0.025

Table 8.2: Scatter recovered values, σ_{lnM} and expected errors, $\sigma(\sigma_{lnM})$ (68% C.L.) for different scatter values taken as fiducial model, σ_{lnM}^{true}. The results when the lower mass limit is taken into account (σ_{lnM}^{*} and $\sigma(\sigma_{lnM})^{*}$ (68%CL)) are also shown.

likelihood to obtain the best value, we calculate how vary the richness bias with the scatter for a given catalog using Equation 8.10. Note that it is different to the Figure 8.2 in Section 8.3, where we model the richness bias for each catalog.

Figure 8.7 shows the decreasing slope for two redshift values, z=0.3 and z=1.1 for $N_{th} = 9$ using the same catalog. As it is predicted the slope decrement increases with the redshift and also with richness. Therefore, we might also found better precision at higher values of redshift and richness.

Although the dominant systematic we have found is the uncertainty in the halo mass and bias function, other source of systematics is the mass resolution of the light cone simulation. The catalog was designed to resolve the collapse of Coma-sized cluster with 500 particles. The particle mass is $2.2 \times 10^{12} h^{-1} M_{\odot}$ yielding a simulation with halos in the range $4.95 \times 10^{13} h^{-1} M_{\odot} \leq M_{200} \leq 2.15 \times 10^{15} h^{-1} M_{\odot}$.

The minimum halo mass introduces a systematics that affects our richness bias model predictions specially when our observable mass is closer to the minimum. Figure 8.8 shows the comparison between the richness bias predictions at two redshifts when we integrate taken into account the lower mass limit of our simulations and when we integrate in a wider range $1 \times 10^{12} h^{-1} M_{\odot} \leq M_{200} \leq 1 \times 10^{16} h^{-1} M_{\odot}$. We choose the case when $\sigma_{lnM}^{true} = 0.2$. In the first case, since we are removing halos from the left side of the lognormal distribution where the bulk of the values lies, the decreasing slope of the bias with scatter is lower than when we don't remove them. Thus we will loose precision to recover the scatter as the results shows (see Figure 8.5). Moreover, as higher is the scatter the disagreement between the two cases is higher and the minimum halo mass systematic is more significant.

Our conclusion is that we may estimate the scatter σ_{lnM} with a precision of $\sim 4\%$, $\sim 3\%$ and $\sim 2.5\%$ for $\sigma_{lnM}^{true} = 0.1, 0.2$ and 0.4 respectively when we take into account the minimum halo mass. Our precision would be better without this limitation. For a cluster cosmology experiment instead of the mass resolution, the systematics would be the minimum observable richness.

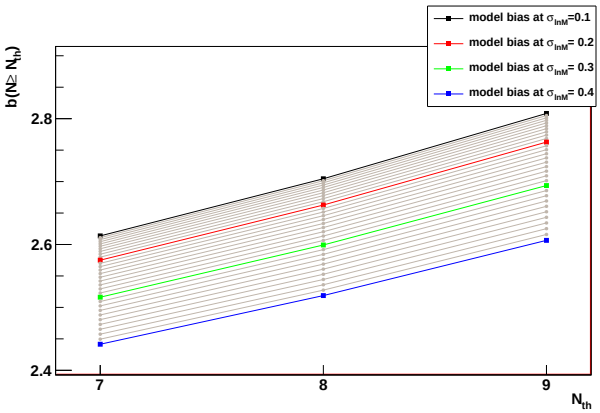

Figure 8.6: Bias model as a function of σ_{lnM} and N_{th} at z=0.3 using the catalog created with $\sigma_{lnM} = 0.2$.

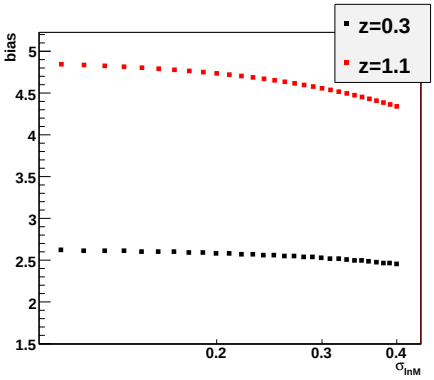

Figure 8.7: Bias model as a function of σ_{lnM} at z=0.3 and z=1.1 for $N_{th} = 9$ using the catalog created with $\sigma_{lnM} = 0.2$. The slope of the bias decreases with the scatter.

As we mention in Section 4.3, we expect a 0.33 of uncertainty at 1 σ level in the mass richness relation for the DES survey. Thus, we found that we can estimate the scatter with a precision of $\sim (0.1 - 0.28)\%$ as our predictions shows. Moreover, based on appendix of Rozo et al. (2011) paper, the dark energy parameters won't be significantly biased.

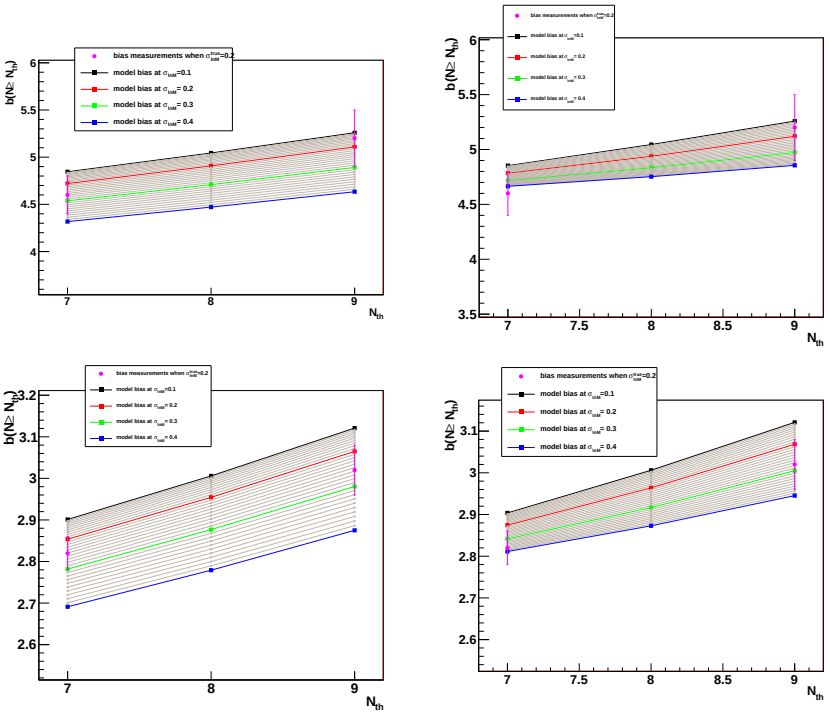

Figure 8.8: Top left: The squares are the bias model predictions as a function of σ_{lnM} and N_{th} at z=1.3 using the catalog created with $\sigma_{lnM}^{true} = 0.2$. The magenta circles are the bias measurements with their errors. Top right: The same results as top left but in this case the minimum halo mass is taken into account. Bottom left:The squares are the bias model predictions as a function of σ_{lnM} and N_{th} at z=0.5 using the catalog created with $\sigma_{lnM}^{true} = 0.2$. The magenta circles are the bias measurements with their errors. Bottom right: The same results as bottom left but in this case the minimum halo mass is taken into account.
Note: The color code of σ_{lnM} for all the figures is σ_{lnM}=0.1 (black) , 0.2 (red), 0.3 (green) and 0.4 (blue).

8.6 Scatter Constraints

We perform a likelihood calculation comparing the richness bias model predictions with the measurements for the three catalogs created as we explain before.

Figure 8.9 and Table 8.3 and 8.4 show the scatter constrains and their $68\%(C.L.)$ errors for the two theoretical models. We also show the results when we take into account the lower bound in mass of the simulation. As we predict before, at highest σ_{lnM} the precision is better and both models agree. We obtain better accuracy when we take into account the lower limit in mass although we can't recover the true scatter value when $\sigma_{lnM} = 0.1$ in any case for both models. However, for $\sigma_{lnM} = 0.2$ we can only recover the value with the Sheth and Tormen (1999) model because we obtain better accuracy when model the mass function and bias.

If we interpolate our results, we confirm that we can measure the expected scatter value for DES survey with a precision of ≤ 0.05.

σ_{lnM}^{true}	σ_{lnM}	$\sigma(\sigma_{lnM})$(68 % CL)	σ^{*}_{lnM}	$\sigma(\sigma_{lnM})^{*}$ $(68\%CL)$
0.1	0.036	0.044	0.013	0.063
0.2	0.172	0.027	0.206	0.035
0.4	0.319	0.017	0.399	0.031

Table 8.3: Scatter recovered values, σ_{lnM} and expected errors, $\sigma(\sigma_{lnM})$ (68% C.L.) using Sheth and Tormen (1999) model for the three catalogs created. The results when the lower mass limit is taken into account (σ^{*}_{lnM} and $\sigma(\sigma_{lnM})^{*}$ $(68\%CL)$) are also shown.

σ_{lnM}^{true}	σ_{lnM}	$\sigma(\sigma_{lnM})$(68 % CL)	σ^{*}_{lnM}	$\sigma(\sigma_{lnM})^{*}$ $(68\%CL)$
0.1	0.071	0.049	0.086	0.060
0.2	0.113	0.039	0.137	0.071
0.4	0.319	0.017	0.398	0.031

Table 8.4: Scatter recovered values, σ_{lnM} and expected errors, $\sigma(\sigma_{lnM})$ (68% C.L.) using Tinker et al. (2010) model for the three catalogs created. The results when the lower mass limit is taken into account (σ^{*}_{lnM} and $\sigma(\sigma_{lnM})^{*}$ $(68\%CL)$) are also shown.

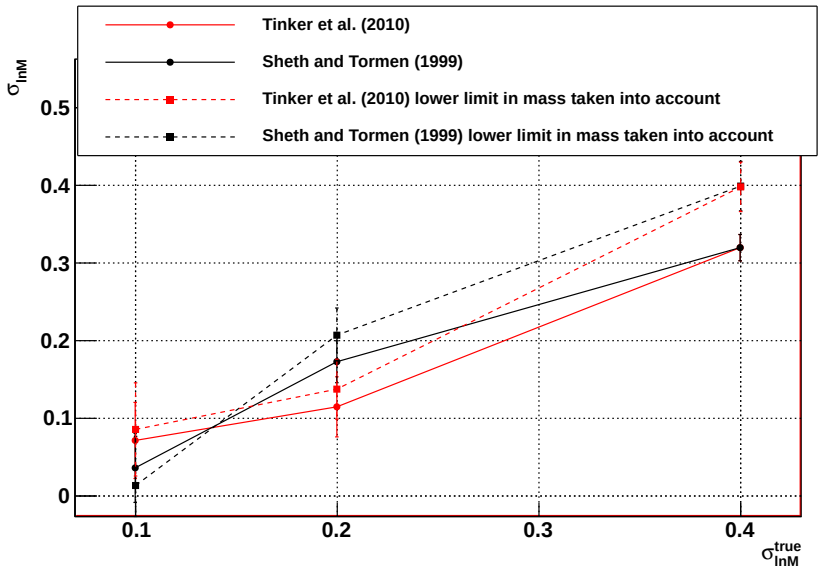

Figure 8.9: Scatter recovered values, σ_{lnM} for the three catalog created with σ_{lnM}^{true} when we use Sheth and Tormen (1999) (black dots) and Tinker et al. (2010) (red dots) models. The expected errors (68% C.L.) are also shown. The squares and dashed lines show the results when the lower mass limit of the simulation is taken into account.

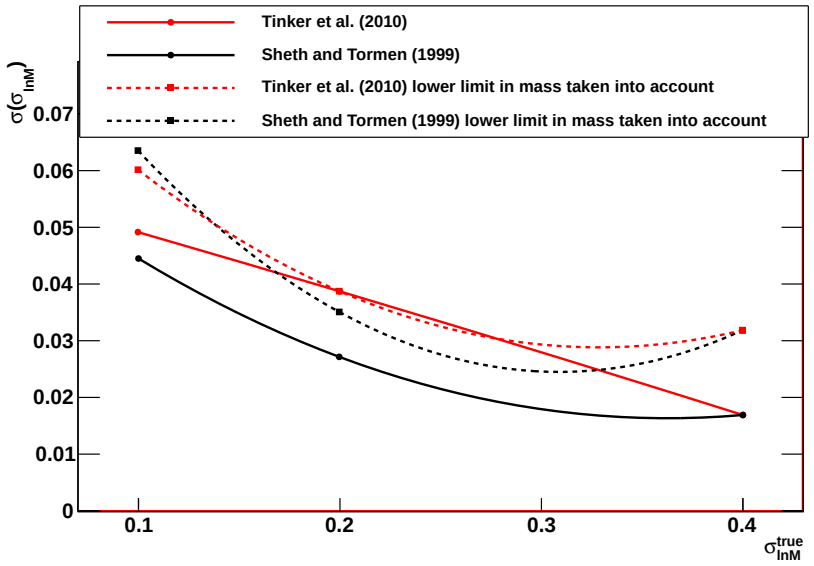

Figure 8.10: Expected errors (68% C.L.), $\sigma(\sigma_{lnM})$, for three true scatter values, σ_{lnM}^{true} . We loose precision when the lower limit of the simulation is taken into account (square dots).

Chapter 9

Conclusions

We have develop a method to measure the scatter in the mass richness relation of galaxy clusters for the future DES cluster catalog using the spatial clustering of the clusters, as characterized by the cluster correlation function. Our method compares the bias measured with the cluster correlation function with the bias predictions. Using only large optical cluster surveys it can be used as a cross check method to compare with simulations, direct methods or self calibration.

After an introduction of the basic cosmological notions in Chapter 2, in Chapter 5 we have described the statistical density uctuations that quantify the clustering of objects. In particular, the two point correlation function and its Fourier transform, the power spectrum. We have also studied the evolution of the density perturbations over time to construct the power spectrum in the ΛCDM paradigm.

In Chapter 3, after a description of the cluster as cosmological probes we have discussed the importance of the calibration of the mass observable relation as a key challenge in extracting precise cosmological constraints. We make emphasis in the scatter and how it cause ambiguities in the interpretation of the abundance of clusters and degrades the cosmological constraints. We mentioned how Rozo et al. (2009) measure the scatter in mass at fixed richness with a 22% precision with 1 σ errors using optical and X-ray observations. They use it as a external prior for cosmology with the MaxBCG cluster catalog. We also describe how with large optical cluster surveys such as HSC, it will be possible to calibrate the mass observable and provide cosmological constraints (Oguri and Takada (2011)). They combine cluster observable and weak lensing. Their forecasts shows and e cient self calibration of systematics just with optical surveys.

In Chapter 4 we introduced the DES project and the Dark Energy Camera where I worked in the CCD R&D program. The primary driver of DES is the detailed optical measurement of galaxy clusters. DES employs a very similar richness estimator to the one that Rykoff et al. (2012) uses. In this

paper they give an estimation of the scatter and find that the total uncertainty in the mass of any given cluster is ≈ 0.33 at the 1σ level. We will take this value as a rough estimation of the scatter for the DES mass richness relation. Moreover, Rozo et al. (2011) studied how precisely the scatter must be known to recover unbiased dark energy parameters using the standard self calibration method for a DES-like cluster experiment.

In order to properly measure the large scale bias for clusters, first we need to understand the large scale properties of the dark matter halos. To achieve this, we use the DES v1.02 halo mock catalog light cone sky survey with a DES volume to determine the halo abundance, the halo two point correlation function and the halo bias. Our results shows that the dominant systematics in our method is the uncertainty in the halo mass function and bias function.

In Chapter 6 we studied the accuracy of the theoretical models of the halos abundance using DES simulations. First we explained how the halo grows from a spherically mass perturbation and then refined the details of that simplified approach, based on the studies made in numerical simulations. We studied the more realistic ellipsoidal collapse model of Sheth and Tormen (1999) and the fitting function for Δ overdensities of Tinker et al. (2008). The first model with the fiducial parameter agrees with high accuracy with the measurement at $z = 0$. However, in the light cone we had to find the parameters that best fit to the simulation for every redshift bin for both models.

At lower redshift bins we found the same accuracy for both models. However, the disagreement between models increase with redshift and we found better accuracy with the Sheth and Tormen (1999) model. This difference is considered as a systematic error of our method.

In Chapter 7 we introduced the linear bias model using the extended PS formalisms and the improvements made by Sheth and Tormen (1999) and Tinker et al. (2010). We studied how the determination of halo bias is closely related to the description of halo abundance. We compared the predictions of these two models with the measurements in simulations.

We measured the linear halo bias on large scales where is considered scale independent and deterministic. To calculate the bias we measured the two point correlation function with LS estimator and study the statistical errors. In particular, we optimized the Poisson error and made a preliminary estimation of the cosmic variance using the jackknife method. We postpone for the near future a more complete analysis to understand the cosmic variance error for more mass and redshift subsamples .

Our results demonstrate that the uncertainty in the mass function produces a systematic error in our method because the halo bias depends on it. One of the reasons why we found very accurate results for the linear bias at $z = 0$ with the Sheth and Tormen (1999) prescription is because we have a

good agreement in the halo mass function. However, in the light cone we obtain a lower accuracy because we have higher deviations for Sheth and Tormen (1999) and Tinker et al. (2010) prescriptions than the deviations at $z = 0$. In addition, as in the last chapter we also considered the difference between these two models as a systematic error of our method.

After we studied the bias in halos, in Chapter 8 we developed a theoretical model of the bias to compare with observations in optical surveys such as DES. We defined the richness bias using the Halo Model of Galaxy Clustering. We took an HOD and a empirical mass richness relation with the same form used by Rozo et al. (2009) to obtain a parametrized model for the bias. We assumed that the bias only depends on the mass.

Our forecast shows the precision to measure the scatter with a DES volume. In particular, we showed the 68% C.L errors and their recovered values for three true scatter values. For simplicity the scatter not varied neither with redshift nor mass, $\sigma_{lnM} = constant$, and we ignored the bias term, $lnM_{bias} = 0$. We obtained very competitive results to measure the expected scatter in the DES mass richness relation using this very simple model for the scatter. The better precision that Oguri and Takada (2011) found was 4% when the scatter is 30%. Our method produces a precision of $\sim 2.8\%$ for the same scatter value. These results are not directly comparable because they are for different masses and scatter model. However, they are indicative of the performance of the new method.

In the forecast we had taken into account the minimum halo mass of the simulation as a systematic error. It reduces the precision to constrain the scatter. However, for a real cluster catalog such the redMaPPer , the systematic will be the minimum richness instead of the minimum halo mass.

After the forecast, we tested our method to constrain the scatter using the DESv1.02 simulations. Here we added the uncertainty in the theoretical models when we compared with simulations. We created three richness catalogs with three scatter values. After we measure the linear bias for subsamples with enough clusters , we performed a likelihood and obtained our scatter constraints. Since our goal is to develop a method to measure the scatter we assumed we known the mass richness relation parameters and the cosmological parameters of our simulation. Note that in the future DES cluster catalog we could also change the form of the scale relation.

As predicted by the forecast, at the highest scatter value, $\sigma_{lnM} = 0.4$ we obtain the highest precision and the results using Sheth and Tormen (1999) and Tinker et al. (2010) halo prescriptions agree. However, for lower values there is a discrepancy between them. Moreover, for the lowest value, $\sigma_{lnM} = 0.1$ we can't not recover the true scatter value in any case while we can recovered it for $\sigma_{lnM} = 0.2$ using Sheth and Tormen (1999) prescription. Since the DES expected scatter value is ≈ 0.33, we conclude that we can measure it and it will be precise enough for the dark energy parameters

won't be significantly biased.

In summary, the new method proposed here could be used as a cross check method complementary to others such as self calibration with large optical surveys Oguri and Takada (2011) or the method developed by Rozo et al. (2009).

In this thesis we ignore the effect of the uncertainty of the redshift of the redMaPPer clusters. The effect on the three-dimensional correlation function is a smearing of the acoustic peak and a relative damping of power on small scales (Estrada et al. (2009)). We postpone to a near future work the study of how this systematic error will affect to the bias measurement and the precision of the scatter measurements.

For future cluster surveys such as LSST we will have 20000 deg^2. Thus, we expect the statistical errors will be reduced at high mass and redshift because the number of clusters will increase considerably. With this, we forecast higher precision to measure the scatter including the lower values.

Appendix A

Focal Plane Detectors for Dark Energy Survey

Abstract: DECam has chosen fully depleted 250 μm thick CCD detectors selected for their higher quantum efficiency in the near infrared with respect to thinner devices. The detectors were developed by LBLN using high resistivity substrate. The characterization of these detectors and the comparison of these results with the technical requirements was done by the DES team. I was involve in the initial phase of the $R\&D$ program. This phase is important to learn and develop the infrastructure and experience for the production phase of the characterization to determine the best one that should populated the focal plane. In this appendix I describe the techniques and methods in which I was involve and in I which I took data.

A.1 DECam CCDs and the DES Technical Requirements

The design of the DECam imager is optimized for DES which requires observations of galaxies up to $z \sim 1$. This establishes strong specifications on the e ciency of the DECam detectors in the red and near-infrared range. The absorption length in the silicon is 205 μm at a wavelength of 1000 μm and thus thick sensors are required for a better QE at that wavelength. Recent advances in the CCD technology (Holland et al. (2003)) allow the fabrication of high resistivity ($\sim 10 k\Omega cm$) detectors, up to $\sim 300 \mu m$ thick which are fully depleted at relatively low voltages. These CCDs have a significantly higher e ciency in the near-IR and for this reason are the optical detectors chosen by groups building new mosaic cameras for astronomy, such as DEcam.

A good blue response is reached by choosing a back illuminated design so that not gate structure absorbs the UV light.

Figure A.1 shows a schematic cross-section of the LBLN CCD. It is a back illuminated, p-channel CCD thinned to $250\mu m$ and biased from the back side to be fully depleted. The charge collected in the depletion region is stored in the buried channel established a few μm away from the gate electrodes. The holes produced near the back surface must be travel the full thickness of the device to reach the potential well.

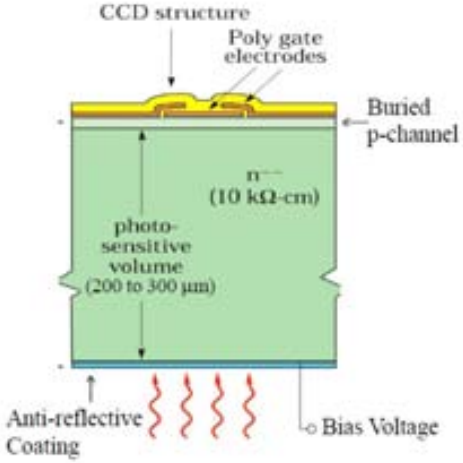

Figure A.1: DES CCD cross-section. Back illuminated, $250\mu m$ thick, p-channel CCD. See Holland et al. (2003) for more details.

The DES CCD technical requirements, established as the minimal requirements in order to achieve the science goal for the survey, are summarized in Table A.1. They correspond mostly to standard requirements for astronomical CCDs with the exception of the average quantum e ciency in the near infrared denoted as the z filter according to the Sloan Digital Sky Survey filter set (Fukugita et al. (1996)).

A.2 Packaging and Testing of DECam Detectors at Fermilab

The DECam CCDs are produced by DALSA [1] and LBLN [2] and delivered to Fermilab as diced parts. Fermilab has developed a package for these CCDs that meets the mechanical and thermal requirements established by DES (see details of DES package in Derylo et al. (2006)). A photography of the final version of the DECam science package is shown in figure A.2.

[1] http://www.dalsa.com/
[2] http://www-ccd.lbl.gov/

	description specification
1	non linearity $< 1\%$
2	full well: $> 130.000\ e^-$
3	no residual image
4	readot time $<17sec$
5	dark current $<35e^-/pix/hour$
6	QE [g,r,i,z]:$[60\%, 75\%, 75\%, 65\%]$
7	QE$< 0.5\%$ per degree K
8	read noise $< 15\ e^{-1}$
9	Charge diffusion $\sigma < 7.5\ \mu m$
10	Cosmetic defects $< 0.5\%$
11	Charge Transfer Ine ciency $< 10^{-5}$
12	Crosstalk for two amplifiers on CCD < 0.001

Table A.1: DECam technical requirements

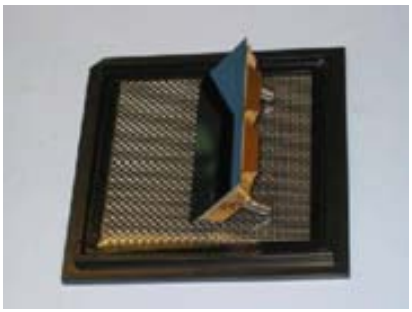

Figure A.2: DECam science package.

After each detector is packaged, it is installed on a single CCD testing station where all the DECam technical requirements are verified. An example of testing station at Fermilab is shown in figure A.3

Fermilab has established a CCD testing lab with three fully instrumented testing stations for production testing. The dewars are cooled with liquid nitrogen (LN_2) and can be controlled to maintain a stable temperature using independents PID loops. The design of the dewar shown allows for a quick detector exchange. Each dewar is illuminated by a 6 integrating sphere with three ports. The illumination source is connected on the input port, a photodiode is connected on one of the output ports and the other output port is connected to the dewar. The sphere is attached 13 from the front of the cube in order to achieve at illumination over the whole area of our detector. A monochromator is used to select the illumination wavelength. A at exposure obtained for one of the DECam CCDs is shown in figure A.4. The 0.5% variations on the signal level produced by the rings of the

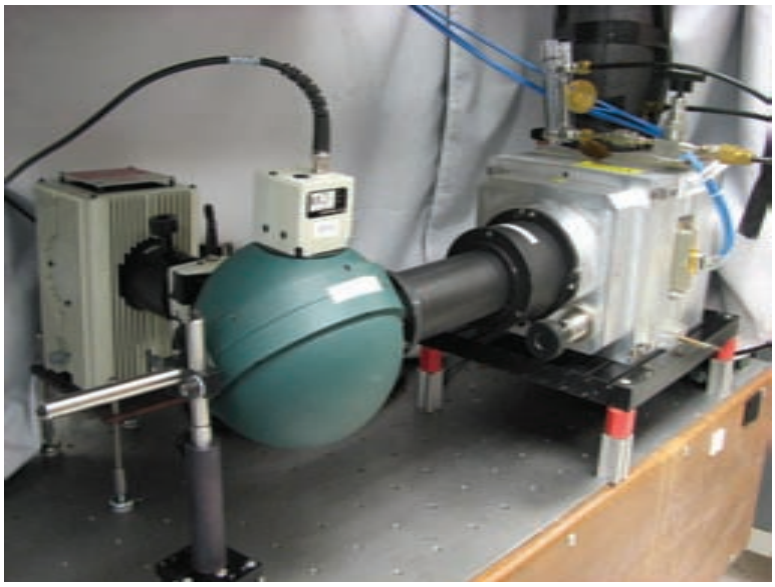

Figure A.3: CCD testing station.

resistivity variation on the silicon substrate are completed removed after a at field correction (Estrada et al. (2010))

The electronic of choice is the Monsoon system [3], a very exible system specially designed for controlling large mosaic arrays. The design of the CCD readout electronic was a combined effort of engineers at Fermilab and Spain (i.e., Shaw et al. (2012)) .

The CCD packaging and testing facilities at Fermilab have been able to maintain an average testing rate of 4 detector per week. The details of the production testing facility and procedures are presented in Kubik et al. (2010).

A.3 Characterization Techniques

The full characterization of the CCDs is done with the goal of finding the optimal operating parameters for these devices and determining if they satisfy the DES requierements presented in Table A.1. In Estrada et al. (2006) and Estrada et al. (2010) we can find the complete suite of test. However, in this appendix, I will brie y describe the techniques and methods in which I was involved and in which I took data (see also Campa (2007)). These are part of first stage tests. If the devices pass these tests more detailed studies

[3] http://www.noao.edu/nstc/monsoon/

Figure A.4: Flat exposure with a light level of $\sim 27.000e^{-}$. The serial register is divided in two and in this image the serial overscan is displayed on the center of the CCD. The parallel overscan is displayed on the top of the image (Estrada et al. (2010)).

will be done.

A.3.1 Photon Transfer Curve: Gain, Linearity and Full Well Capacity

The photon transfer curve (PTC) is one of the most valuable tools for calibrating, characterizing and optimizing performance (Janesick (2001)). During production testing for DECam several transfer curves are collected for each CDD. In our case it is used to evaluate CCD parameters such as the linearity in the response of the signal readout chain, the full well capacity and the read out noise. This curve also gives the gain of the device.

The photon transfer curve consists on taking pairs of exposures with at illumination at different light levels going up to 200000 e^{-}. The gain is measured by looking at the linear relation between the variance on the image as a function of the mean. This is the standard procedure to obtain the gain assuming a fixed electronic noise and Poisson statistic for the number of photons. Figure A.5 shows an example of the results obtained with this method. The inverse of gain is obtained as the slope of the curve, in this case is $0.9ADU/e^{-}$. An alternative method for obtaining this conversion factor between electrons and ADU is to use an image taken with an Fe^{55} X-ray source (see A.3.4).

DEcam requires it detectors to have a full well capacity larger than 130000 e^{-} and less than 1% non-linearities up to those light levels. In Figure A.6 the mean of the signal level as a function of the exposure time is represented and this data are used to confirm this requirements. The non-

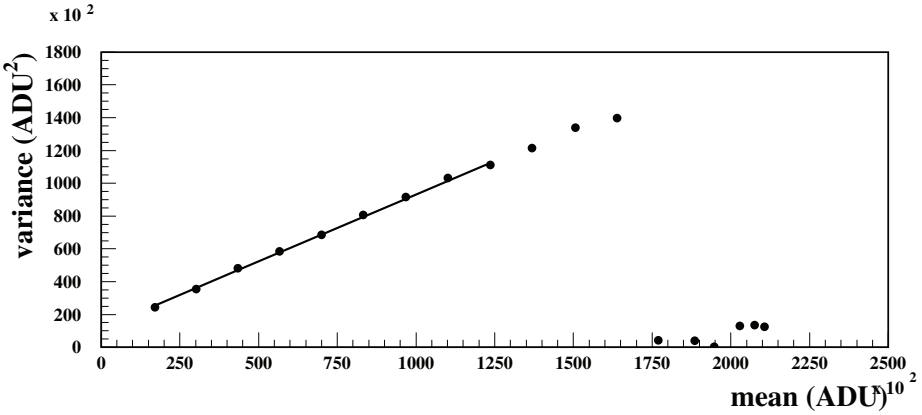

Figure A.5: Photon transfer curve: Variance as a function of mean signal during production testing of a DECam CCD (Estrada et al. (2010)).

linearity measurements are also shown. The 1% technical requirement for DECam is satisfied up to 225000 e^-.

Estrada et al. (2010)) show more studies about linearity, full well and noise using the PTC although these results are not presented here. In particular, this paper studies the CTE variation for high light levels that reduces the maximum charge that can reliably measured on a single pixel and also the performance of the readout system at low light levels.

A.3.2 Charge Transfer E ciency

The charge transfer e ciency (CTE) for the DECam science is requiered to be better than 0.99999. It denotes how much of the charge in one pixel actually gets transferred into the next pixel in a three phase clocking time. Several methods exist to measure the CTE (Janesick (2001)). During the initial phase of $R\&D$ program the CTE is studied using the extended-pixel-edge-response (EPER) technique and by the use of a Fe^{55} (see Estrada et al. (2006), Diehl et al. (2008) and Campa (2007)).

Because of the high diffusion in back illuminated CCDs and the high values of the number of pixels, the X-ray technique is very imprecise. However, the CTI was measured with X-rays in packages built with the front-side exposed (Diehl et al. (2008)).

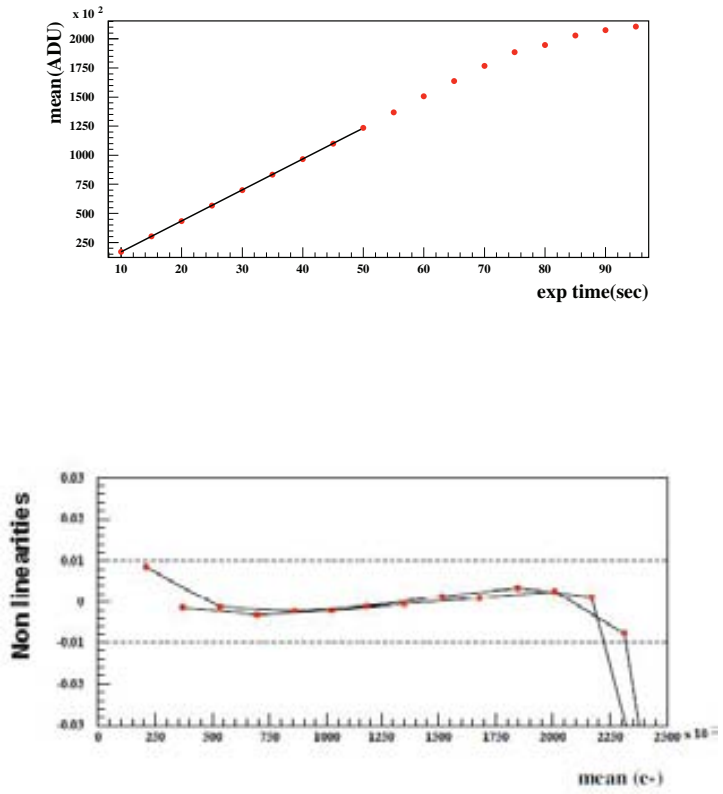

Figure A.6: Photon transfer curve from (Estrada et al. (2010)). Top: Mean of the signal as a function of exposure time. Bottom: Fractional non-linearity as a function of the mean signal.

The CTE for DECam science CCDs in the production phase is checked using the EPER technique. The CCD is illuminated with a light source and the fraction of the charge transferred from active pixels into overscan region provides the charge transfer ine ciency (CTI). Since the CTI depends on the levels of CCDs clocks, each of the four clock rails (horizontal upper and lower rail, vertical upper and lower rail) used for the transfer between pixels is varied. Finally we found a single set of clock voltages for which all the CCDs pass the technical requirements for both horizontal and vertical clocks. Figures A.7 and A.8 show an example of these studies.

As mention before, the CTE also changes with illumination.

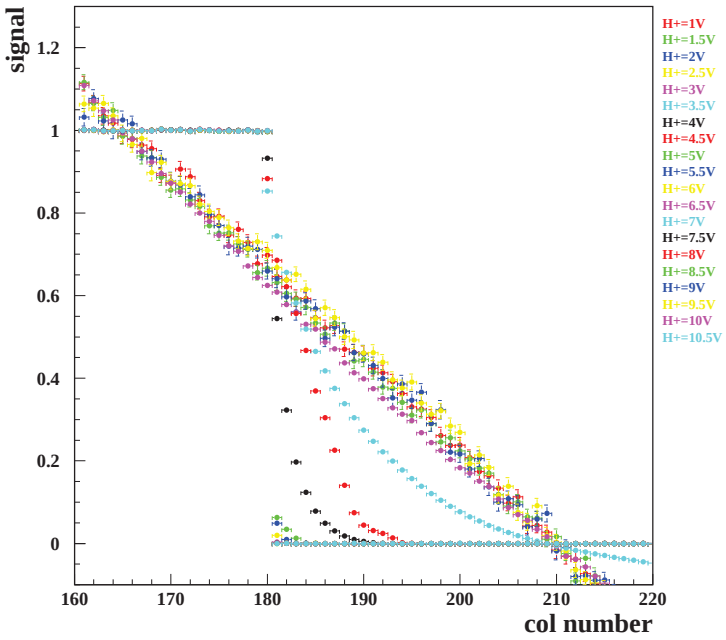

Figure A.7: Top: EPER plot. Transition between the readout of the physical pixels and the overscan as a function of the horizontal barrier H^+ for one amplifier. For a perfect transfer e ciency the transition between the exposed area (columns lower than 181) and the overscan amplifier should be perfectly sharp, going from 1 to 0 in this scale.

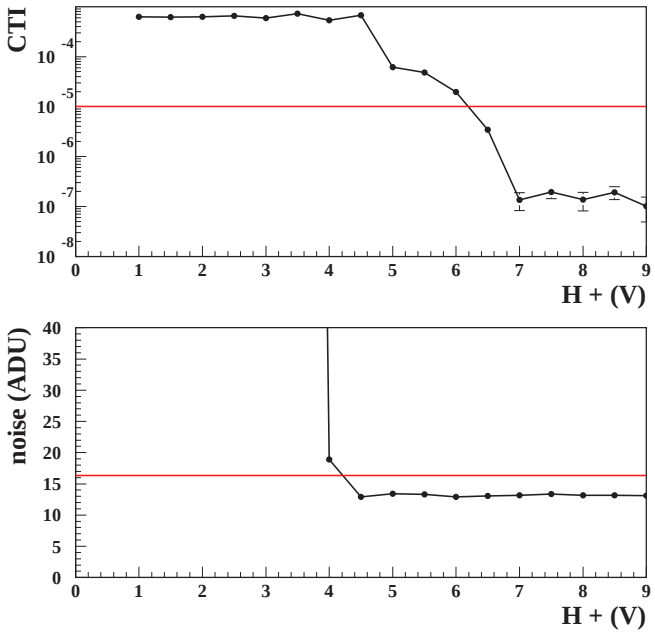

Figure A.8: Top: The CTI calculated with values of the EPER plot. CTI as a function of the H^+. Bottom: Noise as a function of the horizontal voltage H^+. Once we have a low CTI the noise is stable.

A.3.3 E ective Threshold. Output Gate Transfer Curve.

Also part of the full characterization of each CCDs is the measurement of the output transfer gate curve (see description in Janesick (2001)). The goal of the output gate transfer curve is to measure the voltage at which charge injection is produced in the device as a function of the reference voltage, V_{ref}. This technique allows the determination of the channel voltage inside the CCD, under the output gate. Charge injection occurs when this voltage is lower than the V_{ref}. The difference between the applied gate voltage and the channel voltage is typically called V_{th} and depends on the doping conditions of the silicon. Figure A.9 shows an example of the results from one device (Estrada et al. (2006)). The mean value of the signal measured in the overscan area is represented as a function of the output gate voltage, V_{OG} for different values of V_{ref}. When charge injection is produced large deviation from the pedestal values are seen. Taking the line that corresponds to $V_{ref} = -12V$, charge injection occurs for $V_{OG} < 3V$. The effective threshold voltage is $V_{th} = V_{ref} - V_{OG} = -15V$

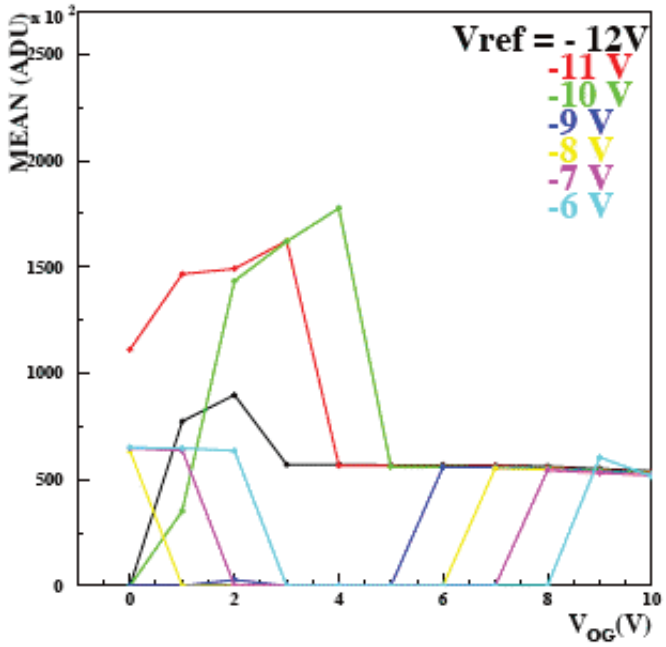

Figure A.9: Output transfer gate voltage, V_{OG}, require to cause charge injection for different V_{ref}.

A.3.4 X-ray calibration

As we mention before, an alternative method to obtain the gain is the Fe^{55} X-ray spectrum (for details see Janesick (2001)). This technique is based on the assumption that the energy deposited by an X-ray hit its restricted in one pixel. Because DECam detectors are back illuminated, the charge diffusion makes the assumption of single pixels hit non valid and this test is not included in the production phase. However, in the initial phase we use front illuminated detectors and exposed to X-rays to study this method (see results in Estrada et al. (2006) and Campa (2007)).

Figure A.10 shows the X-ray spectrum measured for the detector with an exposure of $40s$. The overscan has been subtracted. The plots shows two main peaks, the leftmost one corresponding to the pedestal, only the dark counts collected in a pixel, and the rightmost one correspond to 1620 e^- deposited in single pixel hits by X-ray of 5.9 keV (K_α). A less significant peak corresponding to 6.5 keV (K_β) is also seen. Knowing the number of generated electrons by the two peaks, we calculate the gain and compared with the PTC curve for the same CCD. We found that the measurements with this two methods agree at 1σ level.

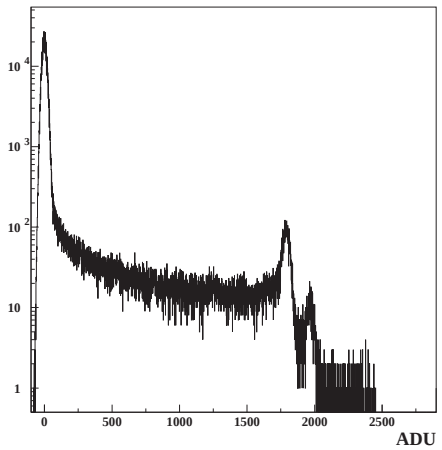

Figure A.10: X-ray spectrum with overscan subtracted. The K_α and K_β are shown (Campa (2007)).

Appendix B

Profile of Dark Matter Halos

Abstract: In this appendix we will discuss about the profile of dark matter halos. This quantity is useful in the halo model of non linear dark matter power spectrum or, equivalently, the correlation function.

B.1 Pro le of Dark Matter Halos

The radial mass profile can be analyzed in N-body simulations if individual halos are represented by a su cient number of dark matter particles. The ability to obtain halo mass profiles depends on the mass resolution of a simulation. The result is that halos seem to show a universal density profile given by

$$\rho(r\ M) = \rho_s \left(\frac{r}{r_s}\right)^{-\alpha} \left(1 + \frac{r}{r_s}\right)^{-\beta} \tag{B.1}$$

Setting $(\alpha, \beta) = (1, 3)$ and $(1, 2)$ in the last equation gives the Hernquist (1990) and Navarro et al. (1996), respectively.

These profiles have two parameters r_s and ρ_s, which define a characteristic radius and the density at that radius, respectively. The parameter r_s marks the radius where the slope of the density profile changes. For $r << r_s$ we find $\rho \quad r^{-1}$, whereas for $r << r_s$, the profile follows $\rho \quad r^{-3}$. These two parameters can be calibrated in numerical simulations and expressed in terms of virialization condition inspired by the spherical collapse model described in Chapter 6. The edge of the object is its virial radius r_{vir} and the mean density of the dark matter haloes is $\bar{\rho} = \Delta_{vir}\rho_{crit}(z)$. The mass is analytically integrable for the NFW and Hernquist profiles,

$$M \equiv \int_0^{r_{vir}} dr 4\pi r^2 \rho(r\ M) \tag{B.2}$$

The concentration parameter $c \equiv \frac{r_{vir}}{r_s}$ characterizes the matter distribution in the dark matter haloes. The larger the value of c, the more strongly the mass is concentrated towards the inner regions. The massive virialized halos are less centrally concentrated that low mass halos.

Simulations show that the concentration index c is strong correlated with the mass and the redshift of the halo. There is also an intrinsic scatter between them that arise because the differences in formation time and merger history of the halo. For halos of the same mass, there is a distribution of concentrations c, which is well described by a log-normal distribution (Bullock et al. (2001), Jing and Suto (2002)). N-body simulations have shown a power law dependence of the concentration parameter with the halo mass given by (Cooray and Sheth (2002a)),

$$\bar{c}(M,z) = \frac{9}{1+z}\left[\frac{M}{M_*}\right]^{-0.13} \tag{B.3}$$

where M_* is the characteristic mass scale already mentioned in 7.1.3. This equation quantifies the tendency for low mass halshaloso to be more centrally concentrated on average than massive halos.

Alternative models, in particular the Einasto profile (Einasto (1965)), have been shown to represent the dark matter profiles of simulated halos as well as or better than the NFW profile. Because of the limited resolution of N-body simulations, it is not yet known which model provides the best description of the central densities of simulated dark-matter halos.

The normalized Fourier transform of the density profile is useful in the halo model of non linear dark matter power spectrum or, equivalently, the correlation function (see Section 7.2).

$$u(\bar{k}\ M) = \frac{\int d^3\bar{x}\rho(\bar{x}\ M)exp(-i\bar{k}\dot{\bar{x}})}{\int d^3\bar{x}\rho(\bar{x}\ M)} \tag{B.4}$$

If we assume spherically symmetric profiles truncated at the virial radius, this becomes

$$u(k\ M) = \int_0^{r_v ir} dr 4\pi r^2 \frac{sin(kr)}{kr}\frac{\rho(r\ M)}{M} \tag{B.5}$$

Appendix C

Two Point Correlation Function Estimators

Abstract: In this appendix we summarize the different studies about the behavior of different the two point correlation function and discuss why the LS is the best option.

C.1 Choosing an Estimator

The simplest edge correction is the natural estimator, first used for the study of the angular correlation function by Peebles (1974). It is defined by

$$\xi_{PH}(r) = \frac{DD(r)}{RR(r)} - 1 \tag{C.1}$$

Apart from the LS estimator, other common estimators involve also ratios of galaxy pairs counts to cross-correlated pair counts of data and random points. Some of them are

$$\xi_{DP}(r) = \frac{DD(r)}{DR(r)} - 1 \tag{C.2}$$

$$\xi_{H}(r) = \frac{DD(r)RR(r)}{DR^2(r)} \tag{C.3}$$

where subscripts denote David and Peebles (1983) (DP) and Hamilton (1993)(H).

Some studies have compared the behavior of the different two point correlation function estimators. The results are the same; the differences between the estimates are more relevant at large scales where $\xi(r) << 1$ and uctuations in the mean density affect the estimators more strongly.

Since our goal in this thesis is not to confirmed the best estimator, we only test the Landy and Szalay (1993) estimator against Peebles (1974) using the Hubble Volume Simulation snapshot at z=0. Figure C.1 shows our $\xi(r)$ results and Figure C.2 compare the Peebles (1974) to Landy and Szalay (1993) to see better the deviations. Since our goal is to divide the sample in mass cuts, we shows the results for two subsamples. The ratio of random to data points used for the biggest sample is 1 and for the smallest is 10. We confirmed that there is a discrepancy between the two estimators at large scales.

Pons-Borderia et al. (1999) analyzed 6 estimators and find that at large scales the Hamilton and Landy-Szalay estimators provide the best results. Kerscher et al. (2000) compared nine of the most important estimators using a predetermined and rigorous criterion. He found that the Hamilton and Landy-Szalay estimators are much better that the others in terms of variance. While the two estimators yield almost identical results for infinite number of random points, the Hamilton estimator is considerably more sensitive to the number of random points employed than the LS version. From a practical point of view, therefore for astrophysical applications they recommends the Landy-Szalay estimator.

Later Kazin et al. (2010) and subsequently Labatie et al. (2012) also studied the uncertainties in four correlation function estimators with simulations. Their goal were comparing them at large scales for BAO studies, although they also studied them at small and intermediate scales. They tested the Landy and Szalay (1993) against the four estimators we mention before and both studies confirmed that Hamilton and Landy-Szalay have much smaller variances.

Kazin et al. (2010) compute the mean averaging over 160 realizations $\bar{\xi}$ and also the rms of the signal $\sigma_\xi = \overline{C_{ii}}$, where C_{ii} is the covariance of ξ. He found that Landy and Szalay (1993) and Hamilton (1993) agree on all scales but Peebles (1974) and David and Peebles (1983) deviate from the latter at large scales. Moreover, he found that Hamilton does not perform as well as Landy-Szalay at smaller scales because the former has a larger variance at $r < 10\ Mpc/h$.

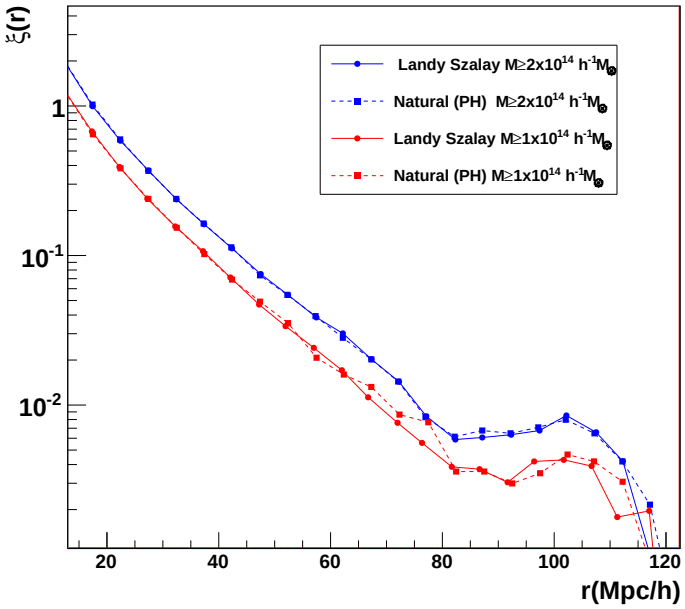

Figure C.1: $\xi(r)$ estimators for two subsamples of HVS snapshot at z=0.

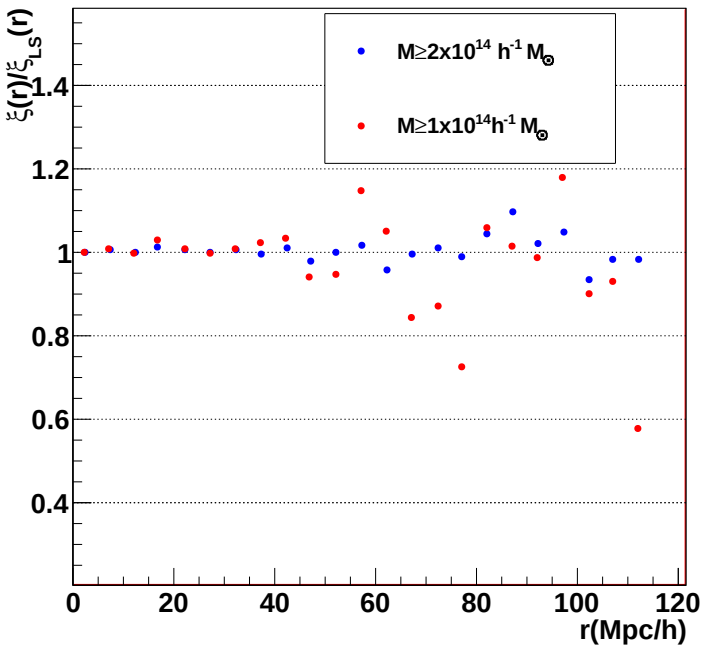

Figure C.2: Comparison of natural estimator to LS93. The ratio of random to data points used for the biggest sample is 1 and for the smallest is 10. We find discrepancies at large scales and they are higher for the first subsample.

Bibliography

Y asi, del mucho leer y del poco dormir,
se le seco el cerebro de manera que vino
a perder el juicio.

Miguel de Cervantes Saavedra

Abbott, T., Abdalla, F., Achitouv, I., Ahn, E., Aldering, G., Allam, S., Alonso, D., Amara, A., Annis, J., Antonik, M. and et al. First SN Discoveries from the Dark Energy Survey. *The Astronomer's Telegram*, vol. 4668, page 1, 2012.

Abell, G. O. The Distribution of Rich Clusters of Galaxies. *The Astrophysical Journal*, vol. 3, page 211, 1958.

Abell, G. O., Corwin, J. and Olowin, R. P. A catalog of rich clusters of galaxies. *The Astrophysical Journal*, vol. 70, pages 1 138, 1989.

Adler, R. J. *The Geometry of Random Fields*. John Wiley & Sons, New York, 1981.

Allen, S. D., Evrard, A. E. and Mantz, A. B. Cosmological Parameters from Observations of Galaxy Clusters. *Annual Review of Astronomy & Astrophysics*, vol. 49, pages 409 470, 2011.

Annis, J., Soares-Santos, M., Strauss, M. A., Becker, A. C., Dodelson, S., Fan, X., Gunn, J. E., Hao, J., Ivezic, Z., Jester, S., Jiang, L., Johnston, D. E., Kubo, J. M., Lampeitl, H., Lin, H., Lupton, R. H., Miknaitis, G., Seo, H.-J., Simet, M. and Yanny, B. The SDSS Coadd: 275 deg 2 of Deep SDSS Imaging on Stripe 82. *ArXiv e-prints*, 2011.

Bahcall, N. A. and Soneira, R. M. The spatial correlation function of rich clusters of galaxies. *The Astrophysical Journal*, vol. 270, pages 20 38, 1983.

Balaguera-Antolínez, A., Sánchez, A. G., Boehringer, H., Collins, C., Guzzo, L. and Phleps, S. The REFLEX II galaxy cluster

survey: power spectrum analysis. *Monthly Notices of the Royal Astronomical Society*, vol. 413, pages 386 400, 2011.

BARDEEN, J. M., BOND, J. R. and SZALAY, N. K. A. S. The statistics of peaks of Gaussian random fields. *The Astrophysical Journal*, vol. 304, pages 15 61, 1986.

BARRIGA, J. and GAZTAÑAGA, E. The three-point function in large-scale structure - I. The weakly non-linear regime in N-body simulations. *Monthly Notices of the Royal Astronomical Society*, vol. 333, pages 443 453, 2002.

BARTELMANN, M. and SCHNEIDER, P. Weak gravitational lensing. *Physics Reports*, vol. 340, pages 291 472, 2001.

BATTYE, R. A. and WELLER, J. Constraining cosmological parameters using Sunyaev-Zel'dovich cluster surveys. *Physical Review D*, vol. 68(8), page 083506, 2003.

BAUGH, C. M. Luminosity Bias: From Haloes to Galaxies. , vol. 30, page 30, 2013.

BERINGER, J., ARGUIN, J., BARNETT, R., COPIC, K., DAHL, O., GROOM, D., LIN, C., LYS, J., MURAYAMA, H., WOHL, C. and YAO, W. *Phys. Rev*, vol. D86(010001), 2012.

BERLIND, A. A. and WEINBERG, D. H. The Halo Occupation Distribution: Toward an Empirical Determination of the Relation between Galaxies and Mass. *The Astrophysical Journal*, vol. 575, pages 587 616, 2002.

BERTSCHINGER, E. Simulations of Structure Formation in the Universe. *Annual Review of Astronomy & Astrophysics*, vol. 36, pages 599 654, 1998.

BONAMENTE, M., JOY, M., LAROQUE, S. J., CARLSTROM, J. E., NAGAI, D. and MARRONE, D. P. Scaling Relations from Sunyaev-Zel'dovich Effect and Chandra X-Ray Measurements of High-Redshift Galaxy Clusters. *The Astrophysical Journal*, vol. 675, pages 106 114, 2008.

BOND, J. R., COLE, S., EFSTATHIOU, G. and KAISER, N. Excursion set mass functions for hierarchical Gaussian uctuations. *The Astrophysical Journal*, vol. 379, pages 440 460, 1991.

BORGANI, S. and KRAVTSOV, A. Cosmological simulations of galaxy clusters. *ArXiv e-prints*, 2009.

BRIEL, U. G., HENRY, J. P. and BOEHRINGER, H. Observation of the Coma cluster of galaxies with ROSAT during the all-sky survey. *Astronomy & Astrophysics*, vol. 259, pages L31 L34, 1992.

BRYAN, G. L. and NORMAN, M. L. Statistical Properties of X-Ray Clusters: Analytic and Numerical Comparisons. *The Astrophysical Journal*, vol. 495, pages 80 99, 1998.

BULLOCK, J. S., DEKEL, A., KOLATT, T. S., KRAVTSOV, A. V., KLYPIN, A. A., PORCIANI, C. and PRIMACK, J. R. A Universal Angular Momentum Profile for Galactic Halos. *The Astrophysical Journal*, vol. 555, pages 240 257, 2001.

BUNN, E. F. and WHITE, M. The 4 Year COBE Normalization and Large-Scale Structure. *The Astrophysical Journal*, vol. 480, pages 6 21, 1997.

CAMPA, J. *Characterization techniques for Scientific Charge-Couple Devices*. Proyecto Fin de Carrera, Universidad Autonoma de Barcelona, 2007.

CAROLL, S., PRESS, W. and TURNER, E. The cosmological constant. *Annual Review of Astronomy & Astrophysics*, vol. 30, pages 499 542, 1992.

COHN, J. D., EVRARD, A. E., WHITE, M., CROTON, D. and ELLINGSON, E. Red-sequence cluster finding in the Millennium Simulation. *Monthly Notices of the Royal Astronomical Society*, vol. 382, pages 1738 1750, 2007.

COLE, S. The 2dF Galaxy Redshift Survey: power-spectrum analysis of the final data set and cosmological implications. *Monthly Notices of the Royal Astronomical Society*, vol. 362, pages 505 534, 2005.

COLE, S. and KAISER, N. Biased clustering in the cold dark matter cosmogony. *Monthly Notices of the Royal Astronomical Society*, vol. 237, pages 1127 1146, 1989.

COLES, P. and JONES, B. A lognormal model for the cosmological mass distribution. *Monthly Notices of the Royal Astronomical Society*, vol. 248, pages 1 13, 1991.

COORAY, A. and SHETH, R. Halo models of large scale structure. *Physics Reports*, vol. 372, pages 1 129, 2002a.

COORAY, A. and SHETH, R. Halo models of large scale structure. *Phys.Rept.*, vol. 372, pages 1 129, 2002b.

CROCCE, M. and SCOCCIMARRO, R. Nonlinear evolution of baryon acoustic oscillations. *Physical Review D*, vol. 77(2), page 023533, 2008.

CROFT, R. A. C., MATTEO, T. D., KHANDAI, N., SPRINGEL, V., JANA, A. and GARDNER, J. P. Dark matter halo occupation: environment and clustering. *Monthly Notices of the Royal Astronomical Society*, vol. 425, pages 2766 2777, 2012.

DAVID, M. and PEEBLES, P. *ApJ*, vol. 267, pages 465 482, 1983.

DAVIS, M., EFSTATHIOU, G., FRENK, C. S. and WHITE, S. D. M. The evolution of large-scale structure in a universe dominated by cold dark matter. *The Astrophysical Journal*, vol. 292, pages 371 394, 1985.

DEKEL, A. and LAHAV, O. Stochastic Nonlinear Galaxy Biasing. *The Astrophysical Journal*, vol. 520, pages 24 34, 1999.

DERYLO, G., DIEHL, H. T. and ESTRADA, J. 0.250mm-thick CCD packaging for the Dark Energy Survey Camera array. In *Society of Photo-Optical Instrumentation Engineers (SPIE) Conference Series*, vol. 6276 of *Society of Photo-Optical Instrumentation Engineers (SPIE) Conference Series*. 2006.

DIEHL, H. T. and ET AL. The dark energy survey and operations: Year 1, 2014. Unpublished Proceedings of the Society of Photo-Optical Instrumentation Engineers (SPIE) Conference Series.

DIEHL, H. T., ANGSTADT, R., CAMPA, J., CEASE, H., DERYLO, G., EMES, J. H., ESTRADA, J., KUBIK, D., FLAUGHER, B. L., HOLLAND, S. E., JONAS, M., KOLBE, W. F., KRIDER, J., KUHLMANN, S., KUK, K., MAIORINO, M., PALAIO, N., PLAZAS, A., ROE, N. A., SCARPINE, V., SCHULTZ, K., SHAW, T., SPINKA, H. and STUERMER, W. Characterization of DECam focal plane detectors. In *Society of Photo-Optical Instrumentation Engineers (SPIE) Conference Series*, vol. 7021 of *Society of Photo-Optical Instrumentation Engineers (SPIE) Conference Series*. 2008.

DIEHL, H. T. and DARK ENERGY SURVEY COLLABORATION. The Dark Energy Survey Camera (DECam). vol. 219 of *American Astronomical Society Meeting Abstracts*, page 413.05. 2012.

DODELSON, S. *Modern Cosmology*. Academic Press, 2003.

DONAHUE., M., VOIT, G. M., GIOIA, I., LUPINO, G., HUGHES, J. P. and STOCKE, J. T. A Very Hot, High-Redshift Cluster of Galaxies: More Trouble for Ω^o=1. *The Astrophysical Journal*, vol. 502, page 550, 1998.

EINASTO, J. On the Construction of a Composite Model for the Galaxy and on the Determination of the System of Galactic Parameters. *Trudy Astrofizicheskogo Instituta Alma-Ata*, vol. 5, pages 87 100, 1965.

EISENSTEIN, D. J. Detection of the Baryon Acoustic Peak in the Large-Scale Correlation Function of SDSS Luminous Red Galaxies. *The Astrophysical Journal*, vol. 633, pages 560 574, 2005.

EISENSTEIN, D. J. and HU, W. Baryonic Features in the Matter Transfer Function. *The Astrophysical Journal*, vol. 496, page 605, 1998.

EKE, V. R., COLES, S. and FRENK, C. S. Cluster evolution as a diagnostic for Omega. *Monthly Notices of the Royal Astronomical Society*, vol. 282, pages 263 280, 1996.

ESTRADA, J., ABBOTT, T., ANGSTADT, B., BUCKLEY-GEER, L., BROWN, M., CAMPA, J., CARDIEL, L., CEASE, H., FLAUGHER, B., DAWSON, K., DERYLO, G., DIEHL, H. T., GRUENENDAHL, S., KARLINER, I., MERRIT, W., MOORE, P., MOORE, T. C., ROE, N., SCARPINE, V., SCHMIDT, R., SCHUBNEL, M., SHAW, T., STUERMER, W. and THALER, J. CCD testing and characterization for dark energy survey. In *Society of Photo-Optical Instrumentation Engineers (SPIE) Conference Series*, vol. 6269 of *Society of Photo-Optical Instrumentation Engineers (SPIE) Conference Series*. 2006.

ESTRADA, J., ALVAREZ, R., ABBOTT, T., ANNIS, J., BONATI, M., BUCKLEY-GEER, E., CAMPA, J., CEASE, H., CHAPPA, S., DEPOY, D., DERYLO, G., DIEHL, H. T., FLAUGHER, B., HAO, J., HOLLAND, S., HUFFMAN, D., KARLINER, I., KUBIK, D., KUHLMANN, S., KUK, K., LIN, H., ROE, N., SCARPINE, V., SCHMIDT, R., SCHULTZ, K., SHAW, T., SIMAITIS, V., SPINKA, H., STUERMER, W., TUCKER, D., WALKER, A. and WESTER, W. Focal plane detectors for Dark Energy Camera (DECam). In *Society of Photo-Optical Instrumentation Engineers (SPIE) Conference Series*, vol. 7735 of *Society of Photo-Optical Instrumentation Engineers (SPIE) Conference Series*. 2010.

ESTRADA, J., SEFUSATTI, E. and FRIEMAN, J. A. The Correlation Function of Optically Selected Galaxy Clusters in the Sloan Digital Sky Survey. *The Astrophysical Journal*, vol. 692, pages 265 282, 2009.

EVRARD, A., MACFARLAND, T., COUCHMAN, H., COLBERG, J., YOSHIDA, N., WHITE, S., NNKINS, A., FRENK, C., PEARCE, F., EFSTATHIOU, G., PEACOCK, J. and THOMAS, P. Galaxy Clusters in Hubble Volume Simulations: Cosmological Constraints from Sky Survey Populations. *The Astrophysical Journal*, vol. 573, pages 7 36, 2002.

FINOGUENOV, A., REIPRICH, T. H. and BÖHRINGER, H. Details of the mass-temperature relation for clusters of galaxies. *Astronomy & Astrophysics*, vol. 368, pages 749 759, 2001.

FLAUGHER, B. L., ABBOTT, T. M. C., ANGSTADT, R., ANNIS, J., ANTONIK, M. L., BAILEY, J., BALLESTER, O., BERNSTEIN, J. P., BERNSTEIN, R. A., BONATI, M., BREMER, G., BRIONES, J., BROOKS, D., BUCKLEY-GEER, E. J., CAMPA, J., CARDIEL-SAS, L., CASTANDER, F., CASTILLA, J., CEASE, H., CHAPPA, S., CHI, E. C., DA COSTA, L., DEPOY, D. L., DERYLO, G., DE VINCENTE, J., DIEHL, H. T., DOEL,

P., ESTRADA, J., EITING, J., ELLIOTT, A. E., FINLEY, D. A., FLORES, R., FRIEMAN, J., GAZTANAGA, E., GERDES, D., GLADDERS, M., GUARINO, V., GUTIERREZ, G., GRUDZINSKI, J., HANLON, B., HAO, J., HOLLAND, S., HONSCHEID, K., HUFFMAN, D., JACKSON, C., JONAS, M., KARLINER, I., KAU, D., KENT, S., KOZLOVSKY, M., KREMPETZ, K., KRIDER, J., KUBIK, D., KUEHN, K., KUHLMANN, S. E., KUK, K., LAHAV, O., LANGELLIER, N., LATHROP, A., LEWIS, P. M., LIN, H., LORENZON, W., MARTINEZ, G., MCKAY, T., MERRITT, W., MEYER, M., MIQUEL, R., MORGAN, J., MOORE, P., MOORE, T., NEILSEN, E., NORD, B., OGANDO, R., OLSON, J., PATTON, K., PEOPLES, J., PLAZAS, A., QIAN, T., ROE, N., ROODMAN, A., ROSSETTO, B., SANCHEZ, E., SOARES-SANTOS, M., SCARPINE, V., SCHALK, T., SCHINDLER, R., SCHMIDT, R., SCHMITT, R., SCHUBNELL, M., SCHULTZ, K., SELEN, M., SERRANO, S., SHAW, T., SIMAITIS, V., SLAUGHTER, J., SMITH, R. C., SPINKA, H., STEFANIK, A., STUERMER, W., SYPNIEWSKI, A., TALAGA, R., TARLE, G., THALER, J., TUCKER, D., WALKER, A. R., WEAVERDYCK, C., WESTER, W., WOODS, R. J., WORSWICK, S. and ZHAO, A. Status of the Dark Energy Survey Camera (DECam) project. In *Society of Photo-Optical Instrumentation Engineers (SPIE) Conference Series*, vol. 8446 of *Society of Photo-Optical Instrumentation Engineers (SPIE) Conference Series*. 2012.

FRIEMAN, J. A., TURNER, M. S. and HUTERER, D. Dark Energy and the Accelerating Universe. *Annual Review of Astronomy & Astrophysics*, vol. 46, pages 385 432, 2008.

FRY, J. N. and GAZTAÑAGA, E. Biasing and hierarchical statistics in large-scale structure. *The Astrophysical Journal*, vol. 413, pages 447 452, 1993.

FUKUGITA, M., ICHIKAWA, T., GUNN, J. E., DOI, M., SHIMASAKU, K. and SCHNEIDER, D. P. The Sloan Digital Sky Survey Photometric System. *The Astronomical Journal*, vol. 111, page 1748, 1996.

GLADDERS, M. D. and YEE, H. The Red-Sequence Cluster Survey. I. The Survey and Cluster Catalogs for Patches RCS 0926+37 and RCS 1327+29. *The Astrophysical Journal*, vol. 157, pages 1 29, 2005.

GOTT, J. R., GUNN, J. E., SCHRAMM, D. N. and TINSLEY, B. M. An unbound universe. *The Astrophysical Journal*, vol. 194, pages 543 553, 1974.

GUNN, J. E. and GOTT, J. R. On the Infall of Matter Into Clusters of Galaxies and Some Effects on Their Evolution. *The Astrophysical Journal*, vol. 176, page 1, 1972.

HAIMAN, Z., MOHR, J. J. and HOLDER, G. P. Constraints on Cosmological Parameters from Future Galaxy Cluster Surveys. *The Astrophysical Journal*, vol. 553, pages 545 561, 2001.

HAMILTON, A. *ApJ*, vol. 417, page 19, 1993.

HANSEN, S. M., MCKAY, T. A., WECHSLER, R., ANNIS, J., SHELDON, E. S. and KIMBALL, A. Measurement of Galaxy Cluster Sizes, Radial Profiles, and Luminosity Functions from SDSS Photometric Data. *The Astrophysical Journal*, vol. 633, pages 122 137, 2005.

HARRISON, E. *Phys. Rev. D.*, vol. 1, page 2726, 1970.

HEATH, D. J. The growth of density perturbations in zero pressure Friedmann-Lemaitre universes. *Monthly Notices of the Royal Astronomical Society*, vol. 179, pages 351 358, 1977.

HERNQUIST, L. An analytical model for spherical galaxies and bulges. *The Astrophysical Journal*, vol. 356, pages 359 364, 1990.

HOGG, D. W. Distance measures in cosmology. *ArXiv Astrophysics e-prints*, 1999.

HOLLAND, S. E., GROOM, D. E., PALAIO, N. P., STOVER, R. J. and WEI, M. Fully depleted, back-illuminated charge-coupled devices fabricated on high-resistivity silicon. *IEEE Transactions on Electron Devices*, vol. 50, pages 225 238, 2003.

HU, W. and JAIN, B. Joint galaxy-lensing observables and the dark energy. *Physical Review D*, vol. 70(4), page 043009, 2004.

HU, W. and SUGIYAMA, N. Small-Scale Cosmological Perturbations: an Analytic Approach. *The Astrophysical Journal*, vol. 471, page 542, 1996.

HUBBLE, E. A Relation between Distance and Radial Velocity among Extra-Galactic Nebulae. *Proceedings of the National Academy of Science*, vol. 15, pages 168 173, 1929.

HÜTSI, G. Power spectrum of the maxBCG cluster sample: new evidence for the acoustic features. *ArXiv e-prints*, 2007.

IKEBE, Y., REIPRICH, T. H., BÖHRINGER, H., TANAKA, Y. and KITAYAMA, T. A new measurement of the X-ray temperature function of clusters of galaxies. *Astronomy & Astrophysics*, vol. 383, pages 773 790, 2002.

JANESICK, J. R. *Scientific charge-coupled devices*. The International Society of Optical Engineering, 2001.

JENKINS, A., FRENK, C., WHITE, S., COLBERG, J., EVRARD, A., COUCHMAN, H. and YOSHIDA, N. The mass function of dark matter haloes. *Monthly Notices of the Royal Astronomical Society*, vol. 321, pages 372 384, 2001.

JEONG, D. and KOMATSU, E. Perturbation Theory Reloaded. II. Nonlinear Bias, Baryon Acoustic Oscillations, and Millennium Simulation in Real Space. *The Astrophysical Journal*, vol. 691, pages 569 595, 2009.

JING, Y. P. and SUTO, Y. Triaxial Modeling of Halo Density Profiles with High-Resolution N-Body Simulations. *The Astrophysical Journal*, vol. 574, pages 538 553, 2002.

JOHNSTON, D. E., SHELDON, E. S., TASITSIOMI, A., FRIEMAN, J. A., WECHSLER, R. W. and MCKAY, T. A. Cross-Correlation Lensing: Determining Galaxy and Cluster Mass Profiles from Statistical Weak-Lensing Measurements. *The Astrophysical Journal*, vol. 656, pages 27 41, 2007.

KAISER, N. On the spatial correlations of Abell clusters. *The Astrophysical Journal*, vol. 284, pages L9 L12, 1984.

KAZIN, E., BLANTON, M., SCOCCIMARRO, M., MCBRIDE, C., BERLIND, A., BAHCALL, N., BRINKMANN, J., CZARAPATA, P., FRIEMAN, J. A., KENT, S. M., SCHEIDER, D. P. and SZALAY, A. *The Astrophysical Journal*, vol. 710, page 1444, 2010.

KERSCHER, M., SZAPUDI, I. and SZALAY, A. *ApJ*, vol. 535, pages 13 16, 2000.

KNOBEL, C. An Introduction into the Theory of Cosmological Structure Formation. *ArXiv e-prints*, 2012.

KOESTER, B. P., MCKAY, T. A., ANNIS, J., WECHSLER, R. H., EVRARD, A. E., BLEEM, E. R. L., SHELDON, E. S. and JOHNSTON, D. MaxBCG: A Red-Sequence Galaxy Cluster Finder. *The Astrophysical Journal*, vol. 660, pages 221 238, 2007.

KOMATSU, E., SMITH, K. M., DUNKLEY, J., BENNETT, C. L., GOLD, B., HINSHAW, G., JAROSIK, N., LARSON, D., NOLTA, M. R., PAGE, L., SPERGEL, D. N., HALPERN, M., HILL, R. S., KOGUT, A., LIMON, M., MEYER, S. S., ODEGARD, N., TUCKER, G. S., WEILAND, J. L., WOLLACK, E. and WRIGHT, E. L. Seven-year Wilkinson Microwave Anisotropy Probe (WMAP) Observations: Cosmological Interpretation. *The Astrophysical Journal*, vol. 192, page 18, 2011.

KUBIK, D., ALVAREZ, R., ABBOTT, T., ANNIS, J., BONATI, M., BUCKLEY-GEER, E., CAMPA, J., CEASE, H., CHAPPA, S., DEPOY, D., DERYLO,

G., DIEHL, H. T., ESTRADA, J., FLAUGHER, B., HAO, J., HOLLAND, S., HUFFMAN, D., KARLINER, I., KUHLMANN, S., KUK, K., LIN, H., MONTES, J., ROE, N., SCARPINE, V., SCHMIDT, R., SCHULTZ, K., SHAW, T., SIMAITIS, V., SPINKA, H., STUERMER, W., TUCKER, D., WALKER, A. and WESTER, W. Automated characterization of CCD detectors for DECam. In *Society of Photo-Optical Instrumentation Engineers (SPIE) Conference Series*, vol. 7735 of *Society of Photo-Optical Instrumentation Engineers (SPIE) Conference Series*. 2010.

KUHLEN, M., VOGELSBERGER, M. and ANGULO, R. Numerical simulations of the dark universe: State of the art and the next decade. *Physics of the Dark Universe*, vol. 1, pages 50 93, 2012.

LABATIE, A., STARCK, J., LACHIÈZE-REY, M. and ARNALTE-MUR, P. *Statistical Methodology*, vol. 9, pages 85 100, 2012.

LACEY, C. and COLE, S. Merger Rates in Hierarchical Models of Galaxy Formation - Part Two - Comparison with N-Body Simulations. *Monthly Notices of the Royal Astronomical Society*, vol. 271, page 676, 1994.

LAHAV, O., TERLEVICH, E. and TERLEVICH, R. J. *Gravitational Dynamics*. Cambridge University Press, 1996.

LANDY, S. D. and SZALAY, A. S. *ApJ*, vol. 412, pages 64 71, 1993.

LEAUTHAUD, A., FINOGUENOV, A., KNEIB, J. P., TAYLOR, J. E., MASSEY, R., RHODES, J., ILBERT, O., BUNDY, K., TINKER, J., GEORGE, M. R., CAPAK, P., KOEKEMOER, A. M., JOHNSTON, D. E., ZHANG, Y. Y., CAPPELLUTI, N., ELLIS, R. S., ELVIS, M., GIODINI, S., HEYMANS, C., FÈVRE, O. L., LILLY, S., MCCRACKEN, H. J., MELLIER, Y., RÉFRÉGIER, A., SALVATO, M., SCOVILLE, N., SMOOT, G., TANAKA, M., WAERBEKE, L. V. and WOLK, M. A Weak Lensing Study of X-ray Groups in the Cosmos Survey: Form and Evolution of the Mass-Luminosity Relation. *The Astrophysical Journal*, vol. 709, pages 97 114, 2010.

LEWIS, A. and BRIDLE, S. Cosmological parameters from CMB and other data: A Monte Carlo approach. *Physical Review D*, vol. 66(10), page 103511, 2002.

LIDDLE, A. R. and LYTH, D. *Cosmological Inflation and Large-Scale Structure*. Cambridge University Press, 2000.

LILJE, P. B. Abundance of rich clusters of galaxies - A test for cosmological parameters. *The Astrophysical Journal*, vol. 386, pages L33 L36, 1992.

LIMA, M. and HU, W. Self-calibration of cluster dark energy studies: Counts in cells. *Physical Review D*, vol. 70(4), page 043504, 2004.

LIMA, M. and HU, W. Self-calibration of cluster dark energy studies: Observable-mass distribution. *Physical Review D*, vol. 72(4), page 043006, 2005.

LSST SCIENCE COLLABORATION, ABELL, P. A., ALLISON, J., ANDERSON, S. F., ANDREW, J. R., ANGEL, J. R. P., ARMUS, L., ARNETT, D., ASZTALOS, S. J., AXELROD, T. S. and ET AL. LSST Science Book, Version 2.0. *ArXiv e-prints*, 2009.

LUKI , Z., HEITMANN, K., HABIB, S., BASHINSKY, S. and RICKER. The Halo Mass Function: High-Redshift Evolution and Universality. *The Astrophysical Journal*, vol. 671, pages 1160 1181, 2007.

MAJUMDAR, S. and MOHR, J. J. Self-Calibration in Cluster Studies of Dark Energy: Combining the Cluster Redshift Distribution, the Power Spectrum, and Mass Measurements. *The Astrophysical Journal*, vol. 613, pages 41 50, 2004.

MANDELBAUMAND, R., SELJAK, U., HIRATA, C. M., BARDELLI, S., BOLZONELLA, M., BONGIORNO, A., CAROLLO, M., CONTINI, T., CUNHA, C. E., GARILLI, B., IOVINO, A., KAMPCZYK, P., KNEIB, J. P., KNOBEL, C., KOO, D. C., LAMAREILLE, F., BORGNE, O. L. F. J. F. L., LILLY, S. J., MAIER, C., MAINIERI, V., MIGNOLI, M., NEWMAN, J. A., OESCH, P. A., PEREZ-MONTERO, E., RICCIARDELLI, E., SCODEGGIO, M., SILVERMAN, J. and TASCA, L. Precision photometric redshift calibration for galaxy-galaxy weak lensing. *Monthly Notices of the Royal Astronomical Society*, vol. 386, pages 781 806, 2008.

MANERA, M. and GAZTAÑAGA, E. The local bias model in the large-scale halo distribution. *Monthly Notices of the Royal Astronomical Society*, vol. 415, pages 383 398, 2011.

MANERA, M., SCOCCIMARRO, R., PERCIVAL, W., SAMUSHIA, L., MCBRIDE, C., ROSS, A., SHETH, R., WHITE, M., REID, B., SÃ NCHEZ, A., DE PUTTER, R., XU, X., BERLIND, A., BRINKMANN, J., NICHOL, B., MONTESANO, F., PADMANABHAN, N., SKIBBA, R., TOJEIRO, R. and WEAVER, B. The clustering of galaxies in the SDSS-III Baryon Oscillation Spectroscopic Survey: a large sample of mock galaxy catalogues. *Monthly Notices of the Royal Astronomical Society*, vol. 428, pages 1036 1054, 2013.

MANTZ, A., ALLEN, S. W., EBELING, H. and RAPETTI, D. New constraints on dark energy from the observed growth of the most X-ray luminous galaxy clusters. *Monthly Notices of the Royal Astronomical Society*, vol. 387, pages 1179 1192, 2008.

MARTINEZ, V. J. and SAAR, E. *Statistic of the Galaxy Distribution*. CHAPMAN and HALL/CRC, 2002.

MATSUMOTO, M. and NISHIMIRA, T. *ACM Transactions on Modeling and Computer Simulation*, vol. 8(1), pages 3 30, 1998.

MELCHIOR, P., SUCHYTA, E., HUFF, E., HIRSCH, M., KACPRZAK, T., RYKOFF, E., GRUEN, D., ARMSTRONG, R., BACON, D., BECHTOL, K., BERNSTEIN, G. M., BRIDLE, S., CLAMPITT, J., HONSCHEID, K., JAIN, B., JOUVEL, S., KRAUSE, E., LIN, H., MACCRANN, N., PATTON, K., PLAZAS, A., ROWE, B., VIKRAM, V., WILCOX, H., YOUNG, J., ZUNTZ, J., ABBOTT, T., ABDALLA, F., ALLAM, S. S., BANERJI, M., BERNSTEIN, J. P., BERNSTEIN, R. A., BERTIN, E., BUCKLEY-GEER, E., BURKE, D. L., CASTANDER, F. J., DA COSTA, L. N., CUNHA, C. E., DEPOY, D. L., DESAI, S., DIEHL, H. T., DOEL, P., ESTRADA, J., EVRARD, A. E., FAUSTI NETO, A., FERNANDEZ, E., FINLEY, D. A., FLAUGHER, B., FRIEMAN, J. A., GAZTANAGA, E., GERDES, D., GRUENDL, R. A., GUTIERREZ, G. R., JARVIS, M., KARLINER, I., KENT, S., KUEHN, K., KUROPATKIN, N., LAHAV, O., MAIA, M. A. G., MAKLER, M., MARRINER, J., MARSHALL, J. L., MERRITT, K. W., MILLER, C. J., MIQUEL, R., MOHR, J., NEILSEN, E., NICHOL, R. C., NORD, B. D., REIL, K., ROE, N. A., ROODMAN, A., SAKO, M., SANCHEZ, E., SANTIAGO, B. X., SCHINDLER, R., SCHUBNELL, M., SEVILLA-NOARBE, I., SHELDON, E., SMITH, C., SOARES-SANTOS, M., SWANSON, M. E. C., SYPNIEWSKI, A. J., TARLE, G., THALER, J., THOMAS, D., TUCKER, D. L., WALKER, A., WECHSLER, R., WELLER, J. and WESTER, W. Mass and galaxy distributions of four massive galaxy clusters from Dark Energy Survey Science Verification data. *ArXiv e-prints*, 2014.

MIYAZAKI, S., KOMIYAMA, Y., NAKAYA, H., DOI, Y., FURUSAWA, H., GILLINGHAM, P., KAMATA, Y., TAKESHI, K. and NARIAI, K. vol. 6269 of *Proc.SPIE Int.Soc.Opt.Eng*, page 9. 2006.

MO, H. J., JING, Y. P. and WHITE, S. High-order correlations of peaks and haloes: a step towards understanding galaxy biasing. *Monthly Notices of the Royal Astronomical Society*, vol. 284, pages 189 201, 1997.

MO, H. J. and WHITE, S. D. M. An analytic model for the spatial clustering of dark matter haloes. *Monthly Notices of the Royal Astronomical Society*, vol. 282, pages 347 361, 1996.

MOHR, J. J. Cluster Survey Studies of the Dark Energy. In *Observing Dark Energy* (editado por S. C. Wolff and T. R. Lauer), vol. 339 of *Astronomical Society of the Pacific Conference Series*, page 140. 2005.

NAVARRO, J. F., FRENK, C. S. and WHITE, S. D. M. The Structure of Cold Dark Matter Halos. *The Astrophysical Journal*, vol. 462, page 563, 1996.

NORBERG, P., GAZTANAGA, E., BAUGH, C. and CROTON, D. *M*, vol. 396, page 19, 2009.

OGURI, M. and TAKADA, M. Combining cluster observables and stacked weak lensing to probe dark energy: Self-calibration of systematic uncertainties. *Physical Review D*, vol. 83(2), page 023008, 2011.

PEACOCK, J. A. *Cosmological Physics*. Cambridge University Press, 1999.

PEACOCK, J. A. and HEAVENS, A. F. Alternatives to the Press-Schechter cosmological mass function. *Monthly Notices of the Royal Astronomical Society*, vol. 243, pages 133 143, 1990.

PEACOCK, J. A. and SMITH, R. E. Halo occupation numbers and galaxy bias. *Monthly Notices of the Royal Astronomical Society*, vol. 318, pages 1144 1156, 2000.

PEEBLES, P. *ApJ*, vol. 185, pages 413 440, 1973.

PEEBLES, P. *ApJ*, vol. 28, page 19, 1974.

PEEBLES, P. *The Large-Scale Structure of the Universe*. Princeton University Press, 1980.

PEEBLES, P. J. E. and YU, J. T. Primeval Adiabatic Perturbation in an Expanding Universe. *The Astrophysical Journal*, vol. 162, page 815, 1970.

PENNA, M. *Abundancia de Aglomerados de Galaxias como Observable Cosmologico:AplicaÃ§oes aos Levantamentos Fotometricos DES e SDSS*. Tesis Doctoral, Centro Brasileiro de Pesquisas FÃsicas, 2010.

PERLMUTTER, S., ALDERING, G., GOLDHABER, G., KNOP, R. A., NUGENT, P., CASTRO, P. G., DEUSTUA, S., FABBRO, S., GOOBAR, A., GROOM, D. E., HOOK, I. M., KIM, A. G., KIM, M. Y., LEE, J. C., NUNES, N. J., PAIN, R., PENNYPACKER, C. R., QUIMBY, R., LIDMAN, C., ELLIS, R. S., IRWIN, M., MCMAHON, R. G., RUIZ-LAPUENTE, P., WALTON, N., SCHAEFER, B., BOYLE, B. J., FILIPPENKO, A. V., MATHESON, T., FRUCHTER, A. S., PANAGIA, N., NEWBERG, H. J. M., COUCH, W. J. and PROJECT, S. C. Measurements of Omega and Lambda from 42 High-Redshift Supernovae. *The Astrophysical Journal*, vol. 517, pages 565 586, 1999.

PILLEPICH, A., PORCIANI, C. and O. HAHN, O. Halo mass function and scale-dependent bias from N-body simulations with non-Gaussian initial

conditions. *Monthly Notices of the Royal Astronomical Society*, vol. 402, pages 191 206, 2010.

PONS-BORDERIA, M., MARTÍNEZ, V., STOYAN, D., STOYAN, H. and SAAR, E. *ApJ*, vol. 523, pages 480 491, 1999.

PRESS, W. H. and SCHECHTER, P. Formation of Galaxies and Clusters of Galaxies by Self-Similar Gravitational Condensation. *The Astrophysical Journal*, vol. 187, pages 425 438, 1974.

REIPRICH, T. H. and BÖHRINGER, H. The Mass Function of an X-Ray Flux-limited Sample of Galaxy Clusters. *The Astrophysical Journal*, vol. 567, pages 716 740, 2002.

RIESS, A. G., FILIPPENKO, A. V., CHALLIS, P., CLOCCHIATTI, A., DIERCKS, A., GARNAVICH, P. M., GILLILAND, R. L., HOGAN, C. J., JHA, S., KIRSHNER, R. P., LEIBUNDGUT, B., PHILLIPS, M. M., REISS, D., SCHMIDT, B. P., SCHOMMER, R. A., SMITH, R. C., SPYROMILIO, J., STUBBS, C., SUNTZEFF, N. B. and TONRY, J. Observational Evidence from Supernovae for an Accelerating Universe and a Cosmological Constant. , vol. 116, pages 1009 1038, 1998.

ROZO, E., RYKOFF, E., KOESTER, B., NORD, B., WU, H. Y., EVRARD, A. and WECHSLER, R. Extrinsic Sources of Scatter in the Richness-mass Relation of Galaxy Clusters. *The Astrophysical Journal*, vol. 740, page 53, 2011.

ROZO, E., RYKOFF, E. S., BARTLETT, J. B. and MELIN, J. B. redMaPPer III: A Detailed Comparison of the Planck 2013 and SDSS DR8 RedMaPPer Cluster Catalogs. *ArXiv e-prints*, 2014.

ROZO, E., RYKOFF, E. S., EVRARD, A., BECKER, M., MCKAY, T., WECHSLER, R. H., KOESTER, B. P., HAO, J., HANSEN, S., SHELDON, E., JOHNSTON, D., ANNIS, J. and FRIEMAN, J. Constraining the Scatter in the Mass-richness Relation of maxBCG Clusters with Weak Lensing and X-ray Data. *The Astrophysical Journal*, vol. 699, pages 768 781, 2009.

ROZO, E., RYKOFF, E. S., KOESTER, B. P., MCKAY, T., HAO, J., EVRARD, A., WECHSLER, R. H., HANSEN, S., SHELDON, E., JOHNSTON, D., BECKER, M., ANNIS, J., BLEEM, L. and SCRANTON, R. Improvement of the Richness Estimates of maxBCG Clusters. *The Astrophysical Journal*, vol. 703, pages 601 613, 2009.

ROZO, E., WECHSLER, R. H., RYKOFF, E. S., ANNIS, J. T., BECKER, M. R., EVRARD, A. E., FRIEMAN, J. A., HANSEN, S. M., HAO, J., JOHNSTON, D. E., KOESTER, B. P., MCKAY, T. A., SHELDON, E. S. and WEINBERG, D. H. Cosmological Constraints from the Sloan Digital

Sky Survey maxBCG Cluster Catalog. *The Astrophysical Journal*, vol. 708, pages 645 660, 2010.

RUHL, J., ADE, P. A. R., CARLSTROM, J. E., CHO, H.-M., CRAWFORD, T., DOBBS, M., GREER, C. H., HALVERSON, N. W., HOLZAPFEL, W. L., LANTING, T. M., LEE, A. T., LEITCH, E. M., LEONG, J., LU, W., LUEKER, M., MEHL, J., MEYER, S. S., MOHR, J. J., PADIN, S., PLAGGE, T., PRYKE, C., RUNYAN, M. C., SCHWAN, D., SHARP, M. K., SPIELER, H., STANISZEWSKI, Z. and STARK, A. A. The South Pole Telescope. In *Z-Spec: a broadband millimeter-wave grating spectrometer: design, construction, and first cryogenic measurements* (editado por C. M. Bradford, P. A. R. Ade, J. E. Aguirre, J. J. Bock, M. Dragovan, L. Duband, L. Earle, J. Glenn, H. Matsuhara, B. J. Naylor, H. T. Nguyen, M. Yun and J. Zmuidzinas), vol. 5498 of *Society of Photo-Optical Instrumentation Engineers (SPIE) Conference Series*, pages 11 29. 2004.

RYKOFF, E. S., EVRARD, A. E., MCKAY, T. A., BECKER, M. R., JOHNSTON, D. E., KOESTER, B. P., NORD, B., ROZO, E., SHELDON, E. S., STANEK, R. and WECHSLER, R. H. The L_X-M relation of clusters of galaxies. *Monthly Notices of the Royal Astronomical Society*, vol. 387, pages L28 L32, 2008.

RYKOFF, E. S., KOESTER, B. P., ROZO, E., ANNIS, J., EVRARD, A. E., HANSEN, S. M., HAO, J., JOHNSTON, D. E., MCKAY, T. A. and WECHSLER, R. H. Robust Optical Richness Estimation with Reduced Scatter. *The Astrophysical Journal*, vol. 746, page 178, 2012.

SÁNCHEZ, A. G., BAUGH, C. M. and ANGULO, R. E. What is the best way to measure baryonic acoustic oscillations? *Monthly Notices of the Royal Astronomical Society*, vol. 390, pages 1470 1490, 2008.

SCHECHTER, P. An analytic expression for the luminosity function for galaxies. *The Astrophysical Journal*, vol. 203, pages 297 306, 1976.

SCHERRER, R. J. and BERTSCHINGER, E. Statistics of primordial density perturbations from discrete seed masses. *The Astrophysical Journal*, vol. 381, pages 349 360, 1991.

SCHNEIDER, P. *Extragalactic Astronomy and Cosmology*. Springer, 2006.

SCHUECKER, P., BÖHRINGER, H., COLLINS, C. and L.GUZZO. The REFLEX galaxy cluster survey. VII. Ω_m and σ_8 from cluster abundance and large-scale clustering. *Astronomy & Astrophysics*, vol. 398, pages 867 877, 2003.

SCOCCIMARRO, R., SHETH, R. K., HUI, L. and JAIN, B. How many galaxies fit in a halo? constraints on galaxy formation e ciency from spatial clustering. *The Astrophysical Journal*, vol. 546(1), page 20, 2001.

SELJAK, U. Analytic model for galaxy and dark matter clustering. *Monthly Notices of the Royal Astronomical Society*, vol. 318, pages 203 213, 2000.

SELJAK, U. and ZALDARRIAGA, M. A Line-of-Sight Integration Approach to Cosmic Microwave Background Anisotropies. *The Astrophysical Journal*, vol. 469, page 437, 1996.

SHAW, T., BALLESTER, O., CARDIEL-SAS, L., CASTILLA, J., CHAPPA, S., DE VICENTE, J., HOLM, S., HUFFMAN, D., KOZLOVSKY, M., MARTÍNEZ, G., MOORE, T., OLSEN, J., SIMAITIS, V. and STUERMER, W. The Dark Energy Camera readout system. In *Society of Photo-Optical Instrumentation Engineers (SPIE) Conference Series*, vol. 8453 of *Society of Photo-Optical Instrumentation Engineers (SPIE) Conference Series*. 2012.

SHAWN, L. D., HOLDER, G. P. and BODE, P. The Impact of Halo Properties, Energy Feedback, and Projection Effects on the Mass-SZ Flux Relation. *The Astrophysical Journal*, vol. 686, pages 206 218, 2008.

SHELDON, E. S., JOHNSTON, D. E., MASJEDI, M., MCKAY, T. A., BLANTON, M. R., SCRANTON, R., WECHSLER, R. H., KOESTER, B. P., HANSEN, S. M., FRIEMAN, J. A. and ANNIS, J. Cross-correlation Weak Lensing of SDSS Galaxy Clusters. III. Mass-to-Light Ratios. *The Astrophysical Journal*, vol. 703, pages 2232 2248, 2009.

SHETH, R. K., MO, H. J. and TORMEN, G. Ellipsoidal collapse and an improved model for the number and spatial distribution of dark matter haloes. *Monthly Notices of the Royal Astronomical Society*, vol. 323, pages 1 12, 2001.

SHETH, R. K. and TORMEN, G. Large-scale bias and the peak background split. *Monthly Notices of the Royal Astronomical Society*, vol. 308, pages 119 126, 1999.

SILK, J. Cosmic Black-Body Radiation and Galaxy Formation. *The Astrophysical Journal*, vol. 151, page 459, 1968.

SMITH, R. E., PEACOCK, J. A., JENKINS, A., WHITE, S., FRENK, C., PEARCE, F., THOMAS, P., EFSTATHIOU, G. and COUCHMAN, H. M. Stable clustering, the halo model and non-linear cosmological power spectra. *Monthly Notices of the Royal Astronomical Society*, vol. 341, pages 1311 1332, 2003.

STANEK, R., EVRARD, A. E., BÖHRINGER, H., SCHUECKER, P. and NORD, B. The X-Ray Luminosity-Mass Relation for Local Clusters of Galaxies. *The Astrophysical Journal*, vol. 648, pages 956 968, 2006.

STANEK, R., RASIA, E., EVRARD, A. E., PEARCE, F. and GAZZOLA, L. Massive Halos in Millennium Gas Simulations: Multivariate Scaling Relations. *The Astrophysical Journal*, vol. 715, pages 1508 1523, 2010.

STANEK, R., RUDD, D. and EVRARD, A. E. The effect of gas physics on the halo mass function. *Monthly Notices of the Royal Astronomical Society*, vol. 394, pages L11 L15, 2009.

SUNYAEV, R. A. and B.ZELDOVICH, Y. Small-Scale Fluctuations of Relic Radiation. *Astrophysics and Space Science*, vol. 7, pages 3 19, 1970.

TAKADA, M. Subaru Hyper Suprime-Cam Project. In *American Institute of Physics Conference Series* (editado por N. Kawai and S. Nagataki), vol. 1279 of *American Institute of Physics Conference Series*, pages 120 127. 2010.

TAUBER, J. A., MANDOLESI, N., PUGET, J.-L., BANOS, T., BERSANELLI, M., BOUCHET, F. R., BUTLER, R. C., CHARRA, J., CRONE, G., DODSWORTH, J. and ET AL. Planck pre-launch status: The Planck mission. *Astronomy & Astrophysics*, vol. 520, page A1, 2010.

THE DARK ENERGY SURVEY COLLABORATION. The Dark Energy Survey. *ArXiv Astrophysics e-prints*, 2005.

TINKER, J., KRATSOV, A., ABAZAJIAN, K., WARREN, M., YEPES, G., GOTTLOBER, S. and HOLZ, D. Toward a Halo Mass Function for Precision Cosmology: The Limits of Universality. *The Astrophysical Journal*, vol. 688, pages 709 728, 2008.

TINKER, J., ROBERTSON, B., KRAVTSOV, A., KLYPIN, A., WARREN, M., YEPES, G. and GOTTLÖBER, S. The Large-scale Bias of Dark Matter Halos: Numerical Calibration and Model Tests. *The Astrophysical Journal*, vol. 724, pages 878 886, 2010.

VIKHLININ, A., KRAVTSOV, A. V., BURENIN, R. A., FORMAN, H. E. W. R., HORNSTRUP, A., JONES, C., MURRAY, S. S., NAGAI, D., QUINTANA, H. and VOEVODKIN, A. Chandra Cluster Cosmology Project III: Cosmological Parameter Constraints. *The Astrophysical Journal*, vol. 692, pages 1060 1074, 2009.

VOIT, G. M. Tracing cosmic evolution with clusters of galaxies. *Reviews of Modern Physics*, vol. 77, pages 207 258, 2005.

WARREN, M. S., ABAZAJIAN, K., HOLZ, D. E. and TEODORO, L. Precision Determination of the Mass Function of Dark Matter Halos. *The Astrophysical Journal*, vol. 646, pages 881 885, 2006.

WEINBERG., D. H., MORTONSON, M. J., EISENSTEIN, D. J., HIRATA, C., RIESS, A. G. and ROZO, E. Observational probes of cosmic acceleration. *Physics Reports*, vol. 530, pages 87 255, 2013.

WHITE, M. The mass of a halo. *Astronomy & Astrophysics*, vol. 367, pages 27 32, 2001.

WHITE, M. The Mass Function. *The Astrophysical Journal*, vol. 143, pages 241 255, 2002.

WHITE, S. D. M., NAVARRO, J. F., EVRARD, A. E. and FRENK, C. S. The baryon content of galaxy clusters: a challenge to cosmological orthodoxy. *Nature*, vol. 366, pages 429 433, 1993.

WHITE, S. D. M. and REES, M. J. Core condensation in heavy halos - A two-stage theory for galaxy formation and clustering. *Monthly Notices of the Royal Astronomical Society*, vol. 183, pages 341 358, 1978.

WU, H.-Y., ROZO, E. and WECHSLER, R. H. The Effects of Halo Assembly Bias on Self-Calibration in Galaxy Cluster Surveys. *The Astrophysical Journal*, vol. 688, pages 729 741, 2008.

ZEHAVI, I., BLANTON, M., FRIEMAN, J., WEINBERG, D., MO, H., STRAUSS, M., ANDERSON, S. and ANNIS, J. *The Astrophysical Journal*, vol. 571, page 172, 2002.

ZELDOVICH, Y. B. A hypothesis, unifying the structure and the entropy of the Universe. *Monthly Notices of the Royal Astronomical Society*, vol. 160, page 1P, 1972.

ZENTNER, A. The halo model, 2005.

ZENTNER, A. R. The Excursion Set Theory of Halo Mass Functions, Halo Clustering, and Halo Growth. *International Journal of Modern Physics D*, vol. 16, pages 763 815, 2007.

ZWICKY, F. Die Rotverschiebung von extragalaktischen Nebeln. *Helvetica Physica Acta*, vol. 6, pages 110 127, 1933.